Exploring Properties of Galaxy Clusters with the Atacama Cosmology Telescope

A.B. Candidate: Gabriele Montefalcone

Advisor: Professor Lyman Page

Senior Independent Work

Submitted to Princeton University

Department of Physics

In Partial Fulfillment of the Requirements for the A.B. Degree

May 2020

This paper represents my own work in accordance with University regulations.

/s/ *Gabriele Montefalcone*

Abstract

Galaxy clusters are the largest known gravitationally bound structures in the Universe. Their abundance as a function of redshift and mass is very sensitive to the matter power spectrum and, hence, constitutes an essential probe for testing models of the Universe and constraining the rate of growth of cosmological structure. In this work we analyze the ACT S18dn cluster catalog of $2,869$ clusters detected via the Sunyaev-Zel'dovich effect. Specifically, we study the properties of the radial profiles extracted from the thermal map and test the predictions of two theoretical models for the cluster pressure profile, namely the Isothermal β model and the Universal Pressure Profile (UPP). We also look at the profiles on the polarization maps to investigate whether or not there is a net polarization signal coming from the clusters. For both of these analysis, we use a stacking method, thoroughly described in Chapter 4, which allows us to compute the average profiles at a specific mass and redshift by stacking over mass and redshift ranges at a very high level of precision with error bars at each radial bin $\sigma_r \lesssim 1\mu\mathrm{K}$. We then repeat the same analysis for the 525 clusters detected by the PlanckSZ2 survey [1] that are in the overlapping region with the ACT field map but were not detected by the ACT experiment. We found that by applying this stacking procedure we are able to resolve these clusters from the unfiltered ACT map and note some distinct features in the thermal profiles of these clusters when compared to those from the original ACT S18dn catalog.

Where it is necessary to adopt a fiducial cosmology, we assume $\Omega_m = 0.3$, $\Omega_\Lambda = 0.7$, and $H_0 = 70$ km s^{-1} Mpc^{-1}, unless stated otherwise.

The ACT data on which this thesis is based are proprietary and not yet public. Related to this, all results presented here should be treated as preliminary and not vetted by the ACT collaboration.

Finally we give credit to Professor Matthew Hilton for providing the complete dataset of the clusters positions in R.A. and Dec, and their estimated mass and redshift.

Acknowledgements

First and foremost, I would like to express my greatest gratitude to my thesis advisor, Lyman Page for his assistance, resources and feedback throughout this year. It has been a joy and a great privilege to work with and learn from you. Additionally, this work would not have been made possible without the cluster catalog provided by Matt Hilton and (without) the fruitful guidance via email discussions. I want to also thank Suzanne Staggs for accepting to be my second reader.

In my time in Princeton, I was fortunate enough to collaborate with many other outstanding physicists. I would especially like to thank Cristiano Galbiati for bringing me in his research group when I was only a sophomore and allowing me to work at the Gran Sasso Laboratory for a summer. I am also extremely grateful to my J.P. advisor Paul J. Steinhardt, for giving me the opportunity to publish my first research together and for his continuous support and encouragement over the past two years, both academically and on a personal level. I appreciate everyone else who has bolstered my enthusiasm and understanding of physics in the last four years, especially an honorable mention to Silviu Pufu, Max Abitbol, Darsh Kodwani, Richard Stiskalek, Claudio Savarese and Alessandro Razeto.

Finally, and most importantly, I am deeply thankful to my family and close friends who have constantly and continuously supported all my dreams and endeavors. I thank you for the encouragement, inspiration and life lessons that have helped me achieve my aspirations and goals at and outside of Princeton. To everyone I've encountered in Princeton these past four years- it would not have been the same experience without you all.

Me piace pensá che er mejo,

deve ancora vení.

I like to think that the best is still yet to come.

Contents

List of Tables

List of Figures

Chapter 1

Introduction

1.1 The Physics of Galaxy clusters

1.1.1 Brief History of Structure Formation

The Big Bang model of cosmology posits that the Universe began in a hot, dense initial state and then expanded continuously, diluting its energy density over time. Assuming homogeneity and isotropy, the expansion of the Universe is determined by the average energy density (ρ_i) and relativistic pressure (p_i) of the i components of the Universe, through the Friedmann equations derived from General Relativity [8]:

$$\left(\frac{\dot{a}}{a}\right)^2 = \frac{8\pi G}{3}\rho_{\text{tot}} - \frac{kc^2}{a^2} \tag{1.1}$$

$$\left(\frac{\ddot{a}}{a}\right) = -\frac{4\pi G}{3}\left(\rho_{\text{tot}} + \frac{3p_{\text{tot}}}{c^2}\right) \tag{1.2}$$

here $a(t)$ is the scale factor, a dimensionless function that describes the growth or contraction of distances over time; and k is the curvature constant that can take one of three values: $k = 1$ for a positive spatial curvature; $k = -1$ for a negative spatial curvature and $k = 0$ for a spatially flat Universe [8]. Energy densities are commonly expressed as fractions to the critical density ρ_c, defined as the the average energy

density required to ensure geometrical flatness.

$$\rho_c = \frac{3H(t)^2}{8\pi G} \quad \text{(critical density)} \tag{1.3}$$

$$\Omega_i = \frac{\rho_i}{\rho_c} \quad \text{(energy density parameter } i\text{)},$$

here $H = \frac{\dot{a}}{a}$ is the Hubble parameter, at first introduced by Hubble to describe the relationship between distance and redshifts of galaxies and provide evidence for an expanding Universe.[1] The current prevailing cosmological model is the ΛCDM model which postulates a geometrically flat Universe ($k = 0$) composed of standard baryonic matter, nearly collisionless cold dark matter, radiation and dark energy in the form of a cosmological constant Λ. By expressing eqs. 1.1 and 1.2 in terms of the fractional energy densities Ω_i, one finds that the scale factor $a(t)$ evolves according to:

$$H(t) = H_0\sqrt{\Omega_\gamma^0 a^{-4}(t) + \Omega_m^0 a^{-3}(t) + \Omega_\Lambda^0}^{\,[2]} \qquad \text{with} \quad \sum_i^{m,r,\Lambda} \Omega_i(t) = 1. \tag{1.4}$$

Hence the expansion rate, as modeled by Friedmann's equation, is determined by the dominant energy component Ω_i at each epoch.

The early Universe ($a \lll 1$) was radiation dominated, with both ordinary and dark matter thermalized, due to the repeated interactions with photons and with each other. As the Universe expanded, the average temperature of the Universe decreased. When it fell below the weak interaction scale, interactions between dark matter and the rest of the Universe became negligible, allowing the dark matter to cool and fall

---

[1] the redshift z refers to the stretching of the emitted wavelength of an electromagnetic radiation (such as light) and is defined as $z = \frac{\lambda_{\text{obs}} - \lambda_{\text{em}}}{\lambda_{\text{obs}}} = \frac{1}{a} - 1$ where λ_{em} and λ_{obs} are respectively the emitted and observed wavelength. In the picture of the expanding Universe, the redshift of electromagnetic waves is both a measure of physical distance and time and is caused by the travelling of such waves through an expanding space which stretches out their wavelength.

[2] The Ω_i^0 refer to the current values of the density parameters of baryonic and cold dark matter ($\Omega_m^0 \approx 0.3$), radiation ($\Omega_\gamma^0 \approx 0$) and the cosmological constant ($\Omega_\Lambda^0 \approx 0.7$). H_0 is the present value of the Hubble constant which in this paper is taken to be $H_0 = 70 \text{ km s}^{-1} \text{ Mpc}^{-1}$.

into gravitational potential wells which amplified the primordial inhomogeneities[3] and gave rise to the first structures [8].

After entering the matter-dominated era, when the temperature cooled sufficiently below the hydrogen ionization energy, protons and electrons combined to form neutral hydrogen atoms. This led to the decoupling of photons from matter, so that the photons were finally free to propagate instead of being constantly scattered by electrons and protons in the plasma. These relic photons form the Cosmic Microwave Background (CMB) also called the surface of last scattering, which it's described in further detail in Sec.1.2.

After decoupling, more baryonic matter was drawn together under the influence of the previously formed gravitational potential wells, as structures continued to form. Initially, this process can be understood through linear cosmological perturbation theory with primordial structures that act as small deviations $\delta = \frac{\delta \rho_m}{\rho_m}$ from a perfect homogeneous Universe. The growth of these fluctuations in the linear regime can be obtained by solving the equation:

$$\ddot{\delta} + 2H\dot{\delta} - 4\pi G \rho_m = 0, \tag{1.5}$$

which is derived by the hydro-dynamical equations of Newtonian physics for a fluid perturbed to first order around the Hubble flow [9]. Quickly, as the wells grew rapidly, non-linear and complex structures began to form in a hierarchical matter with the most massive objects, galaxies and clusters, forming last and in some cases still forming today. The gravitational collapse problem in the non-linear regime becomes more difficult and requires N-body simulations in order to infer the mean number density of halos in the Universe and the amplitude of the growth vs cosmic time [10].

---

[3]the nature of these primordial inhomogeneities is still unknown and could be attributed to the magnification of early quantum fluctuations via inflation or through some other mechanism.

In "recent" times, approximately 4 billion years ago, the Universe entered the dark energy-dominated area, which drives the current cosmological acceleration. According to the ΛCDM model, dark energy takes the form of a cosmological constant which implies that such acceleration will never cease, so that the matter of the Universe, from stars and galaxies to atoms and subatomic particles, and even spacetime itself, will be progressively torn apart ending up with a Universe so dilute to be regarded as empty [11].

1.1.2   Fundamentals of Galaxy Clusters

Galaxy clusters are the largest known gravitationally bound structures in the Universe, consisting of anywhere between hundreds and thousands of galaxies. They tend to have masses ranging between 10^{14}-$10^{15} M_\odot$, while their typical size is around 10^7ly.[4] 81% of the total baryonic mass is distributed in the hot intra-cluster medium (ICM) and only the remaining 19% makes up the stars in the galaxy clusters. This corresponds to ~ 3% of the total mass in clusters, taking into account dark matter, which constitutes 84% of the total mass[12]. The ICM can be thought of as a plasma that is nearly fully ionized due to the high temperatures created by the deep dark matter gravitational potential which heats up the gas to temperatures close to the virial temperature $kT \sim \frac{GMm_p}{R_v}$[5] , ranging between 1-15 keV[12].

Galaxy clusters form at the most extreme peaks in the matter density field and thus their abundance as a function of redshift and mass is an essential probe for testing models of the Universe, by setting constraints on the matter power spectrum and the nature and properties of dark energy.

---

[4]Recall ly stands for light years.

[5]Here m_p,M and R_v respectively stand for the mass of cluster and the mass and corresponding viral radius of the cluster.

To detect galaxy clusters and determine their size, mass and redshift, several methods were implemented based on the different wavelengths of electromagnetic radiation emitted by the ICM (e.g., optical and X-Ray surveys). One promising method that has increased in importance is finding clusters through the Sunyaev-Zel'dovich (SZ) effect on the CMB, (see Sec.1.2.1 for more details). In contrast with the observed cluster brightness in other wave bands, the amplitude of the SZ distortions is relatively redshift independent which makes this method particularly suited to investigate the Universe at high redshifts [3].

1.2 The Cosmic Microwave Background (CMB)

The Cosmic Microwave Background was predicted in 1948 by Ralph Alpher and Robert Herman and measured, for the first time, in 1964 by Arno Penzias and Robert Wilson from the Bell Labs, who observed a mysterious persistent and isotropic microwave background in their radio-wave antenna receiver[13]. As previously mentioned in Sec.1.1.1, the CMB is the lingering radiation emitted during the infancy of the Universe from the separation of matter and radiation, in the event known as decoupling. Its temperature map is shown in Figure 1.1 and approximately resembles a blackbody spectrum with uniform temperature $T \sim 2.7$ K and small spatial temperature anisotropies, which correspond to perturbations in the matter density across the sky. Specifically, regions denser of matter at the moment of the photon-decoupling experience a stronger gravitational redshift, which results in a slightly higher temperature due to the compression of the primordial plasma into potential wells. These temperature variations are in the range of 1 part to 10^5 and have a characteristic angular scale of about 1 degree. In addition to these primary anisotropies, as a consequence of the primordial photon-baryon fluid density fluctuations, the CMB also presents secondary anisotropies, due to the interaction with a long list of objects, as
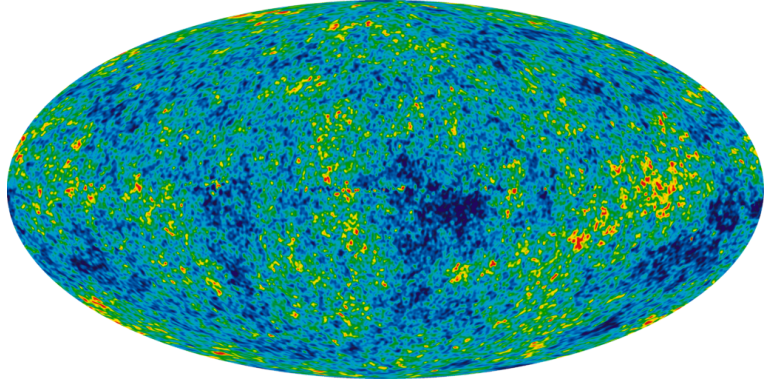
Figure 1.1: The detailed, all-sky picture of the infant Universe created from nine years of WMAP data. The image reveals 13.8 billion year old temperature fluctuations (shown as color differences) that correspond to the seeds that grew to become the galaxies. The signal from our galaxy was subtracted using the multi-frequency data. This image shows a temperature range of $\pm 200 \mu K$ [2].

the relic photons travel across the whole observable Universe. Indeed, the CMB is a backlight to all other sources of radiation between the LSS and the observer, which contaminate and distort the primordial signal at different scales. These distortions includes effects like: the integrated Sachs-Wolfe effect, due to photons moving through a gravitational potential; gravitational lensing, which redistributes the power toward small scales and the Sunyaev-Zel'dovich effect (SZE) due to inverse Compton scattering of CMB photons by hot gas in clusters [14]. Sensitive measurements of all of these and other effects can be studied from the temperature map of the CMB and provide valuable information about the non-linear Universe[6]. For the purpose of this paper, we are interested in the measurement of the SZE, which potentially constitutes the most powerful tool in the study of clusters properties, given its approximate redshift independence.

---

[6]Specifically a powerful method to extract this information is to examine the statistical properties of the temperature fluctuations by computing the two-point correlation function in angular space, the so-called CMB power spectrum. For a recent review on this topic refer to [15].

1.2.1 The Sunyaev-Zel'dovich effect (SZE)

The SZ effect is a small spectral distortion of the cosmic microwave background (CMB) spectrum caused by the scattering of the CMB photons off a distribution of high energy electrons, such as that provided by the ICM of galaxy clusters[3]. The resulting inverse Compton scattering boosts the energy of the CMB photon approximately by $\frac{k_B T_e}{m_e c^2}$, causing a small distortion of $\sim < 1$ mK in the CMB spectrum as shown in Fig.1.2 [3].
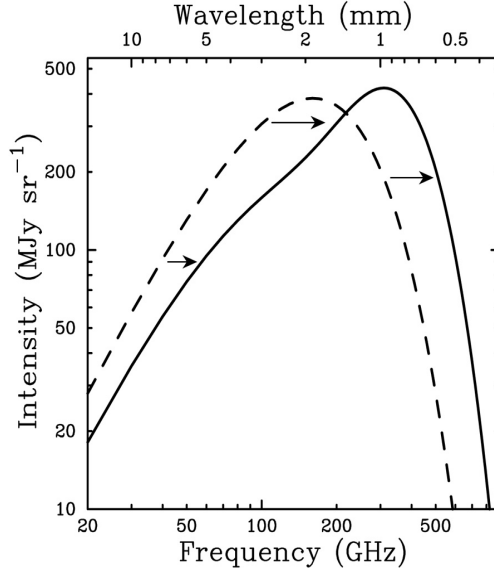
Figure 1.2: The CMB spectrum, undistorted (dashed line) and distorted by the Sunyaev-Zel'dovich effect (solid line). The SZ effect distortion shown is for a fictional cluster 1000 times more massive than a typical massive galaxy cluster [3].

One can express the SZ spectral distortion of the CMB as a temperature change ΔT_{SZE} at dimensionless frequency $x = \frac{h\nu}{k_B T_{CMB}}$ according to:

$$\frac{\Delta T_{SZE}}{T_{CMB}} = f(x)y, \tag{1.6}$$

where y is the Compton-y parameter which can be thought of as the product between the number of scatterings that a photon goes through and the fractional energy gain given by each of the collisions ($\sim \frac{k_B T_e}{m_e c^2}$). y is also cluster model-dependent,

7

characteristic that plays a crucial role in the cluster characterization, as we will show in more detail in Chapter 2. The frequency dependence function of the SZ-effect $f(x)$, if one accounts for the relativistic correction δ_{SZE}, is given by [3]:

$$f(x) = \left(x\frac{e^x+1}{e^x-1} - 4\right) \times (1 + \delta_{\text{SZE}}(x, T_e)). \tag{1.7}$$

Generally, the size of the SZ effect is proportional to the volume-integrated thermal pressure and it is independent of redshift, a feature which makes it a very powerful tool for investigating the distant Universe[3]. If the cluster is moving with respect to the CMB rest frame, there is an additional kinetic spectral distortion caused by the Doppler effect of the cluster bulk velocity on the scattered CMB photons, whose size is proportional to $\frac{v_{\text{pec}}}{c}$[3]. Finally, the scattering of the CMB photons by the electrons of the hot ICM can also result in a measurable polarization of the signal in the order of τ_e times the SZ signal, where τ_e is the optical depth.

1.2.2   CMB Polarization

Fluctuations in temperature are not the only anisotropies of great interest, in fact the CMB signal is also linearly polarized due to Thompson scattering of photons off free electrons in the surface of last scattering [16]. This faint polarization signature, of order of 1 μK, was first detected by the DASI experiment [17] and since it has been observed by many other experiments. Polarized signals are typically expressed in terms of the Stokes parameters, a coordinate dependent basis that decomposes the electric field into an intensity component I and two linear polarization components

Q and U such that [16]:[7]

$$I = |E_x|^2 + |E_y|^2 \tag{1.8}$$

$$Q = |E_x|^2 - |E_y|^2 \tag{1.9}$$

$$U = E_x E_y^* + E_y E_x^*. \tag{1.10}$$

The total linear polarization, P, is then given by:

$$P = \sqrt{Q^2 + U^2}. \tag{1.11}$$

In the context of the CMB, the Stokes parameters Q and U are typically decomposed into the so called E-modes and B-modes[8]. This decomposition is a linear transformation of the Q-U Stokes fields and it is not dependent on the choice of coordinates. E-mode patterns are either tangential or radial and caused by scalar temperature perturbations (i.e. density fluctuations in the early Universe), while B-mode patterns are spiral and caused by tensor perturbations (i.e. primordial gravitational waves)[16].

1.3 The Atacama Cosmology Telescope (ACT)

The Atacama Cosmology Telescope (ACT) is a 6m telescope located at 5200 m in the Atacama desert in northern Chile. The site was chosen for its excellent atmospheric transparency and access to both southern and northern skies which makes it among the best sites in the world for ground-based observations at millimetre wavelengths. Given the high resolution of the CMB observations acquired through this telescope, the Sunyaev-Zeldovich effect (SZ), imprinted by clusters on the CMB, is measurable

---

[7]There is also a 4th parameter V representing the circular polarization component which we do not consider since there is no mechanism by which circular polarization is generated in the CMB.

[8]This naming convention arises from the analogy of the curl free and divergence free properties of electric (E-modes) and magnetic (B-modes) fields [18, 19].

and can be used to detect and characterize clusters of galaxies on the celestial equator where the observations were concentrated. The telescope has three 1024 element arrays of transition edge sensors and observes the sky in four frequency bands at 90 GHz, 150 GHz and 220 GHz simultaneously with arcminute resolution. Specifically, the FWHM[9] of the point spread functions for the 90, 150 and 220 GHz arrays are approximately 2.1', 1.4' and 1.1', respectively.

For this study, we used the S18dn catalog of $2,869$ confirmed clusters[10] on a $15,170$ square degree deep, contiguous region spanning from $-60°$ to $+20°$ in declination and across the whole sky in right ascension, as shown in Fig.1.3.
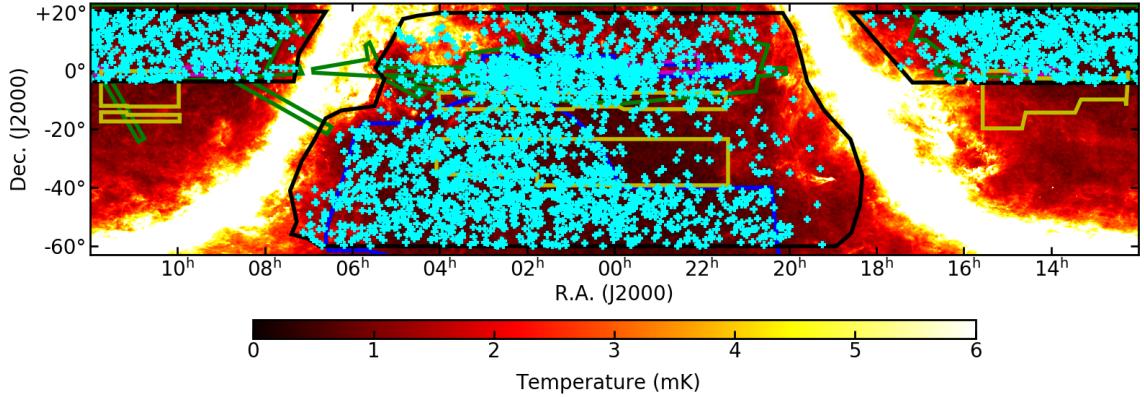
Figure 1.3: The figure shows the portion of the ACT equatorial survey region considered in this work, overlaid on the thermal Planck map in mK. The field spans from $-60°$ to $+20°$ in Declination (Dec.) and across all sky in Right Ascension (R.A.). The dots in light blue provide the location in terms R.A. and Dec of all confirmed 2869 detected clusters from the ACT S18dn cluster sample. Credit: [Professor Matthew Hilton]

---

[9]FWHM stands for Full Width at Half Maximum.

[10]The S18dn catalog contains already $3,100$ confirmed clusters, of these 231 don't have a mass estimate and or a redshift confirmation yet. Hence, in this work we only consider the remaining $2,869$ clusters that have already an associated mass and redshift known.

1.3.1 Galaxy Cluster Detection

In addition to the temperature decrements from galaxy clusters, the ACT maps contain contributions from CMB, radio point sources, atmospheric fluctuations and other sources of noise. Thus, as described thoroughly in [7], a series of matched filters in Fourier space $\Psi_{\theta_{500}}(k)$ is used to amplify the signal for cluster scale and suppress the large scale fluctuations in the map. The signal template adopted for the intra-cluster gas pressure profile is the Universal Pressure Profile (UPP) by Arnaud et. al [4], which includes mass dependence in the profile shape and has been calibrated to X-ray observations of nearby clusters [6]. To maximize the detection efficiency of clusters at different scales, 24 matched filters were applied corresponding to different combinations of the cluster redshift and inferred mass [7]. From the matched filters, real-space filter kernels are constructed and then applied by convolution to the maps. This method has the advantage of simplifying the analysis of split sections from larger maps and the computation of the survey selection function [7]. To obtain such kernels, the filters are truncated at $7'$ radius which then requires the addition of an high pass filter on the maps in order to remove noise at larger scales than $7'$. Finally, the real-space matched filter kernel are normalized such that they return in each pixel the cluster central decrements $\Delta T(x)$ and the overall noise $\sigma(x)$ [7].

Cluster candidates are then identified as all pixels with signal to noise ratio[11] SNR$= \frac{-\Delta T(x)}{\sigma(x)} > 4$ and cross-matched, assembling the catalog at each cluster scale using a $1.4'$ matching radius[7].

---

[11]The maximum SNR across each filter scale is adopted for cluster detection. However as discussed in [6] and in Sec.2.2 of this work, a single reference filter scale of $2.4'$ is also adopted (SNR$_{2.4}$) to obtain the SZ-mass scaling relations and infer the selection function.

1.3.2 Redshift Confirmation

One of the benefits of the location of the ACT equatorial cluster sample is the significant overlap with other public surveys which is a crucial aspect to confirm the cluster detection and determine independently their redshift. For many objects, the redshift measurements come directly from these overlapping surveys, such as SDSS [20], S82 [21] and VIPERS [22]. These surveys are also used to provide confirmation on the redshift estimated through automated methods for cluster finding.

Specifically, the ACT collaboration developed an algorithm, named zCluster,[12] thoroughly described in [7], which was applied to SDSS [20], S82 [21], and the CFHTLS survey data[15] to estimate cluster redshifts using multiband optical/IR photometry. In addition, to obtain more precise estimates for clusters at higher redshift ($z > 0.5$), beyond the typical depth of the major public surveys, the ACT collaboration performed follow-up observations which included optical/IR imaging with the Southern Astrophysical Research Telescope (SOAR) and the Astrophysical Research Consortium 3.5 m telescope at the Apache Point Observatory (APO), and optical spectroscopy using the SALT [7].

---

[12]https://github.com/ACTCollaboration/zCluster

[13]specifically the photometric catalogs of the CFHTLenS project [23, 24].

Chapter 2

Cluster Characterization

2.1 The Compton y-parameter and other SZ-quantities of interest

As it was discussed in Sec.1.2, the ACT cluster survey provides only two parameters independently determined: the thermal decrements ΔT_{SZE} from the SZ effect and the redshift z. For the purpose of obtaining cosmological constraints from SZ surveys, the masses of the detected clusters and their distribution are crucial parameters (see Ch.3). Thus, it becomes important to model the SZ signal and determine the mass scaling relation with z and ΔT_{SZE}. The Compton y-parameter y is a convenient value to use in the scaling relations, it is related to ΔT_{SZE} through eq.1.6 and hence, based only the non-relativistic SZ treatment, it can be estimated as:

$$y(\theta) = \frac{\Delta T_{SZE}(\theta)}{T_{\text{CMB}}} \Big(x \frac{e^x + 1}{e^x - 1} - 4 \Big)^{-1}. \tag{2.1}$$

Now, since y is defined as the product of the fractional energy change of a photon per scattering times the mean number of scatterings, one can write:

$$y = N \times \frac{\delta E}{E} = \int_{-\infty}^{+\infty} n_e \frac{k_B T_e}{m_e c^2} \sigma_T dl, \qquad (2.2)$$

where the total number of collision N was derived given $dN = n_e dV = n_e \sigma_T dl$, with n_e equal to electron number density, and σ_T the Thomson scattering cross section. Assuming the ideal gas law $P = n_e k_B T_e$, where k_B is the Boltzmann constant, eq.2.2 becomes:

$$y = \frac{\sigma_T}{m_e c^2} \int_{-\infty}^{+\infty} P dl. \qquad (2.3)$$

This shows that the Compton y-parameter, and consequently the mass scaling relation derived from it, are a measure of the intra-cluster gas pressure profile adopted. In Sec.2.2, we present first the adiabatic model which provides very simple and intuitive relations; then two improved scaling models: (1) the Isothermal β model and (2) the Universal Pressure Profile, which is ultimately the one implemented to characterize the SZ signal in the ACT catalog. Before moving on in this discussion, in Sec.2.1.1 we define and motivate the parameters commonly used to characterize clusters and their pressure profiles.

2.1.1   The $\Delta = 500$ parameters

In order to establish relationships between mass, SZE flux, and other cluster properties, one needs to define a radius out to which all the quantities will be calculated. A meaningful definition of the size a cluster is the radius within which the matter within the gravitational halo is in mutual virial equilibrium, so that the mass of the cluster can then be defined as the total mass within this radius, appropriately named the virial radius. The extreme over-densities of matter within the cluster make it fairly difficult to define and measure such equilibrium and the corresponding virial

radius r_v. Thus, cluster masses are practically defined with respect to some radius within which the structure has a particular overdensity relative to the critical density ρ_c at the cluster redshift. For an overdensity parameter Δ, R_Δ is the radius of the sphere within which the cluster density is $\Delta \times \rho_c(z)$. Then the cluster mass M_Δ is simply:

$$M_\Delta = \Delta \times \frac{4\pi \rho_c(z) R_\Delta^3}{3}. \tag{2.4}$$

For X-ray and SZ studies, it is conventional to use $\Delta = 500$, denoting the mass and radius respectively as M_{500c} and R_{500c} [1]. Similarly, the angular size of the cluster is denoted by the symbol θ_{500c} and defined in terms of the characteristic radius by:

$$\theta_{500c} = \frac{R_{500c}}{D_A(z)}, \tag{2.5}$$

where $D_A(z)$ is the angular diameter distance (see Appendix A for its full derivation). Another useful quantity, which turns out to provide a more accurate scaling relationship with the mass [4], is the integrated Compton parameter over a sphere of radius R_{500c}, Y_{500c}:

$$Y_{500c} = \frac{\sigma_T}{m_e c^2} \int_{V_{500}} P dr^3 = \int_{\Omega_{500}} y d\Omega. \tag{2.6}$$

2.2 The Cluster Pressure Profile

2.2.1 The Adiabatic Model

To build some intuition about the expected relations between the parameters defined above and y, it is useful to introduce at first the simple adiabatic model which assumes the cluster to be spherical, uniform and isotropic. These symmetries allow us to use the virial theorem, which states that for a stable, self-gravitating, spherical

---

[1]The viral radius in this formalism is defined by $\Delta = 200$ with typical values of $1 - 3 \mathrm{Mpc}$ [25].

distribution of equally massive objects[2], their total kinetic energy is equal to minus $\frac{1}{2}$ times the total gravitational potential energy ($K = -\frac{1}{2}U$). Moreover, given the assumptions on the geometry of clusters, their uniformity and isotropy, one also knows that a cluster of mass M at temperature T has potential energy $U = -3\frac{GM^2}{5R}$ and kinetic energy $K = \frac{3}{2}NkT$, where $3N$ equals to the number of degrees of freedom. For a cluster of mass M, $N \approx \frac{M}{m_p}$ where we approximated the average mass of a particle inside the cluster to that of the proton. Combining these relations with the virial theorem and substituting $R = \left(\frac{M}{\frac{4}{3}\pi\rho}\right)^{\frac{1}{3}}$ one gets:

$$3\frac{M}{m_p}k_BT_e = 3\frac{GM^2}{5R} \quad \Rightarrow \quad T_e = \frac{m_pG}{5k_B}\left(\frac{4}{3}\pi\rho\right)^{\frac{1}{3}}M^{\frac{2}{3}} \propto M^{\frac{2}{3}}. \tag{2.7}$$

Now given eq.2.2, the pressure P will simply be given by the ideal gas law and will be thus proportional to T_e and brought outside of the integral in dl. To obtain y, one must therefore solve the integral $\int_{-\infty}^{+\infty} dl$ along the line of sight. This integral, in terms of the radius of the cluster R is approximately given by:

$$\int_{-\infty}^{+\infty} dl = 2\lim_{d\to 0}\int_{d}^{+\infty}\frac{r}{\sqrt{r^2 - d^2}}dr \approx 2\lim_{d\to 0}\int_{d}^{R}\frac{r}{\sqrt{r^2 - d^2}}dr \approx 2\int_{0}^{R}dr = 2R. \tag{2.8}$$

Substituting our results from eq.2.7 and 2.8 in eq.2.2 one gets:

$$y = \frac{2Gm_pn_e\sigma_T}{5m_ec^2}M \propto M. \tag{2.9}$$

From this we can conclude that, under the adiabatic pressure model, the Compton y parameter of a uniform and isotropic cluster is correlated linearly to its mass M.

To scale the y-parameter in terms of M_{500c}, one can then combine eq.2.4 with the fact that the electron number density can be written in terms of the mass density

---

[2]stars, galaxies, clusters, etc.

and the mass of an electron as $n_e = \frac{\rho_{500c}}{m_e}$ such that:

$$y = \frac{2Gm_p\sigma_T}{5m_e^2c^2}\left(500\frac{3H_0^2E(z)^2}{8\pi G}\right)M_{500c} \propto E(z)^2M_{500c};$$

$$y(M_{500c}, z) = \frac{75H_0^2m_p\sigma_T}{\pi m_e^2c^2}M_{500c}(\Omega_m(1+z^3)+\Omega_\Lambda). \tag{2.10}$$

Thus, introducing the parameter M_{500c} emphasizes an explicit dependence between the central Compton-y parameter and the redshift z. In deriving eq.2.10, we used the definition of critical density $\rho_c(z) = \frac{3H_0^2E(z)^2}{8\pi G}$, where $E(z) = H(z)/H_0$ is the ratio of the Hubble parameter at z to its present value $H_0 = 70$ km s^{-1} Mpc^{-1} (see Appendix A for more details).

2.2.2 The Isothermal β Model

The isothermal β model, at first introduced by Cavaliere and Fusco-Femiano [26], considers the simplified case of an isothermal spherical cluster in hydrostatic equilibrium (no net force applied to the matter in the cluster), such that the gravitational potential ϕ is balanced by the internal pressure P of the gas according to:

$$\frac{d\phi(r)}{dr} = -\frac{1}{\rho(r)}\frac{dP(r)}{dr}. \tag{2.11}$$

Here, in contrast with the simple adiabatic model just presented, the density as well as the pressure are not constant throughout the cluster, but rather a function of its radius[3]. Now, we can express the mass density $\rho(r)$ of the gas in the ICM as the product of the electron number density $n_e(r)$ with the mean gas mass per electron μ_e, such that: $\rho(r) = n_e(r)\mu_e$, with $\mu_e \approx 1.14m_p$ and m_p equal to the mass

---

[3]in eq.2.11 the right-hand side represents the force per unit volume f on the matter in the cluster, defined as $f = \nabla P(\rho) = \frac{1}{\rho(r)}\frac{dP(r)}{dr}$ [27].

of the proton[4]. Assuming the gas follows the ideal gas law: $P(r) = n_e(r)k_B T$ we can rewrite eq.2.11, also exploiting the fact that the gas temperature T is constant given the assumption of isothermality:

$$\frac{d\phi(r)}{dr} = -\frac{k_B T}{n_e(r)\mu_e}\frac{dn_e(r)}{dr} = -\frac{k_B T}{\mu_e}\frac{d\ln[n_e(r)]}{dr}. \tag{2.14}$$

Given that dark matter makes up the majority of the material in clusters, one can estimate the pressure distribution by looking at properties of the dark matter inside the cluster. Specifically, assuming that clusters have an isotropic velocity dispersion function[5], the dark matter pressure distribution $P_{DM}(r)$ can be expressed as the flux of momentum through a given area which gives us $P_{DM}(r) = \sigma^2 \rho_{DM}(r)$, where $\rho_{DM}(r)$ is the dark matter density and σ^2 the velocity dispersion [26]. Plugging this result back into eq.2.11 and integrating over r, after combining it with eq.2.14, we get:

$$\frac{d\phi(r)}{dr} = -\sigma^2\frac{d\ln\rho_{DM}(r)}{dr}$$

$$\text{by eq.2.14:} \quad \frac{k_B T}{\mu_e}\frac{d\ln[n_e(r)]}{dr} = \sigma^2\frac{d\ln\rho_{DM}(r)}{dr}$$

$$\text{integration in } r \Rightarrow n_e(r) = n_e^0 \rho_{DM}^\beta; \tag{2.15}$$

---

[4]This result follows from the assumption of a primordial composition of elements for the intra-cluster gas, with ~ 76% H and ~ 24% He, such that:

$$n_e = \left(\frac{1}{1}\times 0.76 + \frac{2}{4}\times 0.24\right)\frac{\rho}{m_p} \approx 0.88\frac{\rho}{m_p}n_e = \frac{\rho}{\mu_e} \tag{2.12}$$

$$\Rightarrow \boxed{\mu_e \approx 1.14 m_p} \tag{2.13}$$

where the fractions in the brackets express the ratios of the number of electrons to the nucleons for both hydrogen and helium: 1 electron and 1 proton for the hydrogen, against 2 electron, 2 protons and 2 neutrons for the helium.[27]

[5]This assumption implies that the line-of-sight velocity dispersion $\sigma^2 = \frac{4\pi}{3}\int f(v)v^4 dv$ where $f(v)$ is the Maxwellian velocity distribution.

where we defined the dimensionless parameter $\beta = \sigma^2 \mu_e / k_B T$, which essentially measures the ratio of energy per unit mass in galaxies ($\sim \sigma^2 \mu_e$) vs gases ($\sim k_B T$) in a cluster.

The dark matter density ρ_{DM} should be proportional to the galaxy number density which is well approximated by the function $\left[1 + \left(\frac{r}{r_c}\right)^2\right]^{-\frac{3}{2}}$, derived empirically by King from his studies of the Coma cluster [28]. Here, r_c is the core radius of the cluster, defined as $r_c = \sqrt{\frac{2\sigma^2}{4\pi G \rho_{GO}}}$, where ρ_{GO} is the central density of galaxies. Putting everything together and recalling the proportionality between $n_e(r)$ and the pressure profile $P(r)$, we obtain the central result of the isothermal β model:

$$P(r) = P_0 \left[1 + \left(\frac{r}{r_c}\right)^2\right]^{-\frac{3\beta}{2}}. \tag{2.16}$$

Given the definition of the Compton y-parameter in eq.2.3 we can integrate this result to obtain the relationship between y and the linear size of the cluster d:

$$y(d) = \frac{2\sigma_T P_0}{m_e c^2} \int_d^{R_{500c}} \frac{r}{\sqrt{r^2 - d^2}} \left[1 + \left(\frac{r}{r_c}\right)^2\right]^{-\frac{3\beta}{2}} dr$$

$$\text{for } d \lll R_{500c} \rightarrow \quad \approx \frac{\sigma_T P_0}{m_e c^2} \int_d^{+\infty} \left[1 + \left(\frac{r}{r_c}\right)^2\right]^{-\frac{3\beta}{2}} dr$$

$$\boxed{y(d) = y_0 \left[1 + \left(\frac{d}{r_c}\right)^2\right]^{\frac{1}{2} - \frac{3\beta}{2}}} \tag{2.17}$$

where $y_0 = 2\frac{P_0 \sigma_T}{m_e c^2} r_c \sqrt{\pi} \frac{\Gamma(\frac{3}{2}\beta - \frac{1}{2})}{2\Gamma(\frac{3}{2}\beta)}$[6]. Typical β-model parameters are $\beta \sim 1$ and $r_c \sim 0.1 - 1\mathrm{Mpc}$. Figure 2.1 shows the β-model radial pressure profile for these typical values, in comparison with the universal pressure profile that is presented in the next section. The relationship between y and the angular size of the cluster θ is equivalent with $d \rightarrow \theta$ and $r_c \rightarrow \theta_c$, according to the definition of $\theta = \frac{d}{D_A(z)}$.

---

[6] Note that in solving the integral and going from the second to the third line in the derivation, we expanded to first order the hypergeometric function $_2F_1[\frac{1}{2}, \frac{3\beta}{2}, \frac{3}{2}, -\frac{d^2}{r_c^2}]$ contained in the solution of the integral [29].

Finally, to obtain the relation for the mass M_{500c} of the cluster, one must simply recall that $P \propto n_e \propto \rho$ and then integrate eq.2.16 on the spherical shell of radius R_{500c} [29]:

$$M_{500c} = \rho_0 \int_0^{R_{500c}} \left[1 + \left(\frac{r}{r_c}\right)^2\right]^{-\frac{3\beta}{2}} 4\pi r dr \qquad (2.18)$$

$$= 4\pi\rho_0 \frac{r_c^2 - r_c^{3\beta}\left(R_{500c}^2 + r_c^2\right)^{1-\frac{3\beta}{2}}}{3\beta - 2},$$

where ρ_0 is the central density of the cluster.
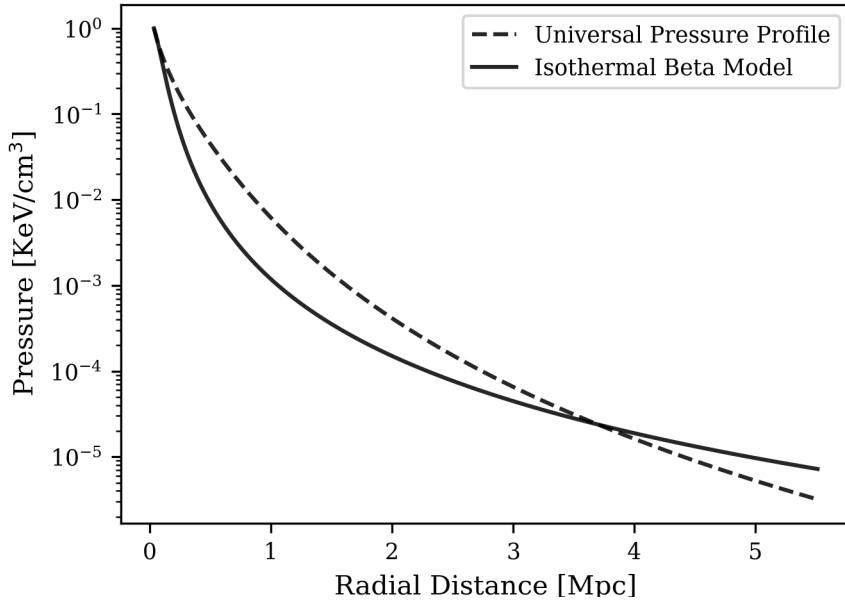
Figure 2.1: The plot shows a comparison between the radial pressure profile of a typical β-model cluster (solid curve), with $\beta = 1$, $r_c = 0.1$ Mpc, $M_{500c} = 10^{14} M_\odot$, and $z = 0.5$, to the Arnaud et al. [4] universal pressure profile (dashed curve) with the same values of z, M_{500c}, and $R_{500c} = 0.8$ Mpc. The profiles are normalized and shown in log scale. We can note that the UPP has a faster falloff at large radii, as well as becoming singular rather than flat at small distances.

2.2.3 The Universal Pressure Profile (UPP)

The isothermal β model was based on three major assumptions, that clusters are: (1) spherical, (2) isothermal in (3) hydrostatic equilibrium. Clearly these assumptions cannot apply in all regimes. For instance, the model fails to take ellipticity and other irregularities in the shape of clusters into account as this would violate (1) [27]. Though this may be a fairly easy extension to make, the main probelmatics remain and are represented by condition (2) and (3). Specifically, at large radii, (2) is violated as the temperature must fall off to the background temperature of the universe rather than remaining constant [27]. Hence, in this regime, the β model will always underestimate the dropoff of the pressure profiles for any cluster under consideration. Similarly, hydrostatic equilibrium can only apply in the regime where the matter has become virialized, namely within the virial radius r_v. Thus at large radii $> r_v$ also the assumption of hydrostatic equilibrium (3) ceases to apply and the β model becomes an inadequate description of the cluster profile.

To overcome such inadequacies of the isothermal β model, Navarro, Frenk, and White (NFW) proposed a pressure profile model fitted for dark matter halos in clusters, based on the results of N-body simulations [30]. The NFW profile extends upon the β model by adding supplementary parameters and it allows pressure profiles to became singular rather than flat at small radii [27]. Its generalized form is [31]:

$$p(x) = \frac{P(r)}{P_{500}} = \frac{P_0}{x^\gamma \left(1 + x^a\right)^{\frac{\beta - \gamma}{\alpha}}}. \tag{2.19}$$

Here $x = \frac{r}{r_s}$ and $r_s = \frac{R_{500c}}{c_{500}}$. The parameters (γ, α, β) are respectively the central slope $(r \ll r_s)$, intermediate slope $(r \sim r_s)$ and outer slope $(r \gg r_s)$, of the profile with the dimensionless parameter c_{500} that defines the transition between these regions [4].

Using a sample of 33 clusters from the REFLEX catalogue, all with $z < 0.2$, Arnaud et al.[4] calculated the best fitted parameters of the generalized NFW profile which

correspond to:

$$[P_0, c_{500}, \alpha, \beta, \gamma] = [8.403 h_{70}^{-\frac{3}{2}}, 1.177, 1.0510, 5.4905, 0.3081]. \tag{2.20}$$

Following [31] and [32], Arnaud et al. defined the characteristic pressure P_{500} from a standard self-similar model, purely based on gravitation, obtaining that:

$$P_{500} = 1.65 \times 10^{-3} H(z)^{\frac{8}{3}} \left[\frac{M_{500c}}{3 \cdot 10^{14} \mathrm{M}_\odot} \right]^{\frac{2}{3}} \mathrm{keVcm^{-3}}. \tag{2.21}$$

Starting from this scaling relation, they derived empirically the mass and redshift dependence of the scaled profile $P(r)$, which results in [4]:

$$P(r) = P_{500} \times \frac{P_0}{(c_{500}x)^\gamma \left(1 + (c_{500}x)^\alpha\right)^{\frac{(\beta-\gamma)}{\alpha}}} \times \left[\frac{M_{500c}}{3 \cdot 10^{14} M_\odot} \right]^{\alpha_p + a_p'(x)}, \tag{2.22}$$

where in this case $x = \frac{r}{R_{500c}}$ and α_p and $\alpha_p'(x)$ are coefficients empirically determined to be:

$$\alpha_p = 0.12, \qquad \alpha_p'(x) = 0.10 - (\alpha_p + 0.10) \frac{x^3}{(0.125 + x^3)}. \tag{2.23}$$

The Compton y-parameter cannot be expressed in an analytic form and may only be computed according to its definition in eq.2.3 through numerical methods of integration.

Chapter 3

Cluster Abundance and Cosmological Analysis

As discussed in Sec.1.1.2, the evolution of the cluster abundance as a function of mass and redshift is a very useful probe of the fundamental cosmological parameters. The formation of the large–scale dark matter potential wells of clusters involves mostly gravitational physics [33]. Hence, the abundance of clusters N_{tot} and their distribution in redshift $\frac{dN}{dz}$ should be determined purely by the geometry of the universe and the power spectrum of initial density fluctuations [34, 35, 36]. Exploiting this relation, measurements of the cluster abundance can be used to constrain the amplitude σ_8 of the power spectrum on cluster scales of 8 h^{-1} Mpc and the matter density parameter Ω_m. Given the surface-brightness redshift-independence of the SZ effect, selected cluster samples using this method also constitute a powerful probe for tests of the dark energy paradigm and to set constraints on its equation of state parameter w_{DE}[1].

---

[1]This property of the SZ effect allows us to obtain nearly mass-limited samples at arbitrary redshifts and thus study the evolution of the cluster abundance at the time when dark energy begins to contribute significantly to the energy budget of the universe ($z \sim 1$). Note, the definition of the universe element i equation of state parameter w_i is: $w_{\text{i}} = \frac{p_{\text{i}}}{\rho_{\text{i}}}$. Hence in the case of a cosmological constant $w_{DE} = w_\Lambda = -1$.

In recent years, constraints on cosmological parameters from SZ cluster surveys have been obtained by the Atacama Cosmology Telescope (ACT) [7, 6], the South Pole Telescope (SPT) [37] and the Planck satellite [38]. To extract cosmological constraints from these surveys, it is required a sophisticated likelihood analysis whose critical ingredient is the underlying likelihood that the galaxy cluster statistics of the observed sky would be realized within a particular universe [39]. Performing this type of analysis goes beyond the scope of this thesis. Hence here, to simplify the discussion, we assume that all the characteristic features of a survey (e.g., selection function, depth as a function of the sky position, etc.) can be fully encoded in the value of a mass threshold M_{thr} and effective survey area $\Delta\Omega_{\mathrm{eff}}$ [2]. We then derive in Sec.3.2.3 the redshift cluster distribution of the ACT S18dn cluster sample and fit it to the ΛCDM theoretical prediction using a least-squares method with three free parameters: σ_8, $\Delta\Omega_{\mathrm{eff}}$ and M_{thr}.

3.1 Theoretical basis for Cluster Cosmology

Within a given survey enclosed in a solid angle $\Delta\Omega$, the expected number of clusters per redshift with mass above M_{thr} can be calculated by:

$$\frac{dN}{dz}(M > M_{\mathrm{thr}}) = \Delta\Omega \frac{dV}{dzd\Omega}(z) \int_{M_{\mathrm{thr}}(z)}^{\infty} dM \frac{dn}{dM}(M, z), \qquad (3.1)$$

---

[2]see Sec.3.2.2 for more details on the implications of this assumption and the physical meaning that these two quantities take on.

where $\frac{dn}{dM}$ is the halo mass function and $\frac{dV}{dzd\Omega}$ is the comoving volume element [3]. The comoving volume V is the volume measure in which number densities of non-evolving objects locked into the Hubble flow are constant with redshift [40]. It is given by [10]:

$$\frac{dV}{dzd\Omega} = D_A^2 c \frac{(1+z)^2}{H(z)},$$ (3.4)

where D_A is the angular diameter distance at redshift z and $H(z)$ is the expansion rate of the universe as defined in eq.1.4 with $a \to \frac{1}{(1+z)}$ [4].

3.1.1 The Halo Mass Function

As emphasized by eq.3.1, the mass function is the primary input to determining the expected cluster count for a given survey and it is defined as the number density of halos at a given mass. Today, our theoretical understanding of halos formation and their properties (the mass, spatial distribution, and inner profiles) is still relatively crude, hence research heavily relies on careful numerical studies in order to obtain accurate results. In 1974, Press and Schechter sketched a simple theoretical framework [41] which served as the base for more complex and extended models later proposed. Press-Schechter (PS) theory provides the analytic formula for the build-up of halos where the initial field of density fluctuations is smoothed using a spherically symmetric filter[5] centered on a given position to obtain information about the likeli-

---

[3]To get an intuition for this formula one can simply think of it as a pure differential obtained by the chain rule:

$$\frac{dN}{dz} = \int \frac{dN}{dVdM} dM \cdot \Delta\Omega \frac{dV}{dzd\Omega}$$ (3.2)

$$= \Delta\Omega \frac{dV}{dzd\Omega} \cdot \int \frac{dn}{dM} dM \quad \text{with } n = \frac{N}{V}.$$ (3.3)

[4]For a graphic representation see Appendix A.

[5]The examined window functions were a sharp k-space filter, a Gaussian filter and a top hat filter, with the latter being the most popular given the simplified correlation that arises between δ at different R scales which helps in computing the desired statistics directly.

hood of later collapse on varying scales [41]. The theory makes several assumptions: (1) the mass density field δ_m is described by a Gaussian distribution, (2) that each object is formed by gravitational collapse of mass density fluctuations, and (3) that such fluctuations can be treated with a linear approximation through the spherical collapse model [41]. According to the PS formalism, by smoothing the linear density perturbations on some mass scale M, the regions where the smoothed density field exceeds the critical over-density for collapse $\delta_c \approx 1.69$[6] correspond to collapsed objects of mass greater than M. Hence, the probability that a given point lies in a region where $\delta > \delta_c$ is:

$$P\left(\delta > \delta_c | M\right) = \frac{1}{\sqrt{2\pi}\sigma_M} \int_{\delta_e}^{\infty} \exp\left[-\delta^2/2\sigma_M^2\right] d\delta, \tag{3.5}$$

where σ_M is the variance of the density field filtered on scale R which encloses M[7] and given by:

$$\sigma_M^2 = \frac{1}{2\pi^2} \int_0^{\infty} P(k,z)\tilde{W}_R^2(k)k^2 dk, \tag{3.6}$$

with $P(k,z)$ and $\tilde{W}_R(k)$ corresponding respectively to the matter power spectrum and the Fourier transform of the filter function, here taken to be a top hat,

$$\tilde{W}_R(k) = \frac{3}{(kR)^3}\left[\sin(kR) - (kR)\cos(kR)\right]. \tag{3.7}$$

The crucial step in the derivation of the PS mass function formula is to set $P\left(\delta > \delta_c | M\right)$ in eq.3.5 equal to the fraction of the universe condensed into objects

[6]this is the value calculated in the linear approximation for a Einstein-de Sitter (EdS) Universe which is still valid for the ΛCDM model, given the weakly dependence of δ_c on the cosmological model in this linear regime. For the extended derivation refer to Appendix B.

[7]The relation between R and M is simply $M = \frac{4\pi}{3}\rho_0 R^3$ where ρ_0 is the uniform background density

with mass greater than M (in short $P(>M)$) multiplied by 2[8]. The mass function is then defined as the comoving number density per unit mass which is obtained by differentiating $P(>M)$ with respect to M and converting from the volume fraction to mass fraction multiplying by $\frac{\rho_0}{M}$ [10]. This yields the famous Press-Schechter mass function formula [41]:

$$\frac{dn}{dM} = \sqrt{\frac{2}{\pi}} \frac{\rho_0}{M} \frac{\delta_c}{\sigma^2} \frac{d\sigma}{dM} \exp\left[-\frac{\delta_c^2}{2\sigma^2}\right]. \tag{3.8}$$

That said, while qualitatively correct, the P-S mass function and numerical results are known to deviate in detail. Specifically, the PS function overestimates the abundance of halos at the low mass end and underestimates the abundance in the high mass tail [42]. Several models for the halo mass function have been proposed since, either by considering extensions of the Press-Schechter formalism [43, 44, 45] or by constructing a general fitting formula based on the results of numerical simulations [42, 46, 47]. In this paper, we use the mass halo function derived by Tinker et al [5]. In their work, they use a large set of collisionless cosmological simulations of flat ΛCDM cosmology to derive fitting functions for the mass function for virial masses in the range $10^{11}h^{-1}M_\odot \le M \le 10^{15}h^{-1}M_\odot$ for a wide range of over-densities Δ and redshift z. Their results improve on previous approximations by 10-20% and also show that the mass function, in contrast with the previously formulated models, cannot be represented by a universal fitting function at this level of accuracy [5].

The halo abundance takes the functional form:

$$\frac{dn}{dM} = f(\sigma) \frac{\rho_0}{M} \frac{d\ln \sigma^{-1}}{dM}, \tag{3.9}$$

---

[8]Originally the postulate from Press and Schechter in [41] set $P(\delta > \delta_c|M) = P(>M, t)$. However, such postulate predicts that only $\frac{1}{2}$ of all matter in the Universe is enclosed in collapsed halos as for $\sigma_M \to \infty$, $P(\delta > \delta_c|M) \to \frac{1}{2}$. To resolve the problem Press and Schechter added by brute force this factor of 2.
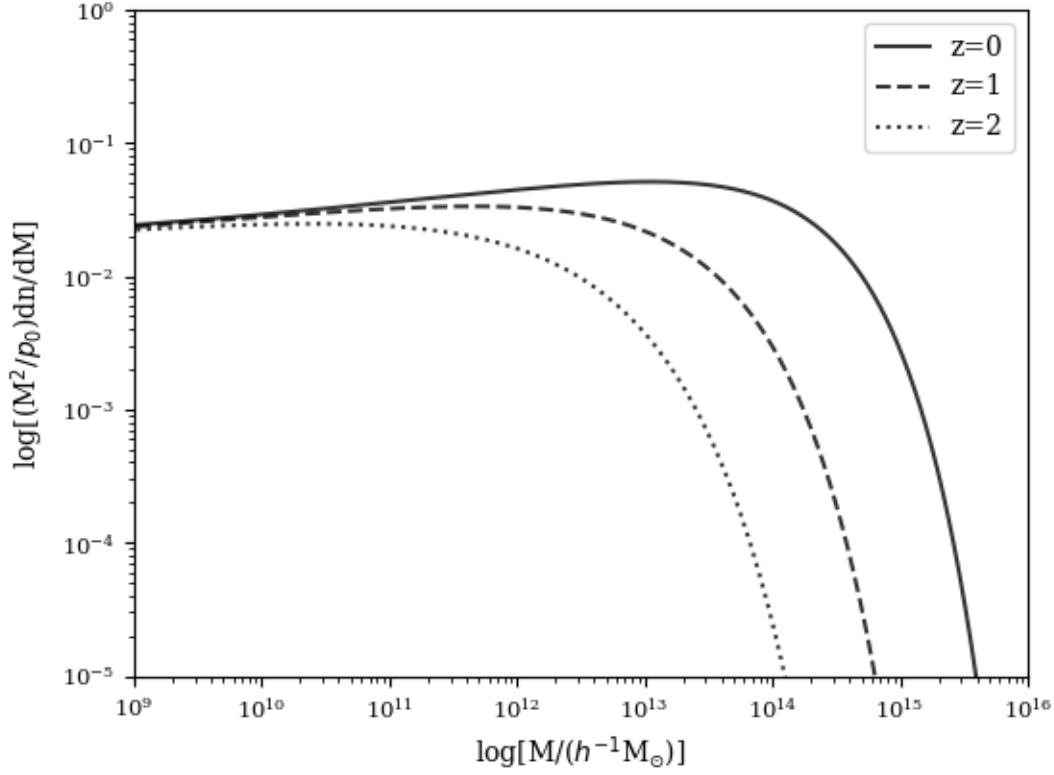
Figure 3.1: The figure shows the mass function derived by Tinker et al. [5] plotted as $(M^2/\rho_0)dn/dM$ vs $M/h^{-1}M_\odot$ both in log scale, with the mass of the halo taken to be M_{500c}. The three curves represent respectively the mass function at redshift $z = 0$ (solid), $z = 1$ (dashed) and $z = 2$ (dotted). All curves are approximately flat until they reach their characteristic mass threshold, after which they fall off sharply. Specifically, at higher redshifts correspond smaller mass cutoffs, as we would expect given that large scale structures form in a hierarchical matter.

with the function $f(\sigma)$ parametrized as:

$$f(\sigma) = A\left[\left(\frac{\sigma}{b}\right)^{-a} + 1\right]\exp\left[-\frac{c}{\sigma^2}\right],\tag{3.10}$$

where σ is defined as in eq.3.6 and A, a, b, and c are constants to be calibrated by simulations representing, respectively, the overall amplitude of the mass function, the slope and amplitude of the low-mass power law, and the cutoff scale at which the abundance of halos exponentially decreases [5]. The best fitted values of these parameters for our case of interest $\Delta = 500$ are:

$$[A, a, b, c] = \{0.220, 1.682, 1.868, 1.386\}.\text{[9]}$$

Figure 3.1 shows the obtained mass function at $\Delta = 500$ for 3 different values of redshift, namely $z = \{0, 1, 2\}$.

3.1.2   Exploring the theoretical cluster distribution for ΛCDM

Given the halo mass function from eq.3.9, one can now estimate the theoretical cluster distribution per redshift for the ΛCDM model [10], according to eq.3.1. There are three separate contributions to this theoretical prediction:

1. The comoving volume element $\frac{dV}{d\Omega dz}$, which is fully determined by the density parameters characteristic of the ΛCDM model.

---

[9]These values are obtained from the fitting functions for the parameters of $f(\sigma)$ in terms of $\log_{10}\Delta$ provided by Tinker et al in [5]:

$$A = 0.1(\log_{10}\Delta) - 0.05; \qquad\qquad a = 1.43 + (\log_{10}\Delta - 2.3)^{1.5}$$
$$b = 1.0 + (\log_{10}\Delta - 1.6)^{-1.5}; \qquad\qquad c = 1.2 + (\log_{10}\Delta - 2.35)^{1.6}.$$

[10]Eq.3.1 is actually valid for any cosmological model but here we only discuss the predictions for ΛCDM model, since is the only model we use as framework throughout this thesis.

2. The integral over the mass function [11], which can only be evaluated numerically and it is a very sensitive function of M_{thr} and σ_8.

3. The survey area $\Delta\Omega$, which acts as a normalization factor.

This shows that, on a purely theoretical standpoint, there are only three elements that can effect the total cluster count, namely: σ_8, M_{thr} and $\Delta\Omega_{\mathrm{eff}}$. The latter, as we just mentioned acts simply as a normalization factor. Hence, the shape of the overall distribution is fully determined by σ_8 and M_{thr}. Specifically, for larger values of σ_8, more clusters are found at higher redshift consequently shifting the peak of the distribution towards the right. On the other hand, a high and flat mass threshold has the opposite effect, shifting considerably the peak of the distribution to lower redshifts. Figure 3.2 shows these opposing actions separately: the top plot presents the cluster distribution for constant $M_{\mathrm{thr}} = 1 \cdot 10^{14} M_\odot$ and varying $\sigma_8 = \{0.7, 0.8, 0.9\}$; conversely the bottom plot presents the corresponding distribution for constant $\sigma_8 = 0.8$ and varying $M_{\mathrm{thr}} = \{1, 3, 5\} \cdot 10^{14} M_\odot$. For both cases the total survey area is taken to be $\Delta\Omega = 10$ degrees^2.

---

[11]which we take to be that derived by Tinker et al. (eq.3.9), as motivated by the discussion in Sec.3.1.1.
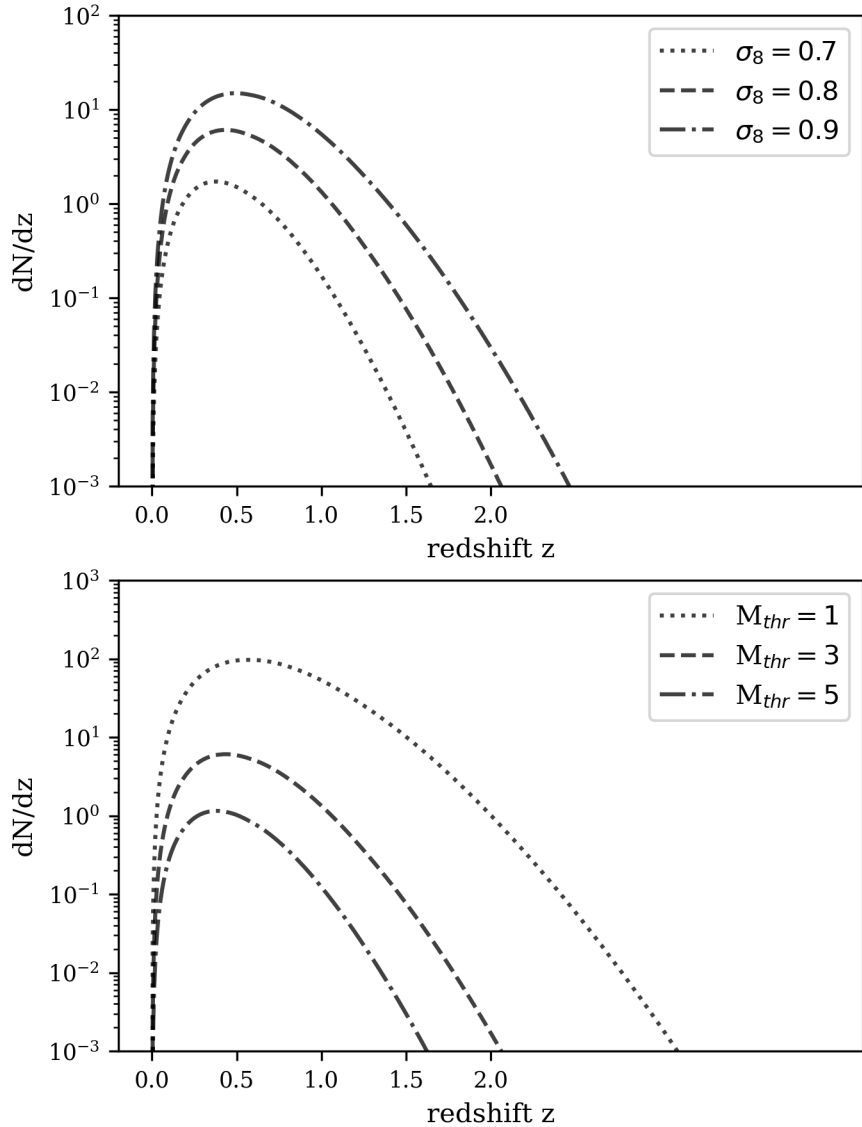
Figure 3.2: The two figures show the cluster redshift distribution given the Tinker et Al.[5] mass function, $\Delta\Omega = 10$ degrees^2 and varying σ_8 and M_{thr}. Specifically the top panel has constant $M_{\mathrm{thr}} = 1 \cdot 10^{14} M_\odot$ and varying $\sigma_8 = \{0.7, 0.8, 0.9\}$; the bottom panel has constant $\sigma_8 = 0.8$ and varying $= M_{\mathrm{thr}} = \{1, 3, 5\} \cdot 10^{14} M_\odot$. The plot emphasizes the conflicting effects of $\sigma_8 = 0.8$ and M_{thr} on both the normalization and shape of the distribution. Specifically, dN/dz shifts to the right and has a lower total cluster count for increasing σ_8 and/or decreasing M_{thr}; and it shifts to the left and has a higher total cluster count for decreasing σ_8 and/or increasing M_{thr}.

Finally, Figure 3.3 shows the theoretical estimate of the cluster distribution at different mass thresholds for a survey area equal to that of the ACT S18dn cluster catalog, namely with $\Delta\Omega = 15,170$ square degrees. Here σ_8 is taken equal to 0.8, in accordance with the mounting evidence that constrains σ_8 around this value [48, 49, 6]. Considering that the estimated mass of the lightest cluster from the ACT sample is $\sim 1 \times 10^{14} M_\odot$ [12], it is interesting to note that the purely theoretical estimate of the total number of clusters N_{tot} for masses above such threshold is roughly 3 orders of magnitude larger than the total number of detected clusters in the ACT survey.

---

[12]see Sec.3.2.1 for the details on the method used by the ACT collaboration for the cluster mass evaluation.
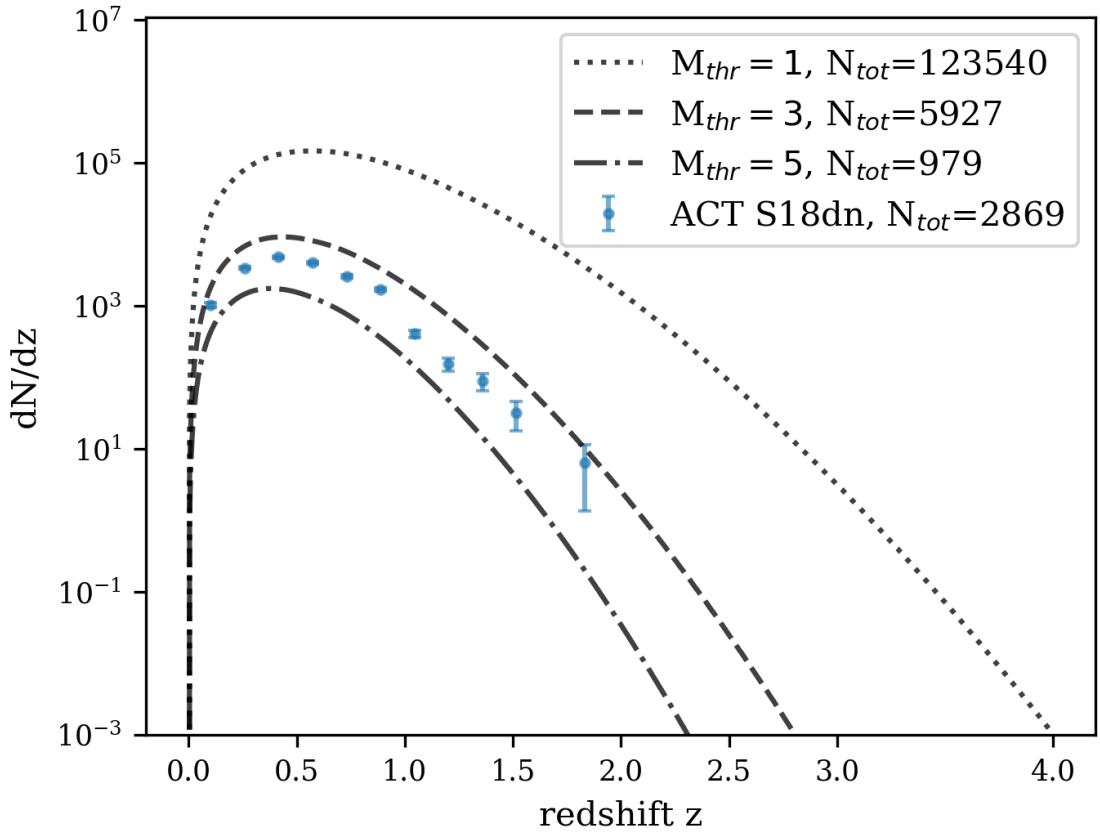
Figure 3.3: Theoretical prediction of the cluster redshift distribution given the Tinker et Al mass function, $\Delta\Omega = 15,170$ degrees^2, $\sigma_8 = 0.8$ and three different mass thresholds in units of $10^{14} M_\odot$: $M_{\mathrm{thr}} = 1$ (dotted), $M_{\mathrm{thr}} = 3$ (dashed) and $M_{\mathrm{thr}} = 5$ (dot-dashed). For comparison, it's plotted the corresponding dN/dz distribution from the ACT S18dn cluster sample (see Sec.3.2 for more details in this computation). The total number of clusters above each threshold N_{tot} is defined as the are under the curve. For $M_{\mathrm{thr}} = 1$, which corresponds approximately to the estimated mass of the lightest cluster in the ACT sample, $N_{\mathrm{tot}} \sim 10^6$, roughly 3 orders of magnitude more than the total number of clusters observed by ACT.

3.2 $\frac{dN}{dz}$ cluster distribution from the ACT S18dn survey

The huge difference evidenced in the previous section, between the total number of clusters predicted by the theory and what we actually observe, relates to the observational effects of cluster detection. These effects include intrinsic astrophysical properties of clusters and the selection function associated with the cluster finder algorithms. Hence, in order to use the galaxy clusters count distribution derived from an experiment for cosmological purposes, one needs to characterize these effects very accurately. The mean to accomplish such characterization is, as we mentioned in the opening paragraph of this chapter, a comprehensive likelihood analysis such as the one described in [6, 49, 38].

Here, to simplify this analysis, we take the ACT mass estimate method, which we present in Sec.3.2.1, to be true and we consider the main effects of the selection function (see Sec.3.2.2) to be fully encoded in the value of the mass threshold M_{thr} and effective survey area $\Delta\Omega_{eff}$.

3.2.1 Cluster mass estimate

As thoroughly described in [6], for the purposes of using the SZ signal to estimate cluster masses, the ACT collaboration developed a framework in which they consider: (1) the cluster profile to be well described by the UPP (see Sec.2.2.3), up to some overall adjustments to the normalization and mass dependence; (2) the SZ signal to be parametrized by a single statistic, obtained from the ACT map filtered using $\Psi_{5'.9}(k)$ and (3) the relativistic SZ-corrections to be negligible. This approach allows

them to compute the "uncorrected"[13] Compton y-parameter $\tilde{y}_0$ as:

$$\tilde{y}_0 = 10^{A_0} E(z)^2 m^{1+B_0} Q\left(\theta_{500c}/m^{C_0}\right) f_{\rm rel}(m,z),\qquad(3.12)$$

where $\left[10^{A_0}, B_0, C_0\right] = \{4.950 \times 10^{-5} h_{70}^{\frac{1}{2}}, 0.08, -0.025\}$; $f_{\rm rel}(m,z) = 1 + 3.79t - 28.2t^2$ includes the relativistic effects for the gas temperature T_e[14]; $m = M_{500c}/(3 \cdot 10^{14} M_\odot)$ is a convenient mass parameter and

$$Q(\theta) = \int \frac{d^2k}{(2\pi)^2} \Psi_{5.9}(k) B(k) \int d^2\theta' e^{i\theta'\cdot k} \tau\left(\theta'/\theta\right)\text{[15]}\qquad(3.13)$$

is the spatial convolution of the filter, the beam, and the cluster's unit-normalized integrated pressure profile [6] (see 3.4).

The usage of a single filter clearly simplifies data processing and has the additional advantage that one does not suffer from inter-filter noise bias. Moreover, one can note from Fig.3.4 that the fixed angular scale at $\theta_{500c} = 5.9$ lies in the regime where the measured $\tilde{y}_0$ statistic for high significance clusters is approximately constant [6]. Hence, eq.3.12 relates $\tilde{y}_0$ to the mass and redshift of a cluster while accounting for the impact of the filter on clusters whose angular size is determined by their mass and redshift. That said, due to intrinsic scatter, measurement noise and the very steep cluster mass function, one cannot naively invert eq.3.12 to obtain the mass estimates. To correct such biases, a Bayesian analysis is required that accounts for the underlying distribution of flux densities and makes reasonable assumptions on the form of the posterior probabilities between the mass parameter m, the observation $\tilde{y}_0^{\rm ob}$ and the true SZ signal $\tilde{y}_0^{\rm tr}$ in the absence of noise [6]. In this work, we

---

[13]Uncorrected in the sense that it is associated with the fixed angular scale filter and does not include a relativistic correction [6].

[14]Here $t = -0.000848 \times (mE(z))^{-0.585}$ according to the scaling relation provided in [50].

[15]Here $B(k)$ and $\tau\left(\theta'/\theta\right)$ are respectively the product of the beam response with the map pixel window function and the signal template at angular scale θ' [6].
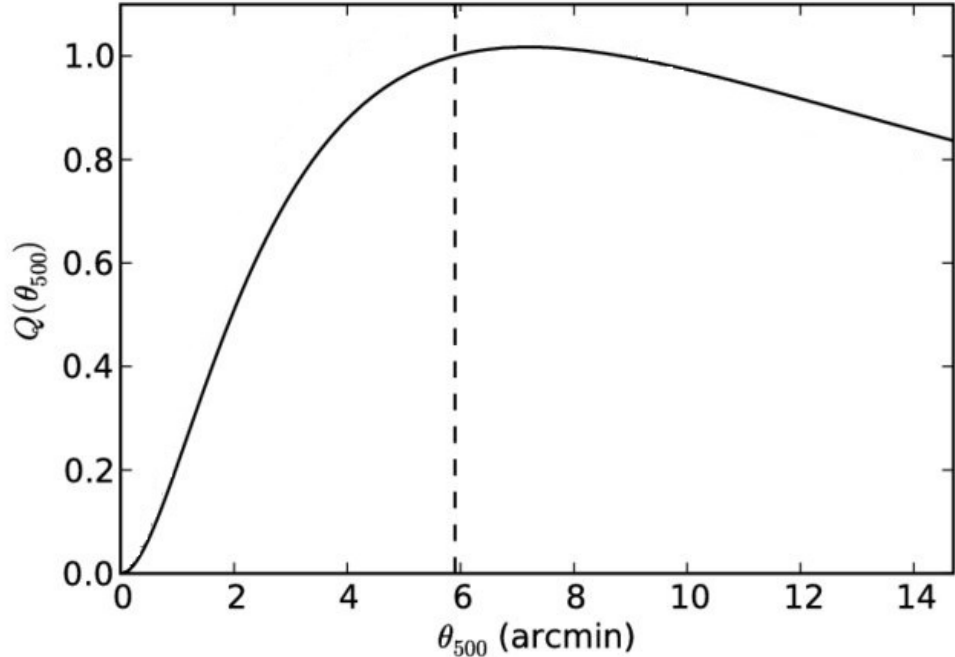
Figure 3.4: The plot shows the response function used to reconstruct the cluster central decrement as a function of cluster angular size. At $\theta_{500c} = 5'.9$, the filter is perfectly matched and $Q = 1$. At scales slightly above $5'.9$, $Q > 1$ because such profiles have high in-band signal despite being an imperfect match to the template profile [6].

simply use the mass estimates of the ACT S18dn cluster sample obtained from this analysis, previously performed by other members of the ACT collaboration. Figure 3.5 shows the M_{500c} estimates of the $2,869$ clusters in the sample as a function of redshift z, and their respective distributions.

3.2.2 Purity and Completeness of the Survey

The selection function associated with the cluster finder algorithm and survey strategy can be mainly characterized by two parameters: its completeness and its purity. The completeness of a cluster catalog is defined as the fraction of galaxy clusters correctly identified relative to the number of true dark matter halos. On the other hand, the purity of the same catalog is defined as the fraction of galaxy clusters correctly identified relative to the total number of detected clusters [51]. Hence, a low
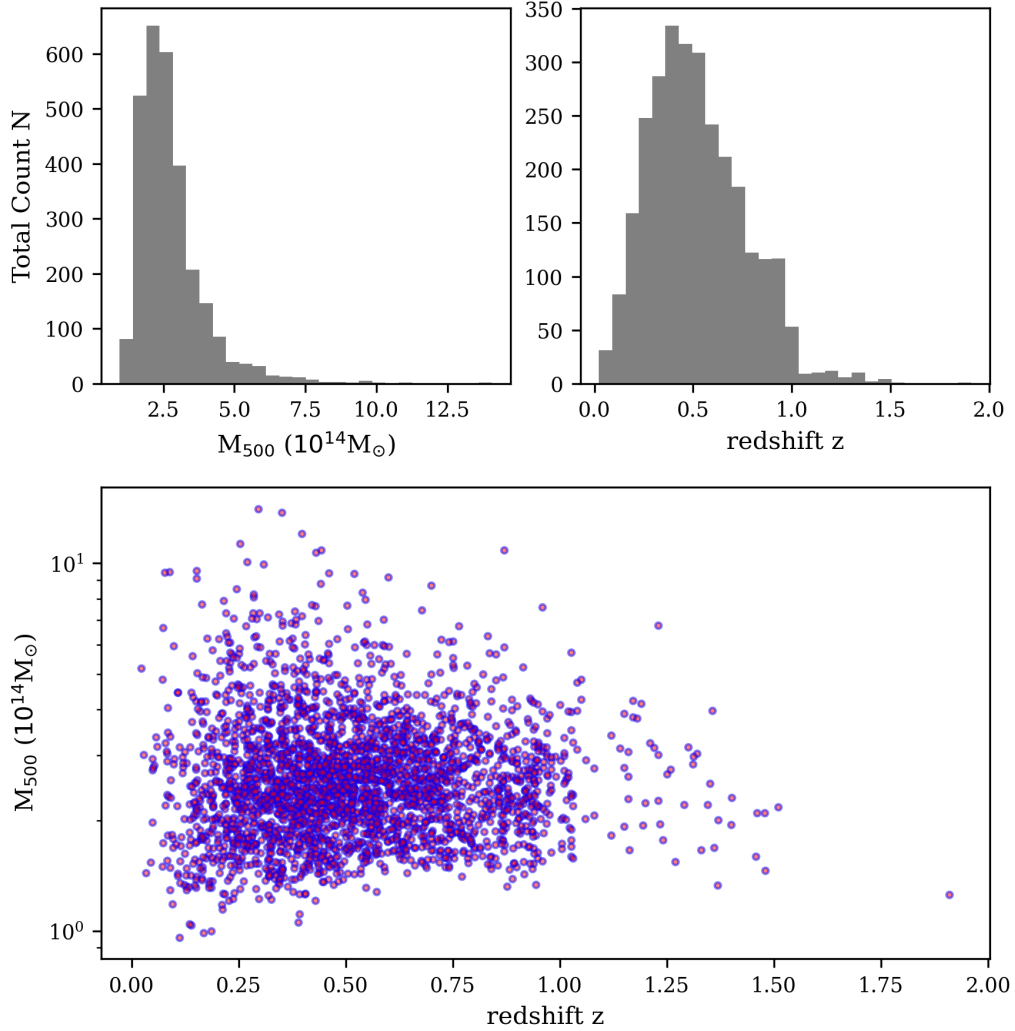
Figure 3.5: The plot shows the mass (top left) and redshift (top right) distribution of the 2879 clusters in ACT S18dn cluster catalog. The bottom plot simply maps all the observed clusters in terms of their mass (in log scale) and redshift. The median redshift and mass are respectively 0.49 and $2.49 \cdot 10^{14} M_\odot$. The lack of clusters at low redshift ($z < 0.2$) is largely a selection effect, due to the angular size of such clusters being similar to the CMB anisotropies [7].

completeness indicates an inefficiency of the cluster finder in detecting systems that it should have detected, whereas a low purity indicates a high fraction of false positives in the sample [51]. It is clear then how the combination of these two factors can strongly diminish the reliability of a survey cluster detection, if they are not properly characterized. Completeness and purity rates can be expressed as a function of mass

and redshift. Here, we parameterize them in terms of a flat 90% completeness mass threshold M_{thr}[16] and an overall normalization factor encoded in the effective survey area $\Delta\Omega_{\mathrm{eff}}$.

3.2.3   Least-squares Analysis

The computation of the cluster distribution $\frac{dN}{dz}$ for the ACT S18dn sample consists of determining a reasonable redshift bin size dz, counting the number of observed clusters N in each bin and dividing this number by dz. The standard deviation σ_i in each bin is then estimated as the square root of N divided by dz.

$$O_i = \frac{N}{dz}; \quad \sigma_i = \frac{\sqrt{N}}{dz}. \tag{3.14}$$

Given the mass estimates, computed according to the method presented in Sec.3.2.1, one can extract the cluster distribution above a specific mass threshold M_{thr} by simply excluding all such clusters with $M_{500c} < M_{\mathrm{thr}}$ from our count per bin. In Fig.3.6, we show the ACT S18dn cluster sample distribution respectively for $M_{\mathrm{thr}} = [1; 2; 3; 4] \cdot 10^{14} M_{\odot}$[17] and a total number of bins $\mathcal{N} = 12$.

To compare the observed results with the ΛCDM model theoretical predictions and estimate the value of σ_8, we perform a least squares optimization between the binned data and the theoretical function from eq.3.1 evaluated on the same $\mathcal{N}$ redshift bins with free parameters σ_8, M_{thr} and $\Delta\Omega_{\mathrm{eff}}$. It is useful to emphasize the importance of keeping these last two parameters free in order to reasonably model the selection function effects and limit their ability to significantly bias the estimated value of σ_8.

---

[16]The mass above which the ACT S18dn cluster sample is 90% complete which in this case we consider to be flat, hence redshift independent.

[17]Note that the first mass threshold in the brackets does not exclude any of the clusters detected by ACT, as the observed cluster with lowest mass has $M_{500c} \approx 0.96 \cdot 10^{14} M_{\odot}$.
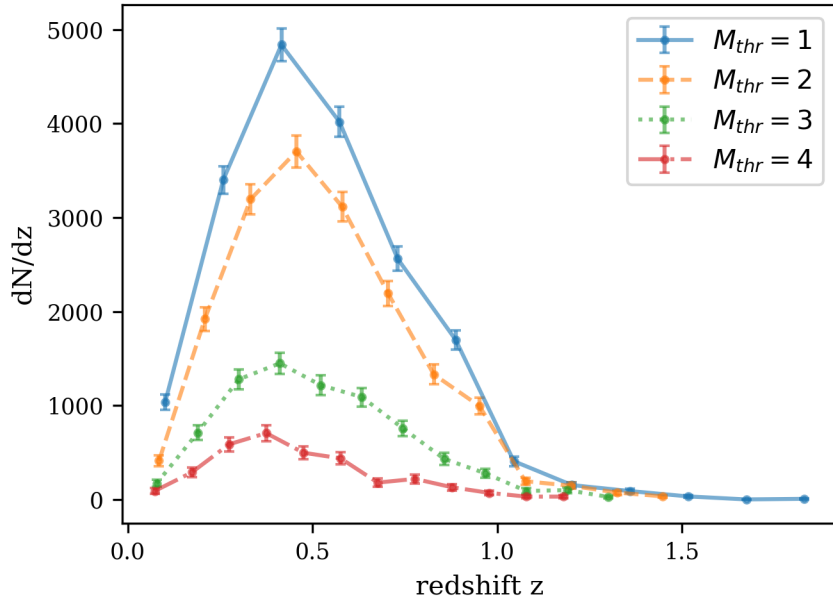
Figure 3.6: The figure shows the redshift distribution of the observed clusters from the ACT S18dn sample for increasing mass thresholds. The values of M_{thr} reported in the legend are given in units of $10^{14} M_\odot$. The data points and associated error bars for each of the $\mathcal{N} = 12$ redshift bins are given by eq.3.14.

The fitting method of least squares used in this analysis consists of minimizing the sum of the squares of the differences between the observed values O_i and the expected values E_i from the model under consideration, in each of the $\mathcal{N}$ bins. This method is based on the statistics of the Chi-square function χ^2, defined as:

$$\chi^2 = \sum_{i=1}^{\mathcal{N}} \frac{(O_i - E_i)^2}{\sigma_i^2}, \tag{3.15}$$

where σ_i^2 is the variance on the observations (see eq.3.14). A good fitted model is one where the measured values on average deviate from the ones expected from the model by their standard deviation σ_i, resulting in $\chi^2 \approx \mathcal{N}$. To be more precise, the χ^2 statistics is directly determined by the number of degree of freedom ν, defined as the difference between the number of observations $\mathcal{N}$ minus the number of fitted parameters $\mathcal{M}$: $\nu = \mathcal{N} - \mathcal{M}$. The χ^2 distribution is skewed to the right with mean

value $\mu = \nu$ and standard deviation $\sigma_{\chi^2} = \sqrt{2\nu}$. Customarily in place of χ^2, the so-called "reduced" χ^2_ν is used, simply defined as:

$$\chi^2_\nu = \frac{\chi^2}{\nu}, \tag{3.16}$$

which basically consists of a normalized χ^2, such that for a good fitted model one would expect $\chi^2_\nu \approx 1$.

The results of this analysis are reported in the table below. The two models presented correspond, respectively, to the best fit considering the whole 3 dimensional parameter space (f_1^{bf}) and to the best fit for fixed $\sigma_8 = 0.8$ (f_2^{bf}). It is important to note that since M_{thr} is regarded as the flat 90% completeness mass threshold, the data are compared to the 90% of the total cluster count predicted by the theoretical model under consideration.

f_1^{bf} is characterized by a considerably lower estimate of σ_8, in contrast with the mounting evidence which constrains $\sigma_8 \gtrsim 0.8$. This peculiarity seems to be non-physical and strictly related to the assumption of taking the mass threshold to be constant in redshift, a feature which can strongly affect the shape of the $\frac{dN}{dz}$ in such a way as to effectively bias the computation of σ_8. Indeed, as shown in Fig.3.2, when keeping everything else constant and up to a normalization factor, σ_8 and M_{thr} have competing roles in effecting the shape of the $\frac{dN}{dz}$, which can cancel out for different combinations of σ_8 and M_{thr}: a distribution with low σ_8 and a high and flat mass threshold, like the one characterizing f_1^{bf}, can have a similar shape of another distribution characterized by a higher value of σ_8 and a lower value of M_{thr}.

This motivates the introduction of another model f_2^{bf} which considers a more realistic estimate of σ_8. The fitted parameters for f_2^{bf} provide an effective survey area which is approximately $\frac{1}{7}$ of the total area inspected and a mass threshold which is

Fitted Model	σ_8	M_{thr} [$10^{14}M_\odot$]	$\Delta\Omega$ [degrees^2]	χ^2_ν	ν
f_1^{bf}	0.725	4.65	7792	0.8	8
f_2^{bf}	0.8	3.85	2369	1.5	9

Table 3.1: The table shows the constrained parameters for the two fitting functions found by χ^2 minimization. Specifically, $f^{\mathrm{bf_1}}$ corresponds to the best fitting function considering the whole 3 dimensional parameter space, while $f^{\mathrm{bf_2}}$ is the best fitting function with fixed $\sigma_8 = 0.8$. The last column ν identifies the number of degrees freedom defined as the difference between the number of observations and the fitted parameters. $f^{\mathrm{bf_2}}$ has 1 degree of freedom more than $f^{\mathrm{bf_1}}$ since σ_8 is held fixed, leaving only 2 free parameters instead of the 3 for $f^{\mathrm{bf_1}}$.

comparable to the survey-averaged 90% mass completeness limit at z=0.5, estimated by the ACT collaboration at $3.8 \cdot 10^{14} M_\odot$.

Though the value of χ^2_ν for f_2^{bf} is approximately twice that of f_1^{bf}, the models are statistically indistinguishable. To show this, one has to look at their corresponding χ^2 values and where they place inside the χ^2 distributions determined by the respective number of degrees of freedom of each model. Specifically, for f_1^{bf} $\chi^2_{\mathrm{bf_1}} = 13.5$ and for f_2^{bf} $\chi^2_{\mathrm{bf_2}} = 6.4$[18]. The difference between the two values $\Delta\chi^2 = 7.1$ is within two standard deviations of both distributions, hence we cannot claim to have any statistically significant difference between the fitted models. This rather humdrum result is a direct consequence of all the assumptions made in this analysis, specifically in regards to the cluster survey selection function. We cannot treat this χ^2 minimization method as a mean to constrain any parameter in a statistically meaningful way since it lacks a rigorous likelihood analysis which takes into account all the factors that can impact the galaxy cluster statistics of the observed sky for a given survey. Instead, one should look at this analysis just as a way to illustrate that the observed data reconcile with the cosmological prediction suggested in the literature of $\sigma_8 \approx 0.8$ for reasonable estimates of a flat 90% completeness mass threshold M_{thr} and effective survey area $\Delta\Omega_{\mathrm{eff}}$.

---

[18]Here the subscript bf_i indicates the respective model for $i \in \{1, 2\}$.
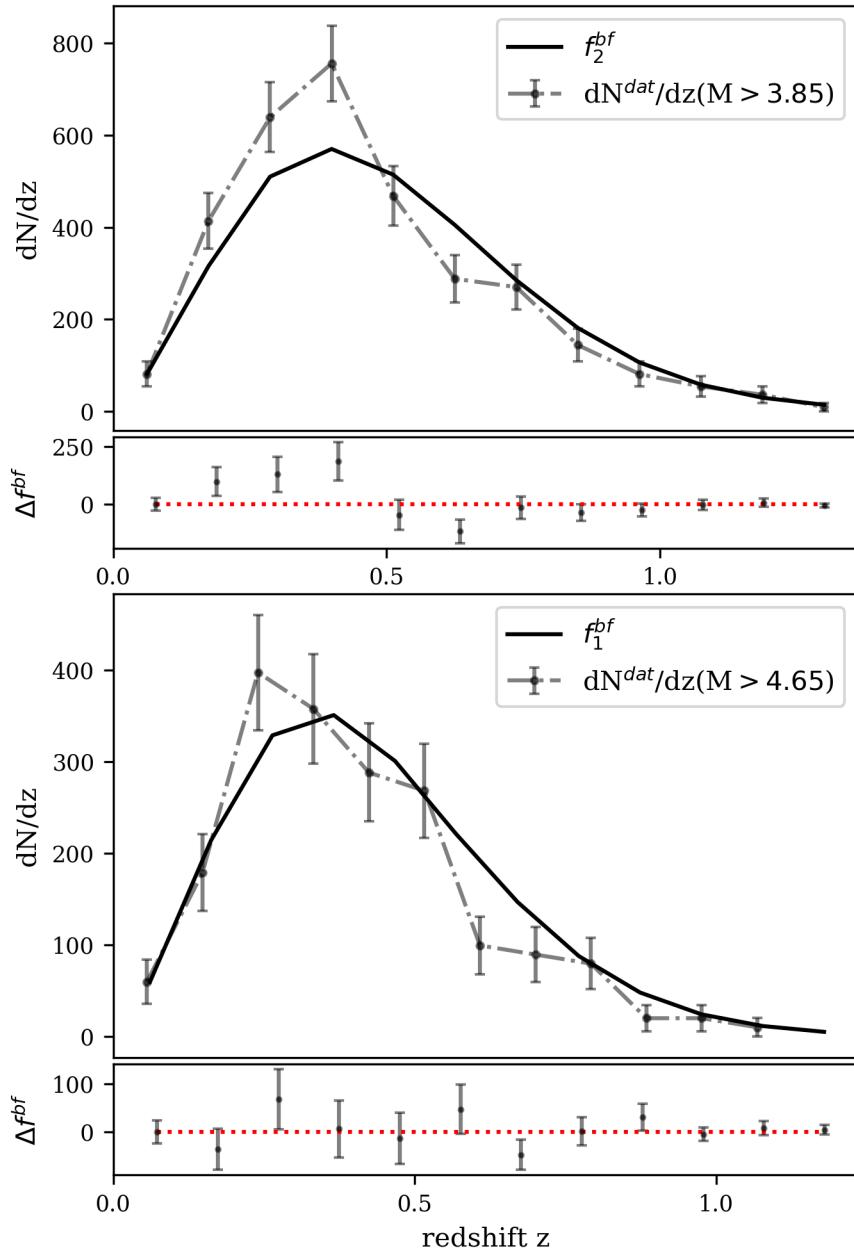
Figure 3.7: The plots in the figure show a comparison between the redshift cluster distributions of the raw data (dot-dashed line) and the two fitted models (solid-lines): f_1^{bf} (bottom) and f_2^{bf} (top). For each plot, we also show the residuals (Δf^{bf}) of the measured cluster counts with respect to the two fitted models. The dotted red line here represents the 0 value, hence no difference between the measured and fitted values.

Chapter 4

Raw Maps Stacking Analysis

In this chapter, we analyze the raw maps[1] of the $2,869$ clusters from the ACT S18dn sample, averaging them over 5 specific mass and redshift ranges. The essence of this stacking process is to investigate clusters' properties and their dependence on redshift and mass. The mass ranges are all equally spaced with width $w = \frac{1}{5} \times (M_{\max} - M_{\min}) = 2.6 \times 10^{14} M_{\odot}$, where $M_{\max}$ and $M_{\min}$ represent respectively the highest and lowest estimated mass for a cluster in the sample[2]. On the other hand, the redshift ranges are determined by imposing the same number of clusters N_c in each of them.

This differentiation in the definition of the redshift stacking from the mass stacking is made to ensure a proper statistics in the computation of the weighted average cluster. In fact, when one considers only equally spaced bins for both the mass and redshift, one finds that in both cases the highest bin contains only a few clusters. Nevertheless, for the mass stacking case this does not cause an issue since, given the approximately linear relationship between M_{500c} and y, these clusters present very deep potential wells that are easily discernible from the overall CMB noise, even if the map is unfiltered. Instead, for the redshift stacking case, since the Compton

---

[1]By raw map it's intended the unfiltered original map which still includes bright sources.

[2]Note, here the masses are taken as estimated by the process illustrated in Sec.3.2.1.

y-parameter is theoretically independent of redshift, the only factor that plays a significant role in the z-distribution is the hierarchical pattern of structure formation, by which we expect clusters at high redshift to be generally smaller in size than those at lower values of z. Hence, in this scenario, for a high redshift bin, one would have to compute an average over a small number of very faint clusters which would not produce a clear result, particularly taking into account that the map is unfiltered. Provided these two sets of redshift and mass ranges, we extracted square patches of side 30×30 arcmins centered on each cluster position from the all-sky ACT equatorial map (Fig.1.3); and then stacked them together based on their redshift and mass [3].

The computation of the average cluster per mass and redshift bin is based on an inverse-variance weighting, where each pixel value $p_j = \Delta T_j$ in the map has an associated weight w_j given by the inverse of the variance:

$$w_j = \frac{1}{\sigma_j{}^2}. \tag{4.1}$$

Hence, the jth pixel of the averaged cluster on a specific mass or redshift bin has associated value and weight given by:

$$\Delta T_{j,\mathrm{avg}} = \frac{\sum_{i=1} \Delta T_{j,i} \cdot w_{j,i}}{\sum_{i=1} w_{j,i}}; \qquad w_{j,\mathrm{avg}} = \sum_{i=1} w_{j,i}. \tag{4.2}$$

If on one hand $\Delta T_{j,\mathrm{avg}}$ is simply the result of a weighted average, $w_{j,\mathrm{avg}}$ is given by the sum of the single weights from all the clusters maps, strongly reducing the uncertainty σ_j on each pixel value.

---

[3]The extracted square patches correspond to images of 60×60 pixels, as the resolution of the ACT map is 0.5 arcminutes. Note that here we are making the implicit assumption that all the pixels have the same size. This is not true since, for points off the celestial equator, one has to correct for the real distance in R.A. which shrinks by a factor of $\cos(\mathrm{Dec})$. That said, given the central area of the ACT survey and the small size of the square patches, the magnitude of these corrections is rather small and we can thus neglect it for simplicity, without effecting significantly our results.

Figures 4.1 and 4.2 show the result of this process respectively for the mass and redshift stacking of the clusters extracted from the ACT temperature map at both 90 and 150 GHz.
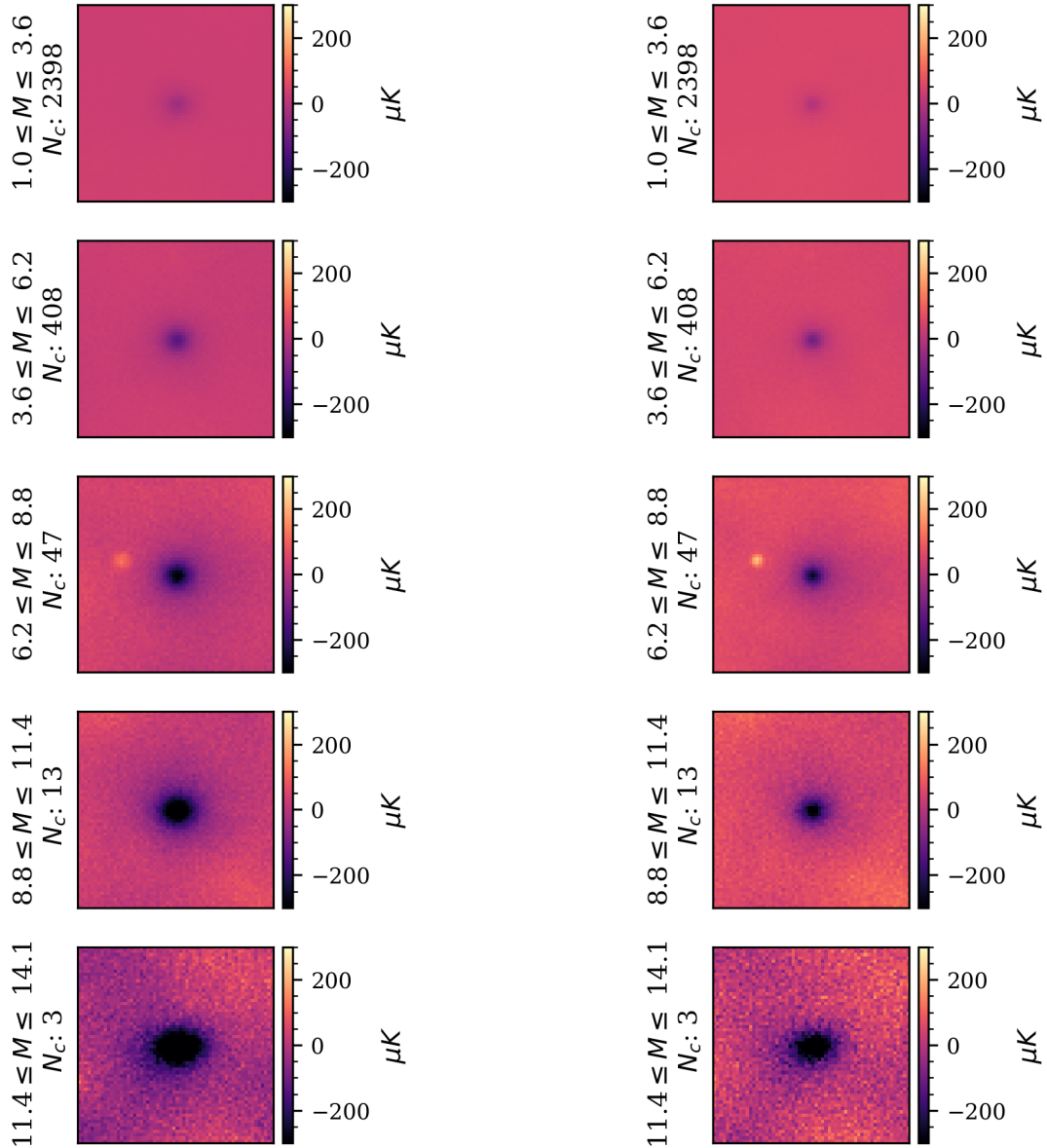
Figure 4.1: The images present the average clusters from the ACT dS18 dataset for 5 different mass ranges of width $w = \frac{1}{5} \times (M_{\mathrm{max}} - M_{\mathrm{min}}) = 2.622 \times 10^{14} M_{\odot}$. N_c represents the number of clusters on which the weighted average is computed in each mass range. On the left, the frequency under consideration is 90 GHz; on the right, 150 GHz.
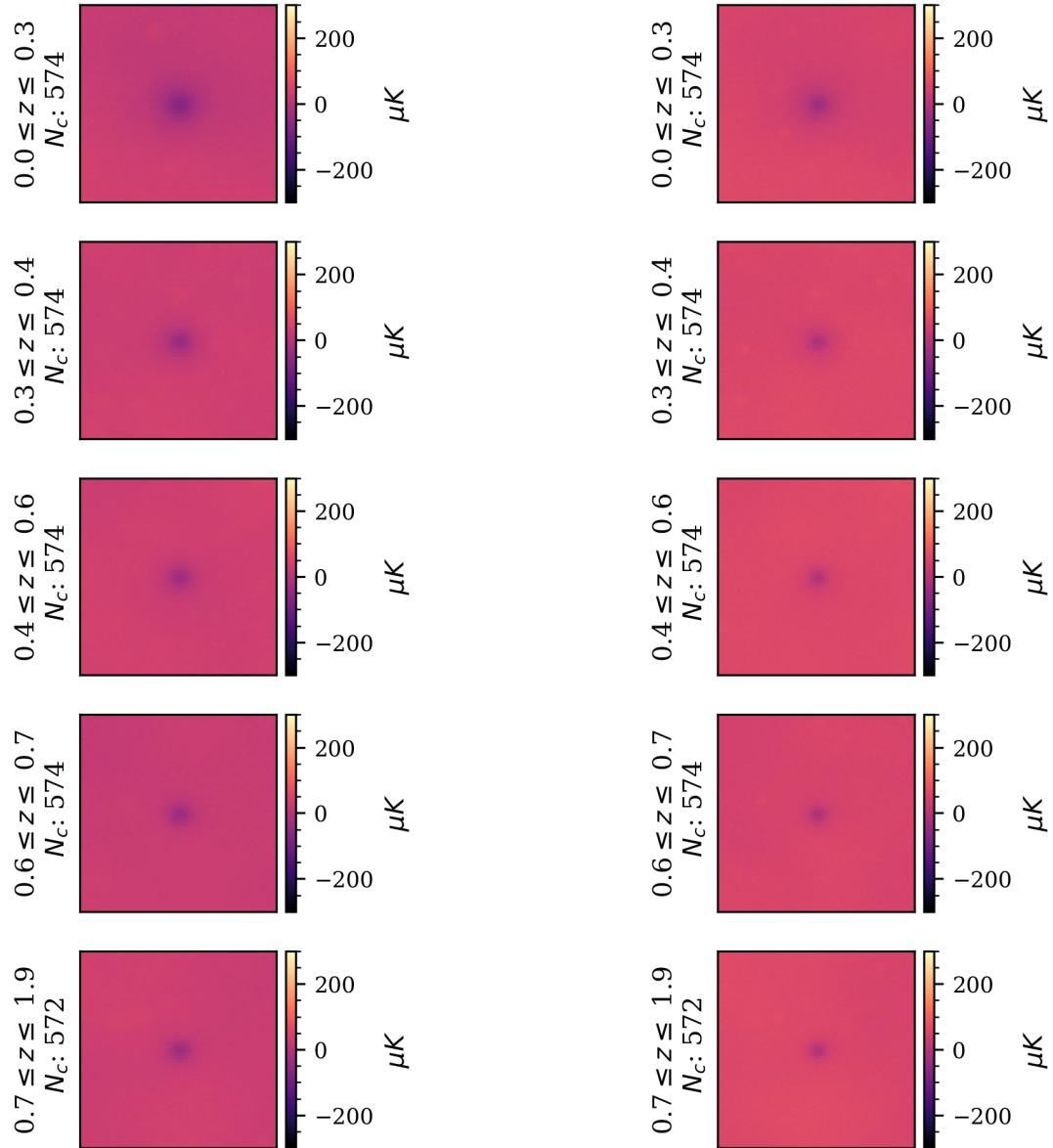
Figure 4.2: The images present the average clusters from the ACT dS18 dataset for 5 different redshift ranges determined by imposing the same number of clusters N_c in each of them. Specifically $N_c = 574$ for each range, apart from the last one which has $N_c = 572$. On the left, the frequency under consideration is 90 GHz; on the right, 150 GHz.

4.1 Testing Pressure Profiles

As thoroughly described in Chapter 3, we know that cosmological constraints derived from galaxy cluster samples are generally limited by the accuracy of cluster selection and mass-observable scaling relations. In particular, further progress in this area requires that we develop an improved understanding of cluster pressure profiles, including their dependence on the cluster mass, redshift and the expected form of the scaling relations in terms of the choice of integration radius. The ACT S18dn cluster catalog provides a great opportunity for this kind of investigation given the increase of approximately one order of magnitude in the number of confirmed clusters compared to previous datasets. In this section, we examine the two major pressure profiles presented in Sec.2.2: (1) the Isothermal β model and (2) the Universal Pressure Profile. The analysis consists in fitting such models using χ^2-minimization (as described in Sec.3.2.2) to the radial profiles of the average clusters calculated from both the mass and redshift stacking procedure. It is important to emphasize that the errors obtained on the best fitted parameters for each of the models under consideration are purely statistical and a product of the χ^2_ν minimization algorithm. Hence, we simply report them as a measure to probe the model and we do not ascribe any physical significance to them.

To obtain these radial profiles, the inverse-variance weighted averaging process described earlier is repeated. The central decrements $\Delta T(\theta)$ and their respective uncertainties $\sigma_{\Delta T}$ are computed according to eq.4.2, where in this case the sum is performed over all the pixels at dimensionless distance θ from the center, for θ that goes from 0.5 to 15 arcmins in steps of 0.5 arcmins. Every profile is offset by the average of the 5 most distant radial bins such that for large θ, $\Delta T \to 0$ regardless of the mass or redshift range under consideration. This offsetting significantly suppresses the effect of the constant background noise from the surrounding region of the cluster and allows an easier comparison between cluster profiles at different mass

and redshift range. Finally, the sign of the thermal decrements is inverted to make $\Delta T(\theta)$ positive and allow for a study of the cluster profiles in logarithmic scale and investigate the multiplicative factors at each angular scale.

According to inverse-variance weighting statistics we know the error at each radial bin θ is given by:

$$\sigma(\theta) = \sqrt{1/w(\theta)} = \sqrt{1/\sum_i w_i(\theta)}, \tag{4.3}$$

where $w_i(\theta)$ corresponds to the weight at pixel i for all is at radial distance θ. Since for larger radii θ we are averaging over a greater number of pixels then, as evidenced by eq.4.3, $\sigma(\theta)$ is expected to initially decrease sharply as θ increases and then flatten out at large radii. This effect is shown in Fig.C.1 for the average clusters radial profile at 150 GHz stacked by redshift and it represents a very useful tool to verify that one has done the right computation during the averaging procedure.

4.1.1   Beam Convolution

Though the ACT maps under consideration are unfiltered, one still needs to take into account the bias introduced by the telescope point spread function, which acts as a low-pass spatial filter on the astrophysical signal from the sky [9]. This can be accomplished by convolving the theoretical models with the beam profile and prior to their comparison with the data from the maps:

$$\mathcal{F}(\theta) = (\mathcal{B} * F)(\theta) \equiv \int_0^\theta F(\tau)\mathcal{B}(\theta - \tau)d\tau, \tag{4.4}$$

where $\mathcal{B}(\theta)$, $F(\theta)$ and $\mathcal{F}(\theta)$ are, respectively, the beam profile and the theoretical model before and after the convolution, with the latter representing the function that is ultimately compared to the data from the maps.

The profile of the beam can be modelled as a Gaussian filter of width equal to the beam size which, as reported in Sec.1.3, is 2.1' and 1.4' respectively at 90 and 150
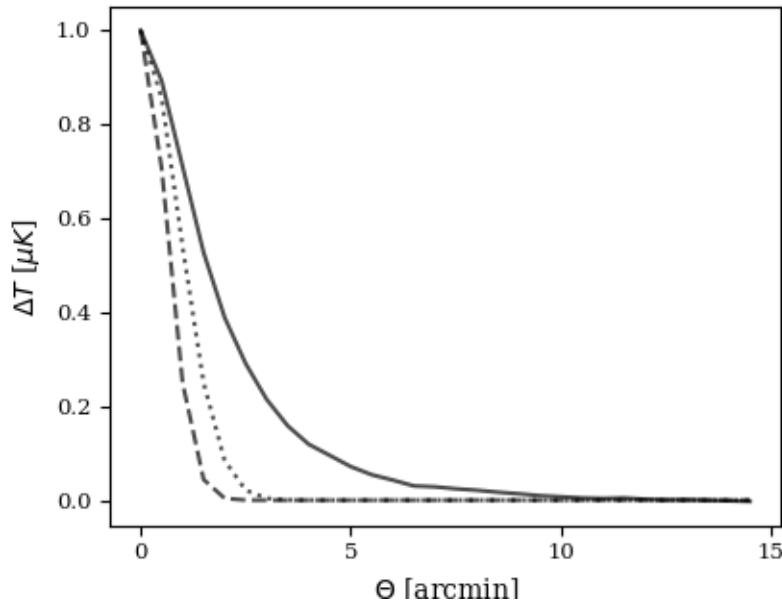
Figure 4.3: The figure presents the ACT 150 GHz (dashed) and 90 GHz (dotted) Gaussian beam characterized respectively by FWHM of 0.6 and 0.9 arcminutes. Shown for reference, the normalized radial profile of the total average cluster from the whole sample (solid).

GHz. To grasp a more graphic intuition on the relevance of the effects of the beam on the measured signal, Figure 4.3 shows the radial profiles of the point spread function at both 90 and 150 GHz in comparison with the normalized absolute average cluster profile[4].

4.1.2   The Isothermal β model

Given the linear relationship between the thermal decrements and the Compton y-parameter as conveyed in eq.2.1, we can consider the Isothermal β profile for $\Delta T(\theta)$ to take on the same form as $y(\theta)$, up to a normalization factor. Hence, the fitting

---

[4]by absolute average cluster profile, we mean the profile obtained by averaging over every cluster in the sample, regardless of its mass or redshift.

function is expressed in its general form as:

$$\Delta T(\theta) = \delta T_{0,\beta} \Big[1 + \Big(\frac{\theta}{\theta_c}\Big)^2\Big]^{\frac{1}{2} - \frac{3\beta}{2}} + c_{0,\beta}, \qquad (4.5)$$

with $\delta T_{0,\beta}$, θ_c, β and $c_{0,\beta}$ taken here as free parameters. $c_{0,\beta}$ is an additional constant required to effectively discern any left over background noise level from the estimate of the cluster profile peak and shape. $\delta T_{0,\beta}$ and θ_c represent, respectively, the normalization factor and angular core radius, features which we expect to be unique to the stacked group under consideration, specifically with higher values for clusters in the higher mass range and lower redshift range. Conversely β, defined as the ratio of the energy per unit mass in galaxies ($\mu_e \sigma^2$) to the energy per unit mass in gas ($k_B T_e$), is generally taken as universal factor, approximately constant among clusters. Its estimated average value has a large scatter, as low as 0.65 [52] to ~ 1.3 [53], depending also on the nature of the observation between X-ray and SZE surveys [54, 55].

In a preliminary analysis, we left β as a free parameter as done in previous literature. As evidenced by the results in Table C.1, this leads to a large scatter in the estimated value of β between stacking groups to which we cannot assign any physical significance. Perhaps one may postulate that β has some sort of dependence on the mass and/or redshift but the scatter still should not be so large nor oscillatory [5]. Following these considerations, in the final analysis we held β fixed to the value estimated for the total average cluster by the preliminary study, hence $\beta = 0.9$ at both 90 GHz and 150 GHz.

The results of this study are presented in Table 4.1 and shown visually in Figures 4.4 and 4.5, for both the mass and redshift stacking at 90 and 150 GHz. The

---

[5]For instance the maximum difference between two estimated values of β is $\Delta\beta_{\max} = 1.3$ between the cluster profile with $0.6 \leq z \leq 0.7$ and that with $0.0 \leq z \leq 0.3$. The value of 1.3 is in itself the upper bound on β obtained by the literature [53] which shows the inconsistency of this prediction.

figures are separated in 3 rows, each of which includes a different metrics of comparison between the obtained fits (solid lines in the figures) and the data (filled circles with respective error bars). Specifically, the top-row contains a standard linear scale comparison to provide a visual representation of the profiles shapes. Instead, the mid-row contains a log scale comparison between the fits and the data both normalized to 1 at their peaks. The combination of these two elements allows to discern and visibly appreciate the multiplicative factors differences both in terms of the angular radial distance θ and among the different profiles. Finally, the bottom-row contains a comparison of the residuals ($\Delta T^{\mathrm{dat}} - \Delta T^{\mathrm{pred}}$), calculated as the difference between the data and the best fits at each θ bin, for all the average clusters groups under consideration. In the bottom-row, there is also an additional flat dotted red line at $\Delta T = 0$, which helps to visually discern which data-points were underestimated or overestimated by the fitted model. As a useful note to the reader, for the remainder of the paper, in every plot and table that we include, unless otherwise specified, we take $M \equiv M_{500c}$ and report its values in units of $10^{14} M_\odot$.

Overall, this model does not fit the data well. This is evident when looking at the estimated values of χ^2_ν which are both large in magnitude and highly variant between the different stacking groups. This is particularly enhanced for the averaged clusters scaled by redshift, which tend to present higher and more variant values of χ^2_ν compared to the corresponding clusters scaled by mass. A distinct feature that arises from the plots in Figures 4.4 and 4.5 is the systematic underestimation of the central peaks of the profiles. This is related to the nature of the β-model which is limited in its ability to characterize cuspy profiles, given the approximately flat behaviour at small radii ($\theta/\theta_c \lll 1$) expressed by the expansion to first order of eq.4.5.

The fact that this model is not an accurate representation of the data was not unexpected. The β-model is very simple and based on three main assumptions (isothermality, spherical symmetry and hydrostatic equilibrium) which, as we discussed in

Sec.2.2.2, can only apply in certain regimes. Hence, when one considers average profiles of a large number of clusters like we do in this work, it is reasonable to suppose that enough of them will present properties that are incompatible with the β formalism [6], and consequently alter the overall profile to make it disagree with the model predictions, at this level of accuracy.

The only exception to this trend is the average cluster profile for the highest mass bin given by $11.4 \cdot 10^{14} M_\odot \leq M_{500c} \leq 14.1 \cdot 10^{14} M_\odot$. In this case, the β-model fits the data fairly well with $\chi_\nu^2 = \{1.3, 2.1\}$, respectively, at 90 and 150 GHz, which correspond to the smallest χ_ν^2 values among all the pressure profiles tested in this work. That said, we do not ascribe any physical significance to this result which can simply be explained by the extremely reduced statistics of the highest mass bin, composed of only three clusters. In fact, according to the inverse-variance weighting formalism (eq.4.2), we know that the relative errors on each radial profile are scaled by a factor of $\sqrt{N_c}$, where N_c is the total number of stacked clusters within a specific mass or redshift range. Hence, the error bars for the highest mass bin are minimum twice as large relatively to those on any other range, strongly reducing the resulting χ_ν^2 as expressed by eq.3.15.

Finally, by comparing the results in Table 4.1 and C.1, we can observe that by fixing β, we resolve the physical properties of the angular core-radius θ_c which is expected to be positively correlated to the mass of the cluster[7] and negatively correlated to redshift according to the inverse of the angular diameter distance $D_A(z)$ as expressed in eq.2.5.

---

[6]e.g., relaxed and cool-cores clusters.

[7]The positive correlation between θ_c and the mass of the cluster M_{500c} follows from combination of (1) the positive correlation between the core radius r_c and M_{500c} as expressed by eq.2.18 and (2) the definition of θ_c expressed in terms of r_c: $\theta_c = r_c/D_A(z) \propto r_c$.

Mass Stacking	$\delta T_{0,\beta}$ [μK]	$\sigma_{\delta T_{0,\beta}}$ [μK]	θ_c [arcmin]	σ_{θ_c} [arcmin]	$c_{0,\beta}$ [μK]	$\sigma_{c_{0,\beta}}$ [μK]	χ^2_ν
Frequency 90 GHz							
$1.0 \leq M \leq 3.6$	60.1	1.0	0.9	-	-0.8	0.1	22.7
$3.6 \leq M \leq 6.2$	149.1	2.2	1.0	-	-1.9	0.2	12.9
$6.2 \leq M \leq 8.8$	289.5	6.1	1.5	0.1	-6.3	0.8	14.2
$8.8 \leq M \leq 11.4$	417.1	8.0	1.8	0.1	-11.2	1.3	14.6
$11.4 \leq M \leq 14.1$	626.1	6.3	1.7	-	-18.5	1.0	1.3
Tot. Avg.	70.9	1.0	1.0	-	-1.0	0.1	30.5
Frequency 150 GHz							
$1.0 \leq M \leq 3.6$	54.6	1.5	0.7	-	-0.6	0.1	42.2
$3.6 \leq M \leq 6.2$	133.9	2.3	0.9	-	-1.5	0.2	13.0
$6.2 \leq M \leq 8.8$	250.0	7.8	1.5	0.1	-5.4	0.9	33.3
$8.8 \leq M \leq 11.4$	331.3	8.6	1.7	0.1	-7.1	1.2	16.1
$11.4 \leq M \leq 14.1$	519.6	7.9	1.7	-	-15.8	1.1	2.1
Tot. Avg.	63.4	1.4	0.8	-	-0.7	0.1	47.7

Redshift Stacking	$\delta T_{0,\beta}$ [μK]	$\sigma_{\delta T_{0,\beta}}$ [μK]	θ_c [arcmin]	σ_{θ_c} [arcmin]	$c_{0,\beta}$ [μK]	$\sigma_{c_{0,\beta}}$ [μK]	χ^2_ν
Frequency 90 GHz							
$0.0 \leq z \leq 0.3$	90.1	1.4	1.8	-	-2.9	0.2	20.8
$0.3 \leq z \leq 0.4$	73.3	1.7	1.0	-	-1.4	0.2	19.4
$0.4 \leq z \leq 0.6$	65.5	1.1	0.9	-	-0.6	0.1	7.5
$0.6 \leq z \leq 0.7$	73.2	3.2	0.5	-	-0.5	0.1	12.5
$0.7 \leq z \leq 1.9$	77.1	4.2	0.5	-	-0.6	0.1	14.6
Tot. Avg.	70.9	1.0	1.0	-	-1.0	0.1	30.5
Frequency 150 GHz							
$0.0 \leq z \leq 0.3$	72.7	1.7	1.8	0.1	-2.0	0.2	38.2
$0.3 \leq z \leq 0.4$	64.6	2.4	0.9	-	-1.1	0.2	34.1
$0.4 \leq z \leq 0.6$	60.7	1.3	0.7	-	-0.5	0.1	6.9
$0.6 \leq z \leq 0.7$	76.7	9.0	0.4	0.1	-0.7	0.2	52.4
$0.7 \leq z \leq 1.9$	79.7	7.3	0.4	-	-0.7	0.1	28.1
Tot. Avg.	63.4	1.4	0.8	-	-0.7	0.1	47.7

Table 4.1: The two tables contain a report of the best fits of the Isothermal β model as expressed in eq.4.5, to the average clusters profiles stacked by mass (top) and redshift (bottom) at both 90 and 150 GHz. For each fit, the tables include the estimated values for the free parameters ($\delta T_{0,\beta}$, θ_c, $c_{0,\beta}$), their respective statistical errors ($\sigma_{\delta T_{0,\beta}}$, σ_{θ_c}, $\sigma_{c_{0,\beta}}$) and the resulting χ^2_ν. All quantities are reported with precision to 1 decimal place. As a convention, the dash – in the tables replaces the statistical errors on fitted parameters that round to 0.0 to 1 decimal place.
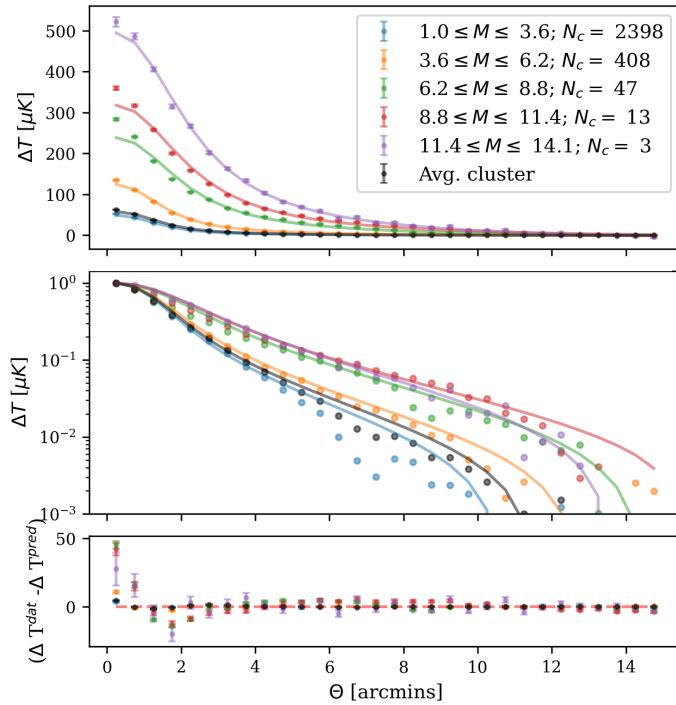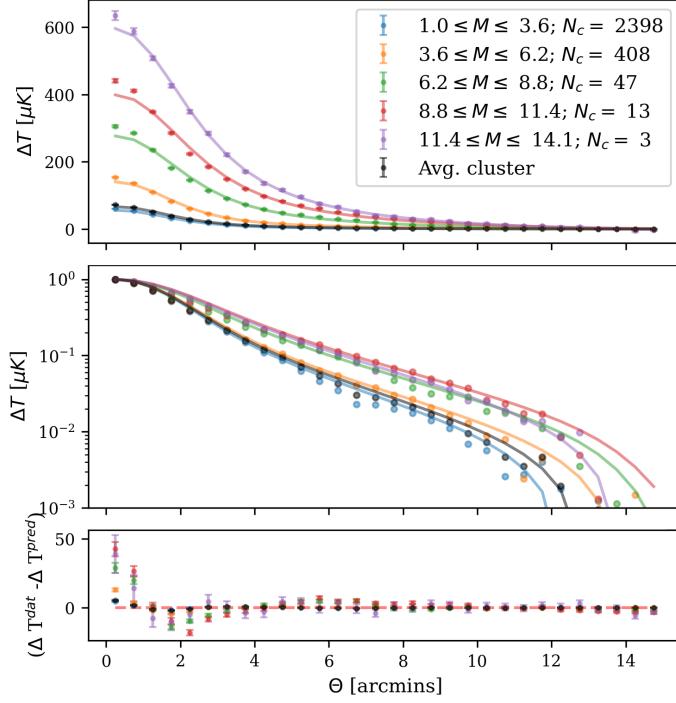
Figure 4.4: The plots in the figure show the best fits of the Isothermal β model with respect to the ΔT radial profiles of the average clusters stacked by mass at both 90 (top) and 150 (bottom) GHz. Each plot is separated in 3 rows following the convention established in Sec.4.1.2. The legend on the top right identifies each mass range and their corresponding number of clusters N_c, associating to each of them a color which is kept the same along the 3 rows.
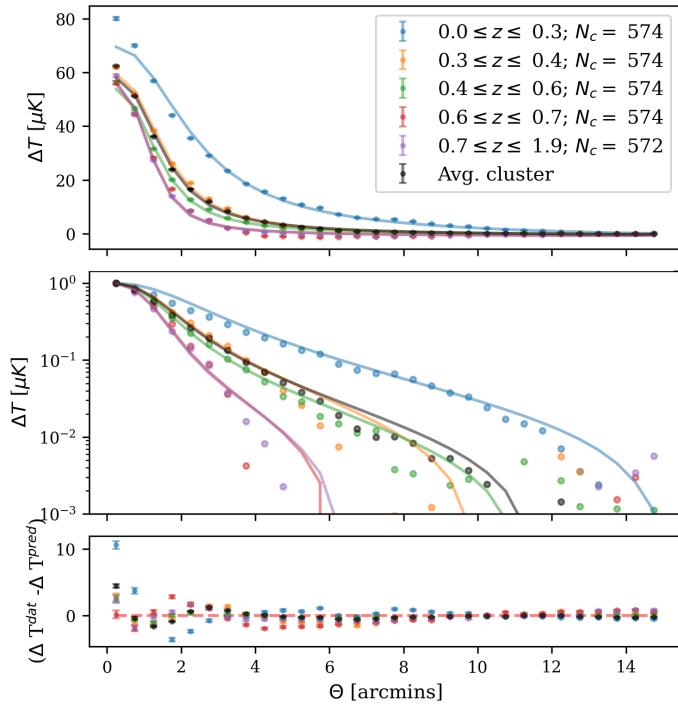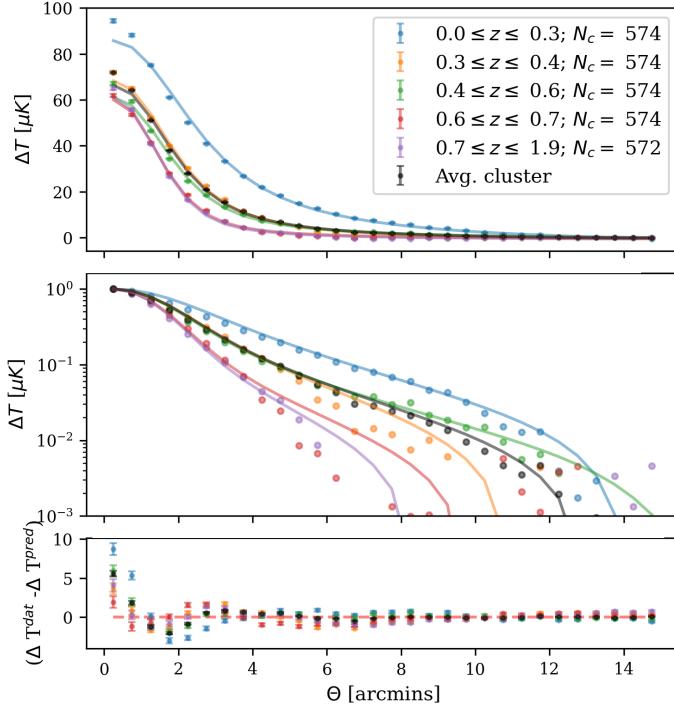
Figure 4.5: The plots in the figure show the best fits of the Isothermal β model with respect to the ΔT radial profiles of the average clusters stacked by redshift at both 90 (top) and 150 (bottom) GHz. Each plot is separated in 3 rows following the convention established in Sec.4.1.2. The legend on the top right identifies each redshift range and their corresponding number of clusters N_c, associating to each of them a color which is kept the same along the 3 rows.

4.1.3 The Universal Pressure Profile (UPP)

As we did for the Isothermal β model, also in the context of the UPP, it is useful to exploit the linear relationship between the Compton y-parameter and the thermal decrements to obtain a fitting function for the latter. As we briefly mentioned at the end of Sec.2.2.3, in the UPP framework there is no analytical form expressing $y(\theta)$ which remains simply defined as the integral of the pressure profile along the line of sight. Hence, the fitting function for $\Delta T(\theta)$ takes the general form:

$$\Delta T(\theta) = \delta T_{0,a} \int_\theta^\infty \frac{s}{\sqrt{s^2 - \theta^2}} \mathcal{P}(s) ds + c_{0,a}, \tag{4.6}$$

where $\mathcal{P}(\theta)$ is the normalized GNFW pressure profile:

$$\mathcal{P}(\theta) = \frac{1}{(c_{500}x)^\gamma [1 + (c_{500}x)^\alpha]^{\frac{\beta-\gamma}{\alpha}}}, \tag{4.7}$$

with $x = \theta/\theta_{500c}$ and $[c_{500}, \alpha, \beta, \gamma] = \{1.177, 1.0510, 5.4905, 0.3081\}$ as determined by Arnaud et al. in [4]. The free parameters in this model are $\delta T_{0,a}$, θ_{500c} and $c_{0,a}$, which are equivalent to $\delta T_{0,\beta}$, θ_c and $c_{0,\beta}$ from the fitting function of the Isothermal β Model. That said, though both θ_{500c} and θ_c specify the angular distance associated with the size of a cluster, they are defined in terms of two different physical scales, namely R_{500c} and r_c, respectively defined in Sec.2.1.1 and 2.2.2.

It is important to emphasize that in deriving the fitting function for $\Delta T(\theta)$ in eq.4.6, we are disregarding the direct dependence of the pressure profile on the mass and redshift of a cluster, empirically derived by Arnaud et al. in [4] and shown in this paper in eq.2.22. This assumption is motivated by the fact that here we are interested in the fitting function for the radial profile of an averaged cluster within a certain mass and redshift range. Hence, the direct dependence on the mass and redshift of

the cluster profile is washed out by the averaging process and can be considered to be fully encapsulated by the normalization factor $\delta T_{0,a}$.

The results of this analysis are presented in Table 4.2 and shown visually in Figures 4.6 and 4.7, for both the mass and redshift stacking at 90 and 150 GHz. Similarly to what we did with the β-model study, the figures are again separated in 3 rows, which contain the equivalent metrics of comparison between the obtained fits (dashed lines) and the data (filled circles with respective error bars) defined earlier. The only differentiation is in the scaling of the angular radial distance θ which, for both the mid and bottom row, is expressed in log scale as a fraction of the estimated θ_{500c} ($\log(\theta/\theta_{500c})$). This is done in order to visually highlight the multiplicative factors that characterize the fall off of the ΔT profile as it approaches θ_{500c}.

Though some of the obtained χ_ν^2 are still very high, the UPP generally fits the data better than the β-model and is more consistent in its predictions. The variance between the estimated χ_ν^2 for different average clusters profiles is strongly reduced, with most of them $\lesssim 10$. As already noted in regards to the β-model, also the UPP fits perform significantly worse when applied to averaged clusters scaled by redshift instead of mass. This can be explained by the combination of 2 factors: (1) the more direct relation between the mass of a cluster and its profile shape, expressed in both eq.4.6 and 4.5 through the dependence respectively on θ_{500c} and θ_c; (2) the approximately flat redshift distribution of the ACT clusters with respect to their mass, which implies that when we average over any redshift bin, we include a rich array of masses. In contrast with what we observed for the β model, the distinct feature that arises from the plots in Figures 4.6 and 4.7 is a systematic overestimation of the central peaks of the profiles. This seems to be directly related to the approximately singular behaviour predicted by the UPP at small radii ($\theta/\theta_{500c} \lll 1$), as expressed in eq.4.6.

An interesting result comes again from the average cluster profile at the highest mass bin given by $11.4 \cdot 10^{14} M_\odot \leq M_{500c} \leq 14.1 \cdot 10^{14} M_\odot$. For this particular range, the UPP does not fit the data well with an estimated χ_ν^2 at least twice as large compared to those for all the other mass ranges considered. This outcome is hard to be explained without suggesting a possible limitation in the UPP model considered in this work when applied to extremely massive clusters ($M_{500c} \sim 10^{15} \cdot M_\odot$). In fact, on a statistical standpoint, if the model works well for all the other mass ranges, one would expect it to work equally good or better also for the highest mass bin, considering its extremely reduced statistics which results in larger error bars relatively to those at any other range. The most problematic assumption, implicit in the expression of the UPP model from eq.4.6, is the exclusion of the direct dependence of the pressure profile on the mass. This assumption was motivated on the basis of an averaging process between a large number of clusters, within a finely binned mass range. The highest mass bin from our sample only contains 3 clusters of highly variant mass estimates, so this assumption is clearly not valid, which explains the poorness of the fit obtained for this particular mass range.

Finally, the estimated values of θ_{500c} generally agree with the physical expectations: for a higher mass and redshift range, we get respectively a larger and lower estimate of θ_{500c}, within the statistical error provided [8].

---

[8]One may note that at both 90 and 150 GHz, the value of θ_{500c} obtained for the highest mass bin ($11.4 \cdot 10^{14} M_\odot \leq M_{500c} \leq 14.1 \cdot 10^{14} M_\odot$) is slightly lower than that for $8.8 \cdot 10^{14} M_\odot \leq M_{500c} \leq 11.4 \cdot 10^{14} M_\odot$. However this difference is still within the statistical error ($\pm \sigma_{\theta_{500c}}$) provided for both quantities; hence it should not be regarded as evidence for a potential flaw in the model itself.

Mass Stacking	θ_{500c} [arcmin]	$\sigma_{\theta_{500c}}$ [arcmin]	$\delta T_{0,a}$ [μK]	$\sigma_{\delta T_{0,a}}$ [μK]	$c_{0,a}$ [μK]	$\sigma_{c_{0,a}}$ [μK]	χ^2_ν
			Frequency 90 GHz				
$1.0 \leq M \leq 3.6$	14.0	0.3	14.6	0.3	-0.3	0.1	11.9
$3.6 \leq M \leq 6.2$	16.2	0.3	34.4	0.5	-0.7	0.2	4.8
$6.2 \leq M \leq 8.8$	25.6	0.6	58.9	0.9	-5.8	0.5	2.8
$8.8 \leq M \leq 11.4$	31.7	0.8	80.3	1.2	-13.3	1.1	3.2
$11.4 \leq M \leq 14.1$	28.3	1.6	125.9	4.3	-17.1	3.2	5.6
Tot. Avg.	15.1	0.3	16.8	0.2	-0.4	0.1	13.5
			Frequency 150 GHz				
$1.0 \leq M \leq 3.6$	10.9	0.3	14.6	0.3	-0.2	0.1	17.2
$3.6 \leq M \leq 6.2$	13.9	0.3	33.3	0.5	-0.4	0.1	5.1
$6.2 \leq M \leq 8.8$	26.2	0.9	53.3	1.2	-5.2	0.7	8.0
$8.8 \leq M \leq 11.4$	31.7	1.4	66.8	1.8	-9.4	1.3	6.5
$11.4 \leq M \leq 14.1$	29.5	2.3	110.1	5.4	-15.1	3.6	8.6
Tot. Avg.	12.2	0.3	16.4	0.3	-0.2	0.1	16.4

Redshift Stacking	θ_{500c} [arcmin]	$\sigma_{\theta_{500c}}$ [arcmin]	$\delta T_{0,a}$ [μK]	$\sigma_{\delta T_{0,a}}$ [μK]	$c_{0,a}$ [μK]	$\sigma_{c_{0,a}}$ [μK]	χ^2_ν
			Frequency 90 GHz				
$0.0 \leq z \leq 0.3$	32.0	1.4	17.5	0.4	-3.2	0.4	20.0
$0.3 \leq z \leq 0.4$	14.5	0.7	18.0	0.6	-0.7	0.2	18.2
$0.4 \leq z \leq 0.6$	14.7	0.4	15.5	0.3	-0.1	0.1	5.6
$0.6 \leq z \leq 0.7$	7.6	0.3	21.0	0.7	-0.1	0.1	5.3
$0.7 \leq z \leq 1.9$	7.3	0.4	21.6	1.0	-0.4	0.1	10.5
Tot. Avg.	15.1	0.3	16.8	0.2	-0.4	0.1	13.5
			Frequency 150 GHz				
$0.0 \leq z \leq 0.3$	32.4	1.6	14.9	0.4	-2.3	0.3	24.8
$0.3 \leq z \leq 0.4$	12.2	0.7	17.2	0.8	-0.5	0.2	26.7
$0.4 \leq z \leq 0.6$	10.0	0.2	16.5	0.3	-0.1	0.0	2.5
$0.6 \leq z \leq 0.7$	5.8	0.5	23.2	2.0	-0.6	0.1	30.2
$0.7 \leq z \leq 1.9$	5.7	0.4	23.2	1.5	-0.5	0.1	18.4
Tot. Avg.	12.2	0.3	16.4	0.3	-0.2	0.1	16.4

Table 4.2: The two tables contain a report of the best fits of the Universal Pressure Profile as expressed in eq.4.6, to the average clusters profiles stacked by mass (top) and redshift (bottom) at both 90 and 150 GHz. For each fit, the tables include the estimated values for the free parameters (θ_{500c}, $\delta T_{0,a}$, $c_{0,a}$), their respective statistical errors ($\sigma_{\theta_{500c}}$, $\sigma_{\delta T_{0,a}}$, $\sigma_{c_{0,a}}$) and the resulting χ^2_ν. All quantities are reported with precision to 1 decimal place.
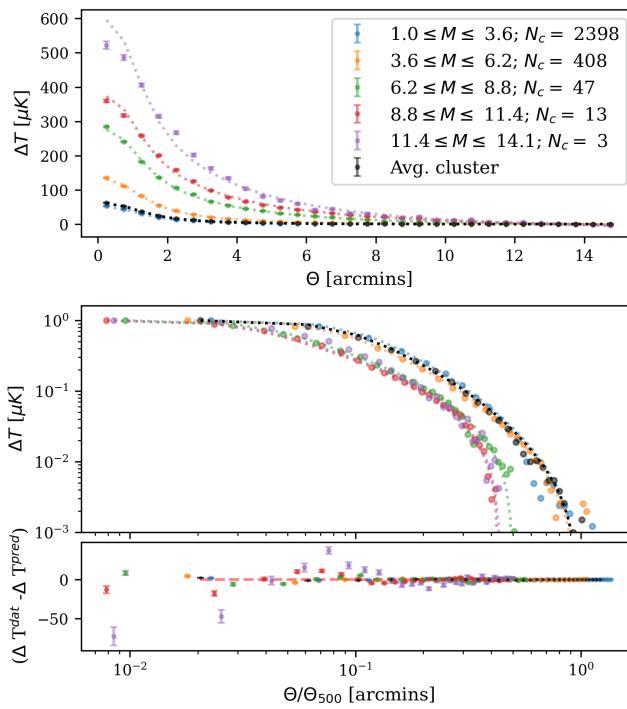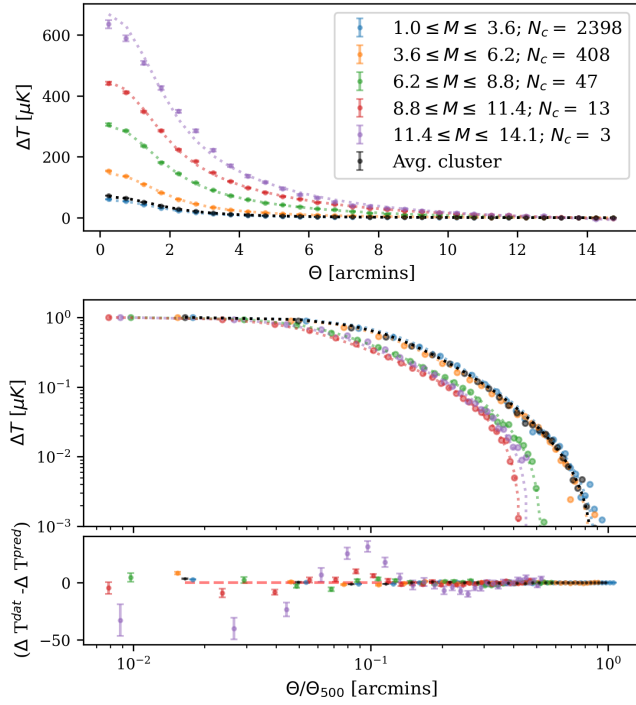
Figure 4.6: The plots in figure show the best fits of the UPP model with respect to the ΔT radial profiles of the average clusters stacked by mass at both 90 (top) and 150 (bottom) GHz. Each plot is separated in 3 rows following the convention reestablished in Sec.4.1.3 . The legend on the top right identifies each mass range and their corresponding number of clusters N_c, associating to each of them a color which is kept the same along the 3 rows.

61
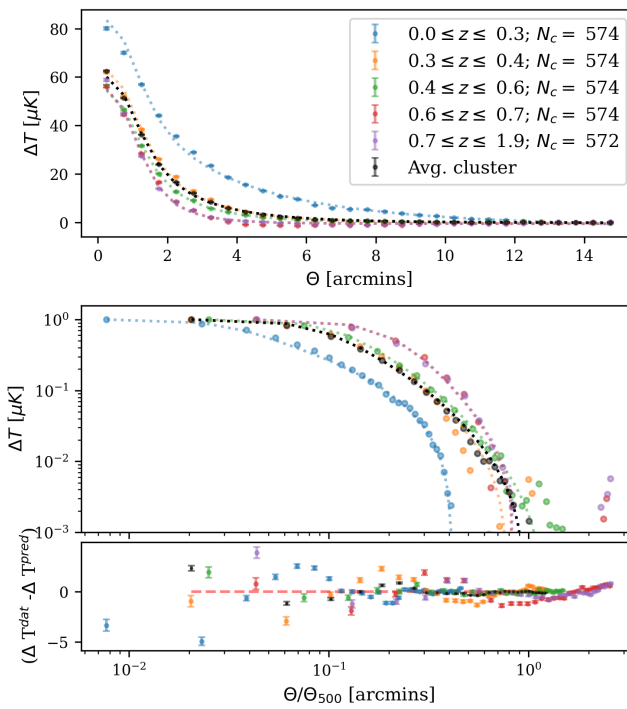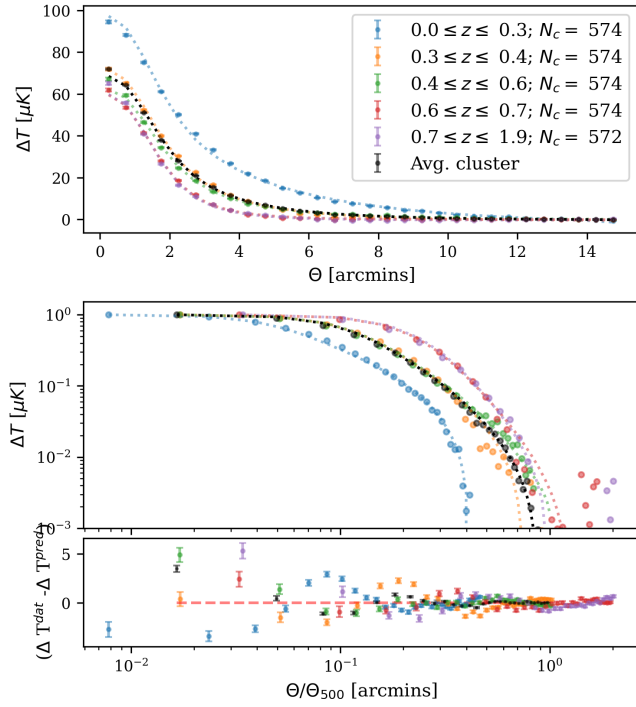
Figure 4.7: The plots in figure show the best fits of the UPP model with respect to the ΔT radial profiles of the average clusters stacked by redshift at both 90 (top) and 150 (bottom) GHz. Each plot is separated in 3 rows following the convention reestablished in Sec.4.1.3. The legend on the top right identifies each redshift range and their corresponding number of clusters N_c, associating to each of them a color which is kept the same along the 3 rows.

4.2 Linear Polarization

In addition to a thermal spectral distortion, the SZ effect is also expected to induce linear polarization in the CMB. The SZE polarization comes entirely from the the presence of a quadrupole component in the of the local radiation field experienced by the scattering electrons [3]. This quadrupole anisotropy is mostly inherent to the CMB radiation itself, or induced by the motion of the cluster with respect to the CMB [56].

If we could obtain polarization measurements for a large number of clusters on a finely binned redshift range, we could potentially trace the evolution of the CMB quadrupole and use that to make several tests on the cosmology of the Universe, such as on its homogeneity [57] or on the nature of dark energy[9] [58]. The non-relativistic SZ effect polarization signal for a massive cluster with optical depth $\tau_e \approx 0.01$ is expected to be $\sim 0.1\mu K$ [3], which is still below the detection limit of current instruments by approximately an order of magnitude. That said, as commented in [59] one can overcome such limitation by averaging polarization signals from a large number of clusters. This corresponds exactly to the nature of the stacking analysis described in this chapter where the average is taken among all the observed clusters in our catalog at a specific redshift and mass range.

Hence here, to investigate whether or not there is a detectable net polarized signal from the average cluster per mass and redshift bin, one must compute the radial profiles of the linear polarization P, by applying the same inverse-variance weighted averaging procedure presented in the introductory section of this chapter[10].

---

[9]By performing such study, the presence of the Integrated Sachs-Wolfe (ISW) effect, which is strongly dependent on the background cosmology and hence on the nature of dark energy, can be statistically established and its redshift dependence contribution to the r.m.s. quadrupole determined [56].

[10]It is useful to recall here that the methodology used throughout this work to obtain the finalized radial profiles with their associated error bars involves two distinguished weighted averaging steps: (1) the stacking of the 30×30 arcmins square patches centered on the clusters for each redshift and

The procedure is performed on the P maps whose signal and weights are fully determined by the Stokes parameters Q and U polarization maps.

Before moving on with this study, it is useful to look at the radial profiles for the single Q and U polarization maps. In fact, even if we detect a distinct total polarization P coming from the clusters, the radial profiles of the single Stokes parameters Q and U should still act like pure noise with mean value zero. This is because, if there is an axis of polarization, one expects that to be random among the class of clusters analyzed. Hence, since Q and U are coordinate dependent, their weighted average around many distinct points in the sky, which here correspond to the clusters positions, should tend to zero. This is also a useful test for systematic errors in the map, which in this case would manifest as a non-zero baseline level.

Figure 4.8 shows the radial profiles of Q and U at both 90 and 150 GHz, computed for the clusters stacked by redshift[11]. It is important to note that in calculating these profiles, the weights on both the Q and U maps are taken to be the same as those from the thermal map. As expected, the Stokes parameters oscillate around the zero value with a scatter for both U and $Q \lesssim 1\mu\text{K}$. To verify this quantitatively, we fit using χ^2 minimization a flat line of the form $f(\theta) = b$, where b is a constant representing the baseline. For all the Q and U radial profiles considered, the best fit is given by $b = 0.0$ with corresponding $\chi^2_\nu \sim 2$, minimum value 1.0 and maximum at 4.2. The extensive list of all the computed χ^2_ν for the radial profiles of Q and U under consideration is reported in Table C.2 for the interested reader.

---

mass bin; (2) the averaging of all the pixels at dimensionless distance θ from the single stacked 30×30 arcmins square patches associated to each mass and redshift group.

[11]In a similar fashion, one can analyze the Q and U radial profiles with respect to the mass stacking subdivision. The results should be equivalent with the only differences arising form the different statistics of each stacking group. Hence, in an effort to avoid being prolix, we do not include this in the discussion. The redshift stacking is preferred purely for graphing purposes since, given the equal number of clusters in each subgroup, the scatter between the maximum and minimum value for Q and U is reduced.
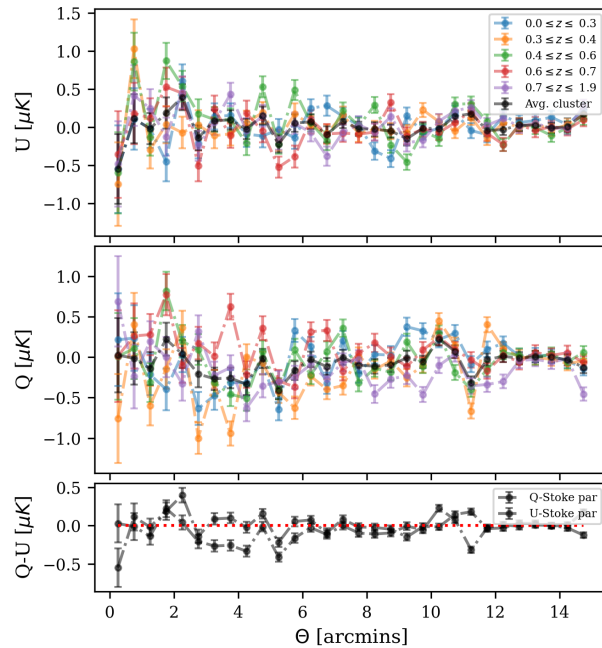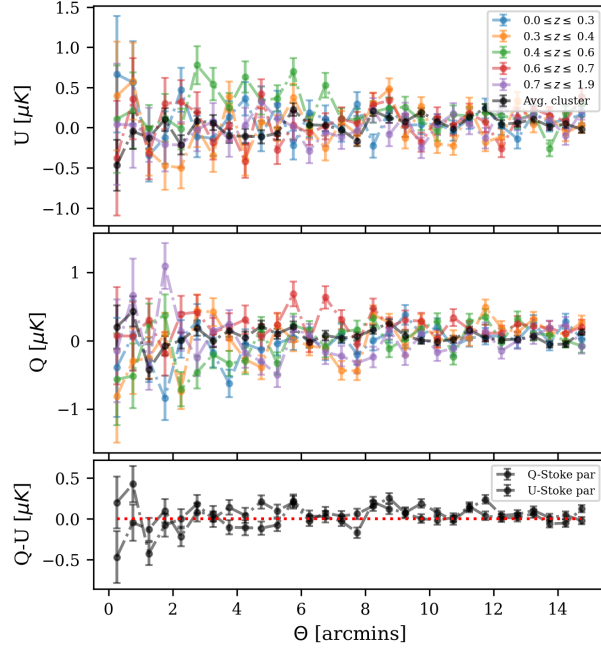
Figure 4.8: The 2 plots in the figure show the radial profiles of the Stokes parameters Q and U for the clusters groups stacked by redshift at both 90 (top) and 150 (bottom) GHz. Each plot is separated in three row. The top-row and mid-row contain the radial profiles of all the clusters groups analyzed respectively for U (top-row) and Q (mid-row). The bottom row instead shows a comparison between the total average profile of Q and U and contains an additional flat dotted red line at $Q = U = 0$. The legend on the top right identifies each redshift range, associating to each of them a color which is kept the same along the top and mid rows.

Having verified the absence of a non-negligible baseline level in the Q and U polarization maps, we are now ready to return to the study of the total linear polarization P.

The signal P is defined in terms of Q and U by equation 1.11, its corresponding weights w_P are also specified by this relation according to the standard rules of error propagation[12] and the definition of inverse-variance weighting (see eq.4.1), such that:

$$\text{since } w_Q = w_U = w_T, \text{ by eq.4.1} \rightarrow \quad \sigma_Q = \sigma_U = \sigma_T$$

$$\text{given eq.1.11, by err. prop. rules} \rightarrow \quad \sigma_P = \sigma_T \qquad (4.8)$$

$$\text{by eq.4.1} \rightarrow \quad w_P = w_T. \qquad (4.9)$$

Hence, similarly to the Q and U maps, also the P map has weights equal to those of the thermal map.

Now, since P is given by the quadrature addition of Q and U, its averaged radial profiles will include a rather large constant baseline level which has no physical significance with respect to our investigation. Therefore, in order to resolve the relatively small net polarized signal, it is crucial to subtract this mean noise level to each of the finalized average radial profiles. The resulting profiles of the linear polarization P after mean subtraction are shown in Figure 4.9 for both the mass and redshift stacking at 90 and 150 GHz. The outcome is evident: we observe no net polarization signal neither for the clusters averaged over mass range, nor for those averaged over redshift range. To verify this quantitatively, as we did for the Stokes parameters Q and U, we can fit to each of the profiles a flat line of the form $f(\theta) = b$.

---

[12]Specifically, we used the summation and power rule which state that:

$$\text{for } Z = X + Y \longrightarrow \quad \sigma_Z^2 = \sigma_X^2 + \sigma_Y^2$$

$$\text{for } Z = X^n \text{ and } n \in Q \longrightarrow \quad \frac{\sigma_Z}{Z} = n \cdot \frac{\sigma_X}{X}$$

Stacking Group	χ^2_ν (90 GHz)	χ^2_ν (150 GHz)
$0.0 \leq z \leq 0.3$	1.2	1.3
$0.3 \leq z \leq 0.4$	0.9	2.1
$0.4 \leq z \leq 0.6$	0.8	1.8
$0.6 \leq z \leq 0.7$	1.0	1.9
$0.7 \leq z \leq 1.9$	1.1	1.2
$1.0 \leq M \leq 3.6$	0.9	1.4
$3.6 \leq M \leq 6.2$	1.0	1.3
$6.2 \leq M \leq 8.8$	1.4	1.7
$8.8 \leq M \leq 11.4$	1.0	2.0
$11.4 \leq M \leq 14.1$	1.4	2.1
Tot. Avg.	1.1	1.3

Table 4.3: The table contains a report of the χ^2_ν obtained by fitting a flat line of the form $f(\theta) = 0$ to the P radial profiles for all the clusters groups stacked both by redshift and mass at 90 (inner-column) and 150 GHz (outer-column). Overall, $\chi^2_\nu \sim 1$ for approximately all the stacking groups considered, with only a few exceptions which present values of $\chi^2_\nu \sim 2$, to not be considered as a statistically significant variation. All quantities are reported with precision to 1 decimal place.

If there is no net polarization and hence the signal is characterized as pure noise with mean 0, then we expect the best fitting function to have $b = 0.0$ and corresponding $\chi^2_\nu \approx 1$. This expectation is matched by the results of the χ^2 minimization algorithm which for all profiles provides the best fit at $b = 0$ and $\chi^2_\nu \sim 1$, with maximum value at 2.1 and minimum at 0.8 (refer to Table 4.3 for the extensive list). This confirms the absence of a discernible linear polarization signal arising from clusters as evidenced by Fig.4.9.
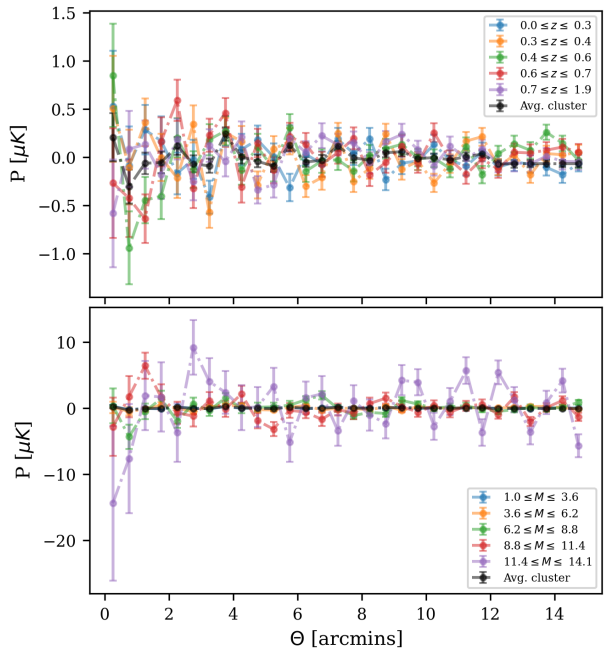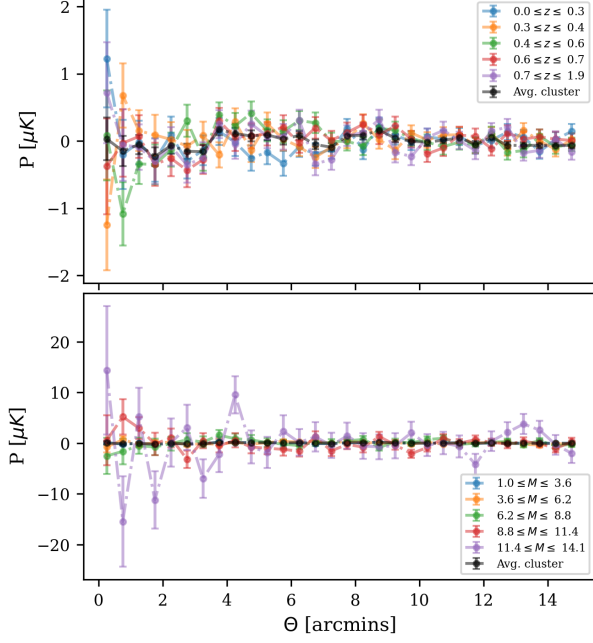
Figure 4.9: The 2 plots in figure show the radial profiles of the linear polarization P for the clusters groups stacked by both redshift and mass at 90 (top) and 150 (bottom) GHz. Each plot is separated in 2 rows respectively representing the stacking by redshift (top-row) and mass (bottom-row). The legend on the top right of both identifies each mass and redshift range, associating to them a color which is kept the same along the top and bottom plot.

4.3 Planck clusters in the ACT S18dn equatorial map
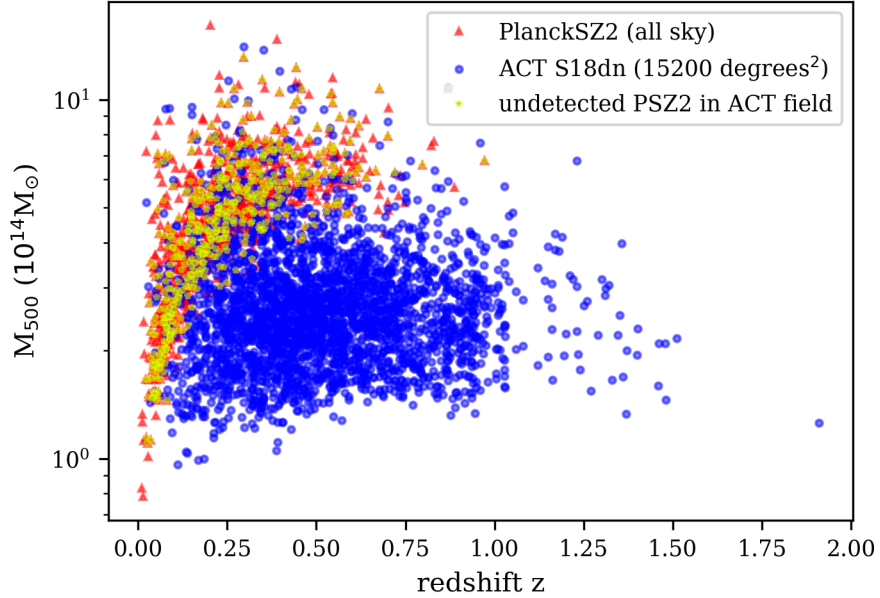
Figure 4.10: The figure shows a comparison of the ACT S18dn cluster sample in the (mass, redshift) plane with the PlanckSZ2 (PSZ2) catalog[1]. In yellow, we evidenced the 525 clusters observed by Planck that are in the overlapping field of the two experiments but were not detected by ACT.

The all-sky Planck Satellite cluster survey (PlanckSZ2) differs notably from the corresponding ground-based surveys, such as ACT and SPT, specifically in terms of angular resolution, available frequency channels and sky coverage. The Planck CMB maps are mainly free from astrophysical emission and are thus considered a good representation of the statistical instrumental noise [60]. Conversely, for a ground-based experiment like ACT, the noise properties can vary significantly due to changes in the atmospheric conditions that can result in spatial variations at large angular scales. On the other hand, ACT presents a higher angular resolution at ~ 1 arcmin level compared to ~ 5 arcmin for the highest Planck frequencies. The higher resolution of ACT allows to detect SZ clusters and characterize their pressure profiles on smaller angular scales. Similarly, the extensive multi-frequency coverage and the

absence of atmospheric noise of Planck allows access to larger angular scales clusters which are instead filtered out in ground experiments like ACT [60].

Figure 4.10 evidences the complementarity between the ACT S18dn and PlanckSZ2 sample: ACT S18dn presents clusters at lower mass and higher redshift since they correspond to a smaller angular scale; PlanckSZ2 presents clusters at lower redshift which correspond to larger angular sizes. It becomes clear then the combination of ACT and Planck data would provide a more complete picture of the total distribution of clusters in the Universe. Hence a combined survey offers a unique opportunity to improve on the study of the intra-cluster pressure profiles and potentially extrapolate tighter constraints on cosmological parameters.

PlanckSZ2 contains 1,653 detections, of which 1,094 are confirmed clusters with assigned mass M_{500c} and redshift. Within this verified catalog, there are 525 clusters in the overlapping region with the ACT S18dn field that were not detected by the ACT experiment[13].

The primary goal of this section is simply to verify if these undetected 525 Planck clusters can be resolved in the unfiltered ACT S18dn equatorial map. To do this, we apply the same averaging formalism used throughout this chapter, and stack the $30{\times}30$ arcmins square patches from the ACT maps centered on the 525 Planck clusters over 3 mass ranges[14]. Similarly to what we did for the ACT S18dn catalog, here the mass ranges are equally spaced with width $w = \frac{1}{3}(M_{\max} - M_{\min}) = 3.7{\times}10^{14} M_{\odot}$, where $M_{\max}$ and $M_{\min}$ represent respectively the highest and lowest estimated mass from the Planck clusters. The result of this process is shown in Figure 4.11. The immediate observation is that when stacked on top of each other, the Planck clusters become

---

[13]the ACT S18dn and PlanckSZ2 catalog have 28 clusters in common which are not considered in this analysis.

[14]The maps taken into account are both the thermal and polarization maps at 90 and 150 GHz. Moreover the position and respective masses and redshifts of all the Planck clusters are taken from the public dataset of PlanckSZ2 survey available at [1].

clearly visible in the ACT temperature map at both 90 and 150 GHz, with noise levels comparable to the original ACT S18dn sample.
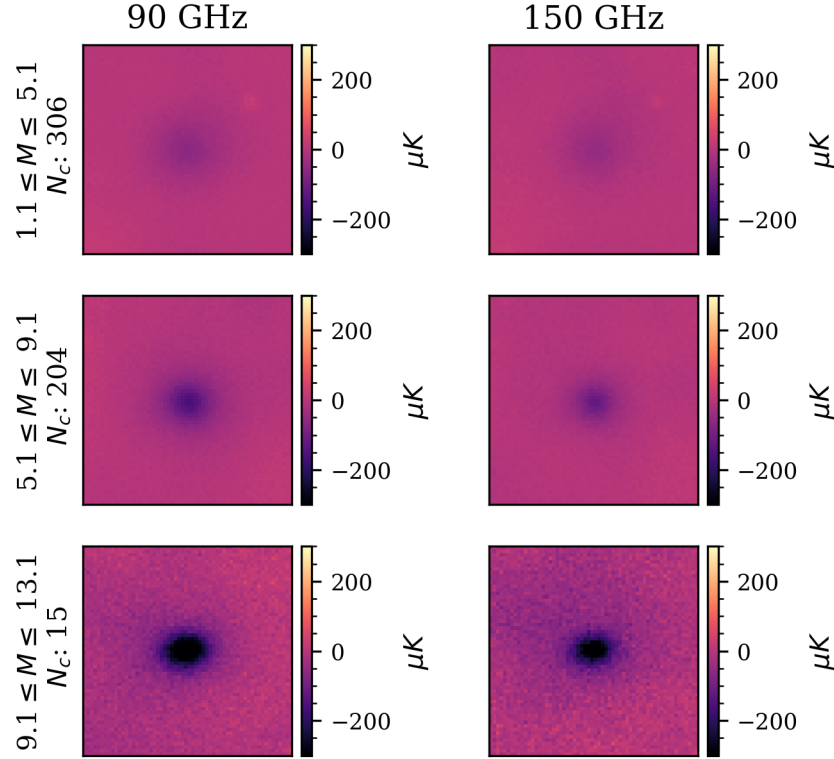
Figure 4.11: The images present the average clusters from the PlanckSZ2 dataset for 3 different mass ranges of equal width $w = \frac{1}{3}(M_{\max} - M_{\min}) = 3.7 \times 10^{14} M_\odot$. N_c represents the number of clusters on which the weighted average is computed in each mass range. On the left, the frequency under consideration is 90 GHz; on the right, 150GHz. Note that we only consider here the PlanckSZ2 clusters in the overlapping region with the ACT S18dn that were not detected by the ACT collaboration.

It is important to emphasize that the mass estimates of these clusters are those computed by the Planck collaboration whose model template, though still based on the UPP, differs from that used by the ACT collaboration and described in Sec.3.2.1. The details of this method are of no interest for the purpose of this work since the estimated masses are only used to determine the stacking measure; for the curious reader, we suggest to refer to [38] and [61]. Finally, in this analysis we disregard the

redshift stacking. This is mainly a pictorial choice for immediate physical pleasure. In fact, as evidenced by the study on the ACT S18dn catalog, in contrast with the average profiles scaled by mass, there is a significantly smaller variability among those scaled by redshift, which makes them harder to be differentiated on a purely graphic level. This is just the consequence of the more direct correlation between the estimated mass of a cluster and its intrinsic properties, manifested here in terms of the induced central thermal decrements in the CMB map and the overall profile shape.

Following the same methodology undertaken for the analysis of the entire ACT S18dn catalog, in the following subsections we examine the Planck clusters to: (1) test the predictions of the Isothermal β model and Universal pressure profile by looking at the thermal radial profiles of the average clusters per mass bin (2) investigate whether or not there is a detectable net polarized signal coming from the clusters by computing the radial profiles of the linear polarization P.

4.3.1 Testing Pressure Profiles

Given the radial profiles of the mass scaled average clusters computed according to the formalism presented in Sec.4.1, we can test them through χ^2 minimization on the two major cluster pressure profile models under consideration, namely the Isothermal β model and the Universal Pressure Profile.

For the Isothermal β model, we use the same fitting function from eq.4.5 with $\delta T_{0,\beta}$, θ_c and $c_{0,\beta}$ taken as free parameters and β fixed at 0.9 for both the 90 and 150 GHz map [15]. Similarly, to test the Universal Pressure Profile, we use the same fitting function from eq.4.6 with free parameters $\delta T_{0,a}$, θ_a and $c_{0,a}$. The results of this analysis are shown in Table 4.4 and 4.5 and Figures 4.12 and 4.13, respectively,

---

[15]This value corresponds to that estimated for the total average cluster in the ACT S18dn sample, in the preliminary study where β was left free.

for the maps at 90 at 150 GHz. Each of the 2 figures is separated in 5 rows. The top row simply contains the radial profiles from the data in standard linear scale. The 2nd and 3rd row are dedicated to the comparison between the data and the fits from the β model respectively containing: (2nd-row) the radial profiles of the data and corresponding best fits normalized to 1 at their peak and put in log scale; (3rd-row) the residuals between the data and corresponding fits ($\Delta T^{\mathrm{dat}} - \Delta T^{\mathrm{pred}}$) with the additional flat dotted red line at $\Delta T = 0$ as done for the analysis of the ACT clusters. Finally, the last two rows follow the same structure and are instead dedicated to the comparison between the data and the fits from the UPP model. The only differentiation, as done for the ACT clusters, is again in the scaling of the angular radial distance θ which in these last two rows is expressed in log scale as a fraction of the estimated θ_{500c} ($\log(\theta/\theta_{500c})$).

Overall for this study, the β model fits the data fairly well, with all the values of $\chi_\nu^2 \lesssim 10$ and minimum $\chi_\nu^2 = 1.2$. That said, the estimated values of the angular core-radius θ_c decrease as one increases the value of the mass bin, which is generally an nonphysical result if the clusters in each mass bin are approximately evenly distributed in redshift. However, as one can clearly observe from Figure 4.14, the masses and corresponding redshifts of the undetected PLanckSZ2 clusters are positively correlated, introducing an important selection effect which may account for the unexpected shrinking of θ_c for the clusters in the higher mass ranges.

Conversely to what we observed for the ACT clusters, here the UPP generally performs worse than the β model, providing extremely high values of $\chi_\nu^2 \sim 10^2$. This differentiation is particularly enhanced for the average clusters profiles of the two lower mass bins. The distinctive feature of these two profiles is the combination of a very long tail with relatively low peak, that then results in physically unreasonable estimates for UPP fitted parameters, suggesting perhaps a limitation of this model when used to describe light clusters with very large angular sizes. Indeed, when

73

one considers the average cluster from the highest mass bin, which does not present this distinctive elongated tail, then the UPP performs much better and comparably to what we obtained for the two highest mass ranges from the ACT sample, with $\chi^2_\nu \lesssim 10$.

With all this said, the essence of this profile analysis is not to make any conclusive argument on the flaws of the UPP and/or on the nature of the correct pressure profile to use. There are many elements that we are neglecting for simplicity and that could strongly impact the statistical significance of our fitted models [16]. Hence, all we can really claim is the evident distinction between the average profiles on the two lower mass bins from the undetected PlanckSZ2 clusters compared to all the other profiles presented in this work. This contrast is emphasized even more in Figure 4.14 where we compare the profiles from the undetected PlanckSZ2 clusters with the ACT S18dn clusters sample stacked over the same 3 mass ranges.

The average clusters on the lowest mass bin diverge at almost all scales, with the the PlanckSZ2 cluster characterized by both a smaller peak and longer tail. For the second mass bin, the profiles agree for $\theta \geq 5$ arcmin and only diverge significantly in the core, with the PlanckSZ2 cluster identified again by a smaller peak. Overall, these two PlanckSZ2 clusters groups seem to perfectly pertain to the class of objects with low mass and large angular size that tend to be filtered out in ground experiments like ACT. On the other hand, as clearly shown in Fig.4.14, the average clusters profiles on the highest mass bin are much more coherent with only small differences that, given the low statistics of the average, can be considered to be negligible. This is also very interesting in itself, because one may ask why clusters with such similar features that seem to be in the ACT resolution range were not detected.

---

[16]e.g., the different mass calibration between the two experiments, the noise in the map coming from bright sources, the use of a simplified version of the UPP without the direct mass dependence, etc.

We must recall, as we mentioned at the very beginning of this thesis, the ACT S18dn dataset studied here is only a preliminary version but, if it will be confirmed, being able to explain the nature of these exclusions will become more pressing and may involve non negligible differences in the mass calibration between the two experiments or inaccurate estimates of the completeness of the survey.
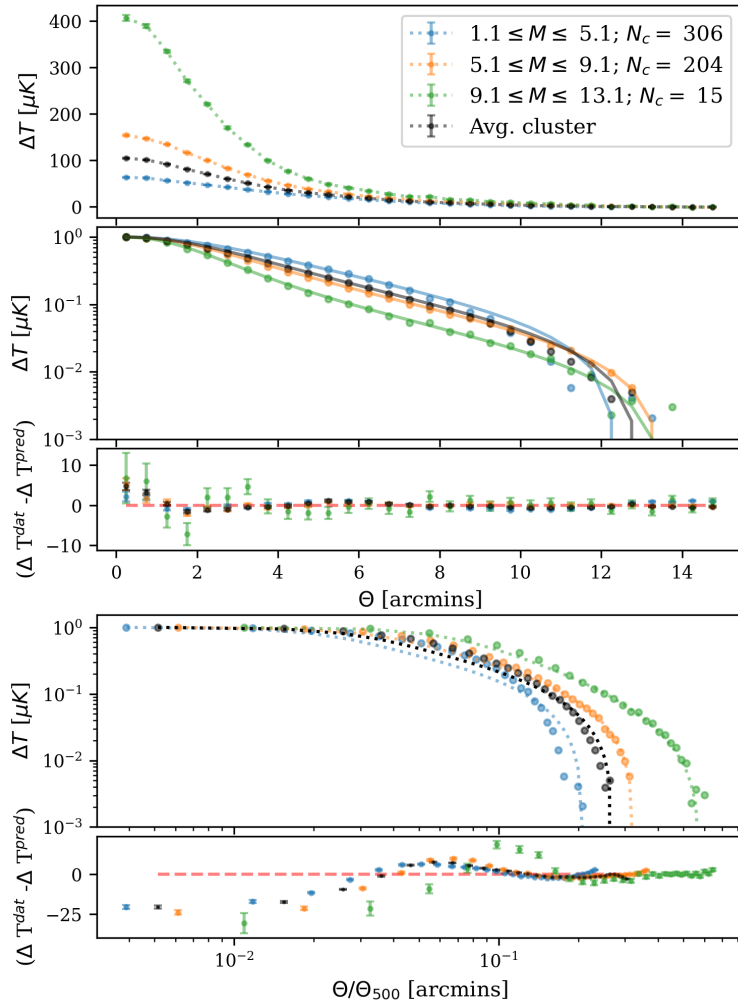
Figure 4.12: The plots in the figure show the best fits of the β-model (2nd-3rd row) and of the UPP (4nd-5rd row) with respect to the ΔT radial profiles from the undetected PlanckSZ2 clusters stacked by mass at 90 GHz. The legend on the top right identifies each mass range and their corresponding number of clusters N_c, associating to each of them a color which is kept the same along the 5 rows. The performance of the fits can be evaluated by looking at the plots of the residuals (3rd and 5th row) which are approximately flat for the β-model and evidently oscillatory for the UPP, which overall seems to overestimate the core and underestimate the tail of the profiles.
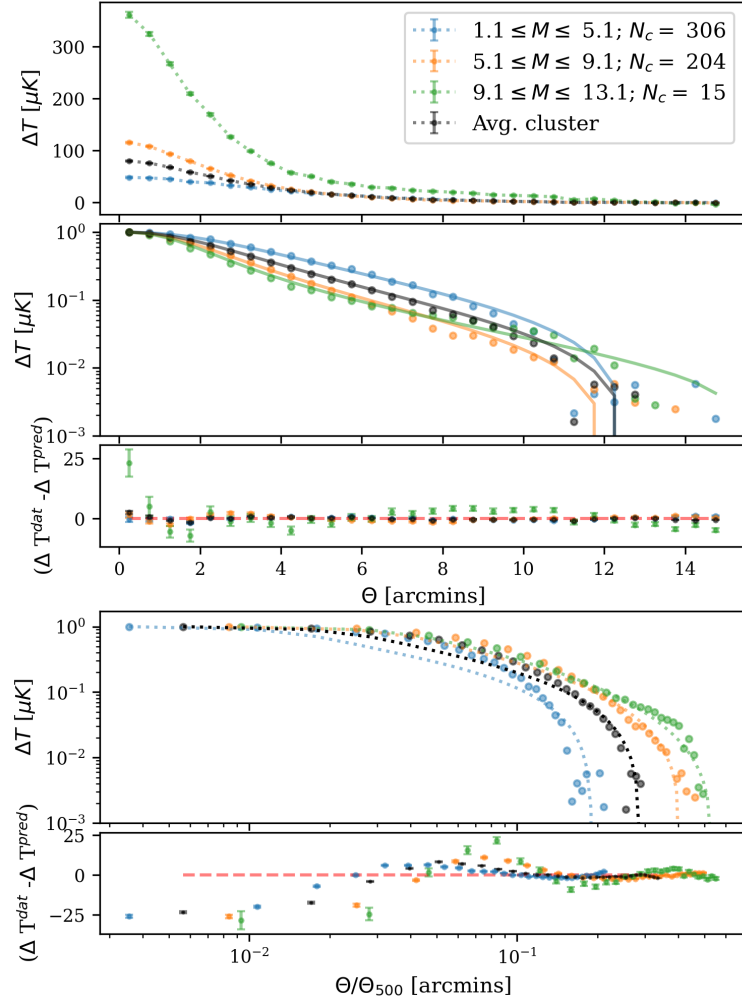
Figure 4.13: This plot is equivalent to that in Figure 4.12 for the map at 150 GHz. Overall the results are in line with what is shown in the previous figure, with the common tendency of obtaining slightly worse fits at this frequency.
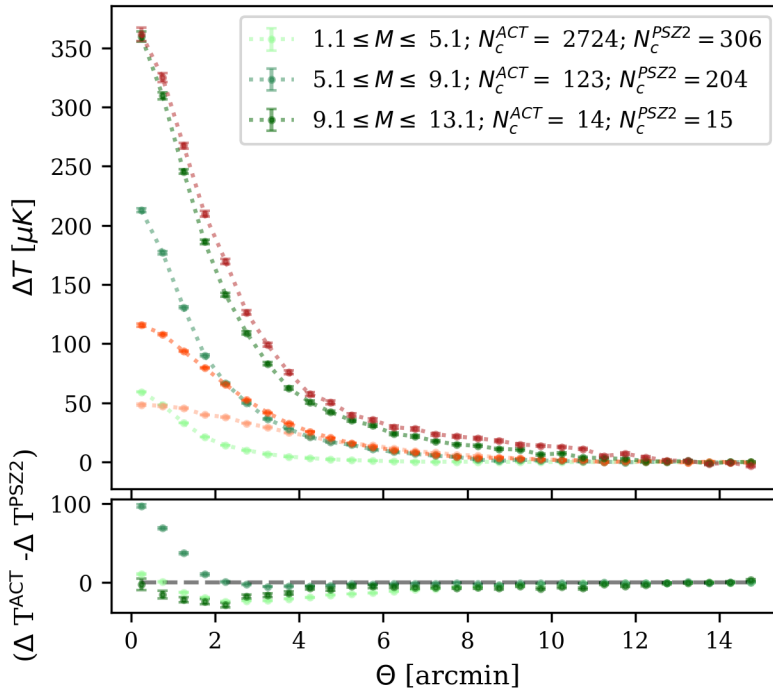
Figure 4.14: The plot shows a comparison of the average cluster profiles stacked over the same mass range between the ACT S18dn catalog and the 525 undetected PlanckSZ2 (PSZ2) clusters. The PSZ2 and ACT profiles are respectively in shades of red and green, with the lightest shade corresponding to the lowest mass bin and the darkest shade to highest mass bin. The legend on the top right identifies each mass range and their corresponding number of clusters N_c for both the ACT and PSZ2 sample. Finally on the bottom, we plot the residuals defined as the difference between the ACT and PSZ2 profiles at each θ bin for all the 3 mass ranges under consideration. Each of the residuals profiles is labeled with the same color of the corresponding ACT cluster profiles of the top plot.

Mass Stacking	$\delta T_{0,\beta}$ [μK]	$\sigma_{\delta T_{0,\beta}}$ [μK]	θ_c [arcmin]	σ_{θ_c} [arcmin]	$c_{0,\beta}$ [μK]	$\sigma_{c_{0,\beta}}$ [μK]	χ^2_ν
Frequency 90 GHz							
$1.1 \leq M \leq 5.1$	68.8	1.1	3.4	0.1	-7.3	0.5	11.5
$5.1 \leq M \leq 9.1$	158.3	0.7	2.2	-	-7.6	0.2	1.9
$9.1 \leq M \leq 13.1$	420.3	3.1	1.5	-	-10.0	0.4	1.2
Tot. Avg.	108.1	0.9	2.6	-	-7.1	0.3	8.8
Frequency 150 GHz							
$1.1 \leq M \leq 5.1$	54.7	1.0	3.4	0.1	-5.7	0.4	12.4
$5.1 \leq M \leq 9.1$	121.1	2.0	1.9	-	-5.0	0.3	14.5
$9.1 \leq M \leq 13.1$	352.4	7.8	1.5	-	-6.2	0.9	7.8
Tot. Avg.	83.3	1.0	2.4	-	-4.9	0.2	11.8

Table 4.4: The table contains a report of the best fits of the Isothermal β model as expressed in eq.4.5, to the average clusters profiles from the 525 undetected PlanckSZ2 clusters stacked by mass at both 90 and 150 GHz. For each fit, the table includes the estimated values for the free parameters ($\delta T_{0,\beta}$, θ_c, $c_{0,\beta}$), their respective statistical errors ($\sigma_{\delta T_{0,\beta}}$, σ_{θ_c}, $\sigma_{c_{0,\beta}}$) and the resulting χ^2_ν. All quantities are reported with precision to 1 decimal place. The dash – in defined according to the same convention expressed in the caption of Table 4.1.

Mass Stacking	θ_{500c} [arcmin]	$\sigma_{\theta_{500c}}$ [arcmin]	$\delta T_{0,a}$ [μK]	$\sigma_{\delta T_{0,a}}$ [μK]	$c_{0,a}$ [μK]	$\sigma_{c_{0,a}}$ [μK]	χ^2_ν
Frequency 90 GHz							
$1.1 \leq M \leq 5.1$	63.9	21.3	12.0	1.6	-8.1	3.5	126.2
$5.1 \leq M \leq 9.1$	40.8	4.5	29.4	1.6	-9.1	2.1	79.6
$9.1 \leq M \leq 13.1$	22.9	1.1	89.6	2.8	-6.9	1.5	9.3
Tot. Avg.	48.5	7.9	19.6	1.5	-8.5	2.3	178.3
Frequency 150 GHz							
$1.1 \leq M \leq 5.1$	70.2	33.3	10.2	1.8	-7.0	4.0	154.8
$5.1 \leq M \leq 9.1$	29.8	3.7	26.2	2.0	-4.3	1.4	116.2
$9.1 \leq M \leq 13.1$	26.8	1.9	74.5	3.4	-5.8	2.0	14.0
Tot. Avg.	44.1	8.2	16.6	1.5	-5.7	1.9	210.5

Table 4.5: The table contains a report of the best fits of the Universal Pressure Profile as expressed in eq.4.6, to the average clusters profiles from the 525 undetected PlanckSZ2 clusters stacked by mass at both 90 and 150 GHz. For each fit, the tables include the estimated values for the free parameters (θ_{500c}, $\delta T_{0,a}$, $c_{0,a}$), their respective statistical errors ($\sigma_{\theta_{500c}}$, $\sigma_{\delta T_{0,a}}$, $\sigma_{c_{0,a}}$) and the resulting χ^2_ν. All quantities are reported with precision to 1 decimal place.

Stacking Group	χ^2_ν (90 GHz)	χ^2_ν (150 GHz)
$1.1 \leq M \leq 5.1$	1.1	1.7
$5.1 \leq M \leq 9.1$	1.1	1.3
$9.1 \leq M \leq 13.1$	0.9	1.8
Tot. Avg.	1.0	1.3

Table 4.6: The table contains a report of the χ^2_ν obtained by fitting a flat line of the form $f(\theta) = 0$ to the P radial profiles for the average Planck clusters stacked by mass at both 90 (inner-column) and 150 GHz (outer-column). Overall, similarly to what we obtained for the ACT clusters, $\chi^2_\nu \sim 1$ for approximately all the stacking groups considered, with only a few exceptions that do not represent a statistically significant variation. All quantities are reported with precision to 1 decimal place.

4.3.2 Linear Polarization

Following the same procedure indicated in Sec.4.2, in order to study the potential net polarized signal from the average PlanckSZ2 clusters, we must compute the radial profiles of the linear polarization P for each mass bin and subtract the relative mean noise level. It is useful to recall that since we are still simply examining the ACT S18dn map, the weights on the P maps are, as derived in Sec.4.2, equal to those from the thermal maps.

Figure 4.15 shows the resulting profiles of the linear polarization P after mean subtraction at both 90 and 150 GHz. As for the entire ACT S18dn dataset, also for these 525 undetected Planck clusters we observe no discernible polarization signal coming arising from clusters. Quantitatively, this is confirmed by the χ^2_ν values obtained from the fit of all the P profiles with the function $f(\theta) = 0$. As presented in Table 4.6, all the computed $\chi^2_\nu \sim 1$, with maximum value at 1.8 and minimum at 0.9.
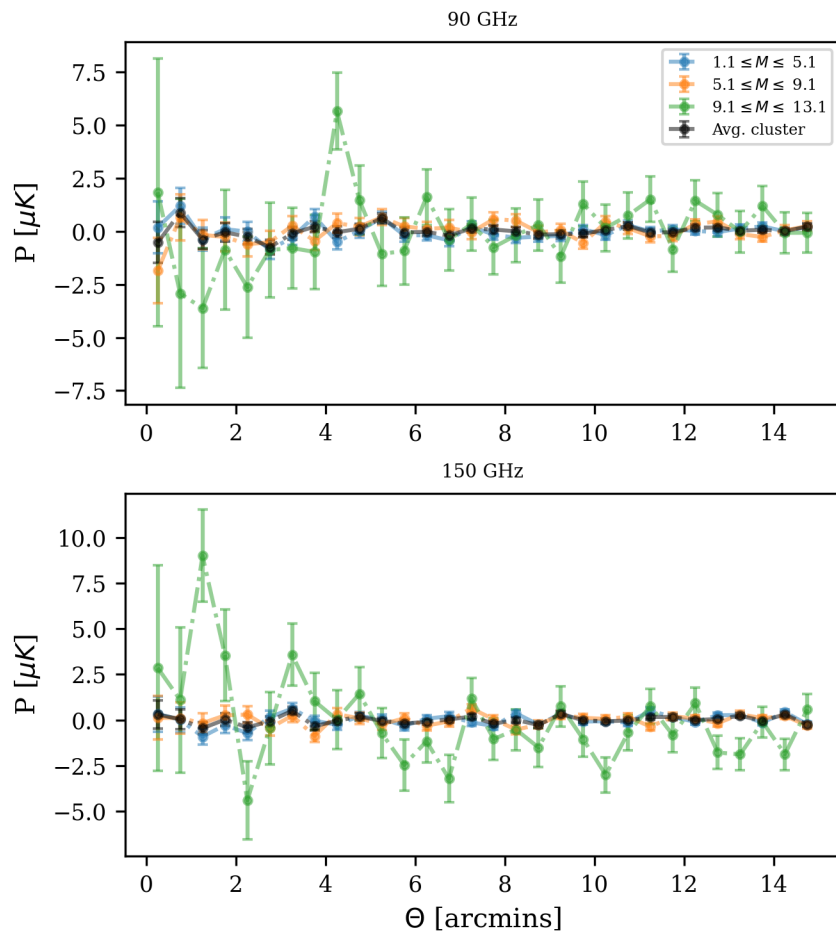
Figure 4.15: The 2 plots in the figure show the radial profiles of the linear polarization P for the averaged Planck clusters stacked by mass at 90 (top) and 150 (bottom) GHz. The legend on the top right identifies each mass, associating to them a color which is kept the same along the top and bottom plot.

Chapter 5

Conclusions

In this work, we have used data from the ACT S18dn cluster catalog and presented many aspects of the ACT characterization and scientific results. The main findings of this thesis are summarized below:

1. In Chapter 3, we computed the abundance redshift distribution of the observed clusters in the ACT catalog. We then illustrated, through a simplified least-squares analysis, that given reasonable assumptions on the observational effects of cluster detection, the calculated distribution generally reconciles with the cosmological prediction of the ΛCDM model for $\sigma_8 \approx 0.8$.

2. In Chapter 4, we used the unfiltered thermal CMB map from ACT and the positions of the clusters from the S18dn catalog, to extract the average radial profiles of clusters, stacked over specific mass and redshift ranges. Given the inverse-variance weighting of each pixel in the map, we were able to resolve the cluster thermal profiles at a very high level of precision with error bars at each radial bin $\sigma_r \lesssim 1\mu\mathrm{K}$, despite the map being unfiltered. This allowed us to test the predictions of the Isothermal β model and the Universal Pressure Profile (UPP). What we found is that at the current state of observation, the UPP

performs generally better and provides physically reasonable estimates for the value of θ_{500c} at each mass and redshift bin.

3. The stacking formalism was then extended to the Q and U polarization maps to obtain the radial profiles of both Stokes parameters and of the total polarization P. Given the high precision achieved by these average cluster profiles, we were able to perform an important test for systematic errors in the map and show that the Q and U profiles, when averaged over enough clusters, do act like pure noise with mean value zero. In regards to the total polarization P, we do not observe a discernible signal coming from the clusters regardless of the average measure used.

4. Finally, we investigated the 525 clusters from the PlanckSZ2 catalog, in the overlapping region with the ACT S18dn field, that were not detected by the ACT experiment. By applying the same stacking formalism used throughout this work, we were able to verify that these clusters can be resolved in the un-filtered ACT S18dn equatorial map. We then investigated the resulting thermal and polarization profiles using the same methodology as for the ACT catalog. In regard to P maps, we found that there is no net polarization signal, in agreement with what was obtained for the ACT S18dn dataset. In regard to the radial profiles, we were able to identify an evident distinction between their average profiles on the two lower mass bins compared to all the other profiles presented in this work. The distinctive properties of these clusters, namely their low mass and large angular scale (very low redshift), perfectly pertain to the class of objects usually filtered out in the ACT experiment, which provides a reasonable explanation for their exclusion from the ACT dataset. Overall, if the preliminary version of the ACT cluster catalog studied in this work is con-firmed, a similar analysis to what we presented here will be necessary in order

to accurately characterize the nature of all the exclusions, and constrain more firmly the completeness level of the survey and any non negligible difference in the mass calibration between the two experiments.

Appendix A

Distance measures in an Expanding Universe

A.1 The Redshift

Light emitted from a distant galaxy which travels towards an observer on Earth is stretched by this expansion according to:

$$\lambda_0 = (1+z)\lambda_e, \tag{A.1}$$

where λ_e is the wavelength at the time of emission and λ_0 is the wavelength we now observe. The parameter z is the so called cosmological redshift of the source which results strictly from the expansion of space and can thus be directly expressed in terms the scale factor $a(t)$, which defines the "size" of the Universe at time t:

$$a(t) = \frac{1}{1+z}. \tag{A.2}$$

It is important to note that there are two other main contributions to the total redshift of an object which are due to its peculiar velocity v_{pec} with respect to the observer and the consequent relativist corrections.

A.2   The Hubble parameter

The Hubble parameter $H(t)$ is named after the American astronomer who in 1929 provided the first evidence for an expanding universe studying the relationship between distance and redshifts of galaxies. $H(t)$ is defined as constant of proportionality between recession speed v and distance d of the universe, it provides a measure of the relative rate of expansion and can hence be expressed in terms of the scale factor a according to:

$$H(t) = \frac{\dot{a}}{a}, \tag{A.3}$$

H_0 represents its present value which in this work I take to be equal to $H_0 = 70$ km s^{-1} Mpc^{-1}, following the same convention as in [7]. A very useful quantity in cosmology is the dimensionless Hubble parameter $E(z)$ defined as the ratio of $H(t)$ to its present value H_0. Combining eq.1.4 with the definition of the redshift in terms of the scale factor, one can derive that:

$$E(z) = \sqrt{\Omega_m^0 (1 + z)^3 + \Omega_\Lambda^0}, \tag{A.4}$$

where in the context of the ΛCDM model, we take $\Omega_\gamma^0 \approx 0$, $\Omega_m^0 = 0.3$ and $\Omega_\Lambda^0 = 0.7$.

A.3   The Angular Diameter Distance

The angular diameter distance D_A is defined as the ratio of an object's physical transverse size to its angular size. It is usually used to convert angular separations in telescope images into proper separations at the source [40].
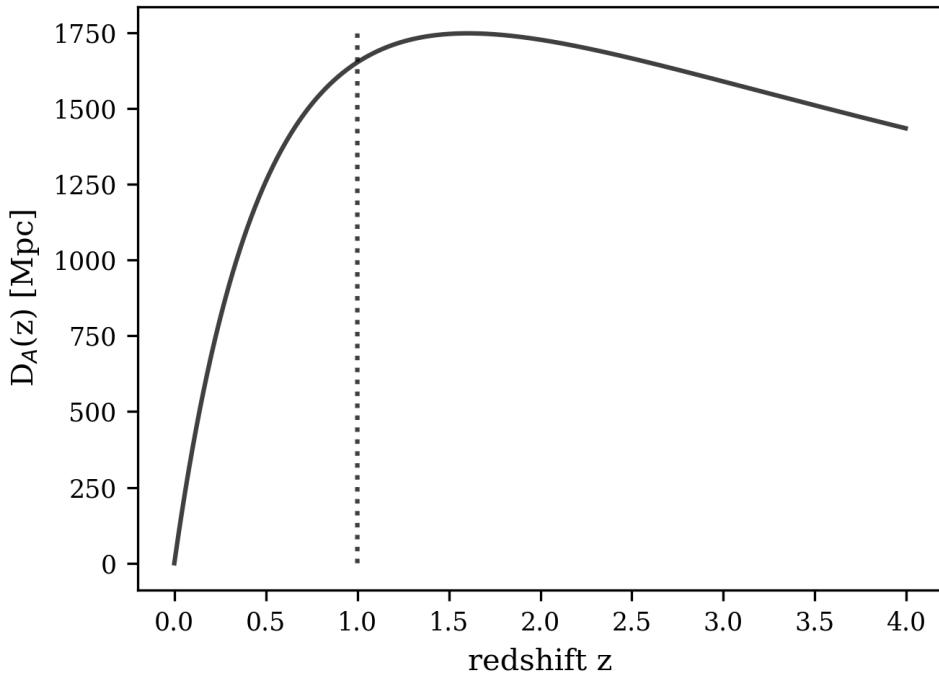
Figure A.1: The figure shows the Angular Diameter Distance D_A as a function of redshift for a ΛCDM cosmology with $\Omega_m^0 = 0.3$ and $\Omega_\Lambda^0 = 0.7$. The dotted line at $z = 1$ indicates the approximate characteristic redshift at which D_A turns and starts decreasing so that more distant objects actually appear larger in angular size.

Its function depends on the assumed geometry and in the case of a spatially flat universe with $k = 0$, D_A is equal to the comoving distance D_C times the scale factor $1/(1 + z)$. D_C is defined in turn as the distance between two objects measured along a path defined at the present cosmological time, in other words is equal to the ratio of the proper distance to the scale factor $a(t)$ [40]. In terms of the redshift, D_A can be expressed as the integral of the inverse of the dimensionless Hubble parameter

$E(z)$:

$$D_A(z) = \frac{c}{H_0} \frac{1}{1+z} \int_0^z \frac{dz'}{E(z')}, \tag{A.5}$$

where $E(z)$ is given by eq.A.4. As shown in the plot above, the $D_A(z)$ function presents a very peculiar feature, which is that it does not increase indefinitely as $z \to \infty$. In fact, the function turns over at $z \sim 1$ such that thereafter more distant objects actually appear larger in angular size [40].

A.4 The Comoving Volume Element

In a similar fashion to the comoving distance D_C, the comoving volume V_C is defined as the proper volume times three factors of the relative scale factor, namely $(1+z)^3$. Its differential per unit solid angle per redshift is given by:

$$\frac{dV}{dzd\Omega} = D_A^2 \frac{c}{H_0} \frac{(1+z)^2}{E(z)}. \tag{A.6}$$

Here, the angular diameter distance together with two factors of $(1+z)$ converts a solid angle Ω into a comoving area [40], which is multiplied by the differential of the comoving distance, proportional to $1/E(z)$ as expressed in eq.A.5. The plot of the comoving volume element, as shown in figure A.2, presents two distinct behaviours for low and high redshifts, increasing approximately exponentially at first and then levelling off after reaching a peak at $z \sim 2$.
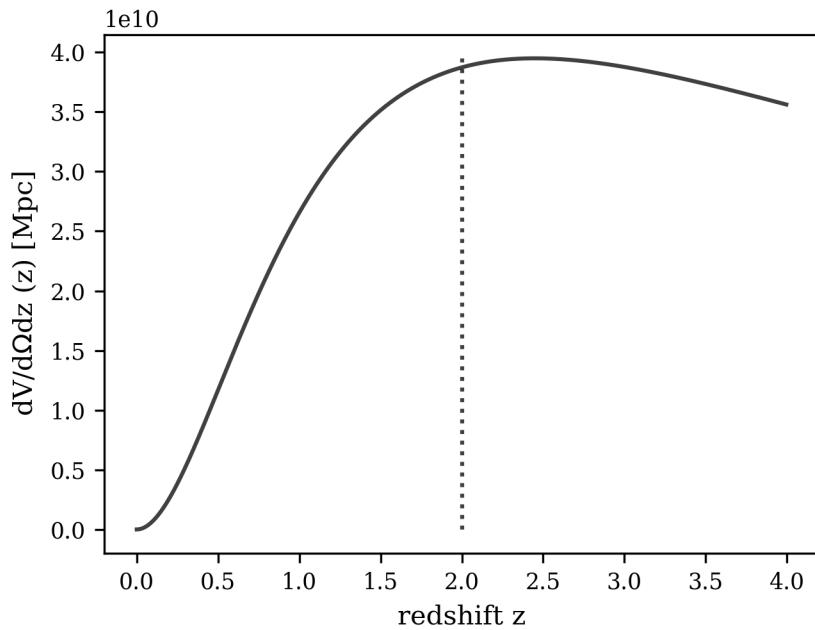
Figure A.2: The figure shows the Comoving Volume element $dV/d\Omega dz$ as a function of redshift for a ΛCDM cosmology with $\Omega_m^0 = 0.3$ and $\Omega_\Lambda^0 = 0.7$. The dotted line at $z = 2$ indicates the approximate characteristic redshift at which $dV/d\Omega dz$ turns and starts flattening similarly to the angular diameter distance D_A. This is explained by the factor of D_A^2 in eq.A.6 which dominates at large z.

Appendix B

Gravitational collapse and Structure growth

Generally, it's known that cosmic expansion plays an important role in the formation of structures on the physical scale of galaxies and above. Specifically, the emerging picture is that gravitational attraction of initially over-dense regions cause the surrounding matter to deviate from the Hubble flow and collapse onto them, forming larger and larger collapsed structures. Considering a small positive spherical density perturbation, the radius of its shell initially expands with the Hubble flow, but then it slows down, turns over and eventually collapses due to the gravitational pull of the excess mass it encloses [25]. The time of maximum size is called the turn-around time t_{ta}, while the time of collapse is referred as the virialization time: $t_{\mathrm{vir}} = t_{\mathrm{coll}} = 2t_{\mathrm{ta}}$.

B.1   The Growth function

The simplest model for cosmological structure growth assumes Birkhoff's theorem which states that spherically symmetric gravitational fields in empty space can be modelled to evolve as independent homogeneous universes with characteristic scale

factor a_p where the subscript p refers to the perturbation [62]. If we take two spheres containing the same mass, one of background density ρ, and the other with density ρ_p, the densities within the spheres are related to their radii by [62]:

$$\rho_p a_p^3 = \rho a^3, \quad \delta \equiv \rho_p/\rho - 1, \tag{B.1}$$

where to first order in in δ, $a_p = a(1 - \delta/3)$. Following the formalism of eq.1.1 and 1.2, the cosmological equation for both the spherical perturbation and the background is then [62]:

$$\frac{1}{a}\frac{d^2 a}{dt^2} = -H_0^2\left[\frac{1}{2}\Omega_m^0 a^{-3} - \Omega_\Lambda^0\right], \tag{B.2}$$

which is valid for both a and a_p and assumes a ΛCDM background model. Using this equation for both spheres and substituting the relations between a, a_p and δ, the result to first order gives:

$$\ddot{\delta} + 2H\dot{\delta} - \frac{3}{2}\Omega_m(a)H^2\delta = 0, \tag{B.3}$$

where $\Omega_m(a) = \Omega_m^0 a^{-3}/E^2(a)$ and the dots denotes a time derivative. This equation can be also derived in the Newtonian limit under the assumption that pressure gradients are negligible [1]. In this limit, one can get eq.B.3, expressed in the same form as eq.1.5 by combining the Continuity, Euler and Poisson equation that govern the behaviour of the over-density δ [10].

An important feature of equation B.3 is that it only includes differential terms in time t which implies that the time evolution is independent of cosmic location x, such that the corresponding solution to eq.B.3 can be separated into a spatial part $\delta(x)$ and a temporal part $D(t)$, such that $\delta(t) = D(t)\delta(x)$.

---

[1]In other words, assuming Ω_m to be the dominant energy element in the universe

$D(t)$ is the linear growth function and it's given by [63]:

$$D(a) = \frac{5\Omega_M^0}{2}E(a)\int_0^a \frac{da'}{\left[a'E\left(a'\right)\right]^3}.$$ (B.4)

In the context of ΛCDM, it is common to use the power series approximation of this integral by Carroll, Press & Turner [64], which states that:

$$D(a) \simeq \frac{5\Omega_m(a)a}{2}\left[\Omega_m(a)^{4/7} - \Omega_\Lambda(a) + \left(1 + \frac{\Omega_M(a)}{2}\right)\left(1 + \frac{\Omega_\Lambda(a)}{70}\right)\right]^{-1}.$$ (B.5)

B.2   Critical density for collapse

At any epoch, there is a critical initial density for collapse δ_c, such that during such epoch of interest all perturbations that are more dense ($\delta \geq \delta_c$) have collapsed, while those that are less dense ($\delta < \delta_c$) have not. δ_c is defined as the value of the linear density contrast extrapolated at the time of collapse ($\delta_c = \delta(t_c)$) and depends on the growth function according to [65]:

$$\delta_c = D_0 \lim_{H_0 t \to 0}\left[\frac{\delta(t)}{D(t)}\right].$$ (B.6)

In the linear approximation, δ_c turns out to be only weakly dependent on the cosmological model, hence, for ease, it is commonly approximated by its value for the Einstein-de Sitter (EdS) cosmological model characterized by $\Omega_m = 1$ and $\Omega_\Lambda = 0$ [62].

In this linear regime, the evolution of the density perturbations is fully encoded in the scale factor $a(t)$ of a EdS universe, calculated according to the Friedman

equations such that:

$$\text{from eqs. 1.1 and 1.2 for EdS: } a(t) = a_0 \left(\frac{8\pi G\rho_0}{3} \right)^{\frac{1}{3}} t^{\frac{2}{3}} \propto t^{\frac{2}{3}}$$

$$\text{linear regime: } \delta(t) \propto D(a) \propto a \propto t^{\frac{2}{3}}$$

$$= \delta_i \left(\frac{t}{t_i} \right)^{\frac{2}{3}}, \tag{B.7}$$

where t_i and δ_i define the initial conditions of the perturbation δ.

Now, in the context of EdS, given a uniform spherical shell of initial radius r_i and density contrast δ_i, its equation of motion is simply determined by [66]:

$$\ddot{r} = -\frac{GM}{r^2} = -\frac{4\pi G}{3r^2} \rho_m^i r_i^3 \left(1 + \delta_i \right), \tag{B.8}$$

where $M = \frac{4\pi}{3} r_i^3 \rho_m^i (1 + \delta_i)$ is the initial total mass of the overdensity [2]. The exact solution of this equation of motion is that of a cycloid parameterized with a variable θ such that [25]:

$$r = A(1 - \cos\theta), \quad t = B(\theta - \sin\theta), \tag{B.9}$$

where A and B are constants to be determined by the initial conditions for the mass shell with values bound by the relation $A^3 = GMB^2$ [3]. The maximum radius r_{ta} occurs at the turn around point for $\theta = \pi$ and hence, according to eq.B.9, is equal to $A/2$. Following the same argument, the time at turn around t_{ta} is also defined at $\theta = \pi$ and is equal to πB [25].

By integrating eq.B.8, we get the energy conservation equation:

$$\frac{1}{2}\dot{r}^2 - \frac{H_i^2 r_i^3}{2r} \left(1 + \delta_i \right) = \text{ constant } \equiv E, \tag{B.10}$$

---

[2]Note the subscripts i on any given quantity x indicate in this notation the initial value of x.

[3]This relation is derived by expanding the solutions of r and t from eq.B.9 at early times for $\theta \ll 1$, keeping the first two non-zero terms of the power series and then plugging them back in eq. B.8 [25].

where I substituted the initial value of the Hubble parameter H_i according to the definition of the critical density in eq.1.3. The value of E can then be expressed in terms of the initial parameters δ_i, r_i and H_i by combining eq.B.10 with the Birkhoff's theorem mentioned earlier, which states that $\frac{\dot{r}_i}{r_i} = \frac{\dot{a}_i}{a_i}(1 - \delta_i/3)$ [66].

$$E = -\frac{5}{3}\frac{(H_i r_i)^2}{2}\delta_i \tag{B.11}$$

Given this value, one can solve eq.B.10 at $\dot{r} = 0$ and obtain the maximum radius at the turn-around point r_{ta}, this time only in terms of δ_i and r_i [66]:

$$r_{\text{ta}} = \frac{3}{5}\left(\frac{1 + \delta_i}{\delta_i}\right)r_i. \tag{B.12}$$

By expanding to linear order in δ_i and combining all the equations that relate A, B, r_{ta} and t_{ta}, it follows that in EdS universe:

$$r_{\text{ta}} = \frac{r_i}{\left[\frac{5}{3}\delta_i + 1\right]}; \quad t_{\text{ta}} = \frac{3\pi}{4}\frac{t_i}{\left[\frac{5}{3}\delta_i + 1\right]^{\frac{3}{2}}} {}^{4} \tag{B.13}$$

Thus, recalling that the collapse time $t_{\text{c}} = 2t_{\text{ta}}$ its corresponding parameter is $\theta_c = 2\pi$. Hence, by plugging the expression of t_{c} from the parametrized solution (eq.B.9) into the definition of $\delta(t)$ from eq.B.7, we can finally derive the famous value of the critical density for linear collapse δ_c:

$$\delta_c = \delta(t_c) = \delta_i\left(\frac{t_c}{t_i}\right)^{\frac{2}{3}} \tag{B.14}$$

$$= \delta_i\left(\frac{3}{4t_i}\frac{t_i}{\left[\frac{5}{3}\delta_i + 1\right]^{\frac{3}{2}}} \cdot 2\pi\right)^{\frac{2}{3}} \tag{B.15}$$

$$= \frac{3}{5}\left(\frac{3\pi}{2}\right)^{\frac{2}{3}} \approx 1.686. \tag{B.16}$$

---

[4] r_{ta} is obtained by eq.B.12 for $\delta_i \lll 1$ which implies $\frac{3}{5}(1 + \delta_i/\delta_i) \approx 1/\left[\frac{5}{3}\delta_i + 1\right]$. t_{ta} is then derived using the relation between A and B and the fact that $r_{\text{ta}} = A/2$, $H_i = \frac{2}{3t_i}$ and $GM = H_i^2 r_i^3(1 + \delta_i)$.

Appendix C

Additional Figures and Tables
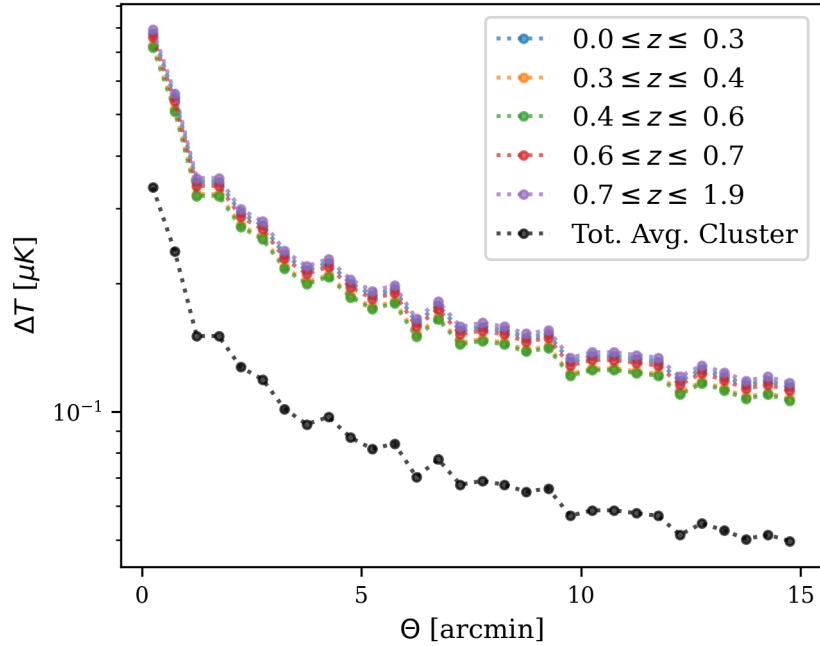
Figure C.1: The figure shows the radial profiles of the errors $\sigma_{\Delta T}$ on the observed thermal decrements for the average clusters stacked by redshift. According to inverse-variance weighting, $\sigma_{\Delta T}(\theta)$ is expected to initially decrease sharply as θ increases and then flatten out at large radii. We observe this behaviour in the picture and also note that the errors for different ranges of z are roughly the same and around 1 order of magnitude greater than those of the total average. This result confirms our expectations since the error profiles shown at each redshift range are computed over an equal amount of clusters N_c according to eq.4.2. On the other hand, the total average by definition is computed over the entire number of clusters $\sim 5N_c$ which should hence lead to lower values for the error at each bin, according to the same formalism.

Mass Stacking	δT_0 [μK]	$\sigma_{\delta T_0}$ [μK]	θ_0 [arcmin]	σ_{θ_0} [arcmin]	β	σ_β	c_0 [μK]	σ_{c_0} [μK]	χ^2_ν
Frequency 90 GHz									
$1.0 \leq M \leq 3.6$	59.9	1.4	1.0	0.1	0.9	0.0	-0.8	0.2	22.7
$3.6 \leq M \leq 6.2$	158.3	3.5	0.7	0.1	0.8	0.0	-3.5	0.5	8.2
$6.2 \leq M \leq 8.8$	327	8.5	0.8	0.1	0.7	0.0	-18.7	2.5	5.4
$8.8 \leq M \leq 11.4$	479.5	7.2	0.9	0.1	0.6	0.0	-37.6	2.9	2.0
$11.4 \leq M \leq 14.1$	640.0	9.5	1.5	0.1	0.8	0.0	-24.2	3.2	1.1
Tot. Avg.	72.2	1.6	0.9	0.1	0.9	0.0	-1.2	0.2	29.2
Frequency 150 GHz									
$1.0 \leq M \leq 3.6$	52.4	1.7	0.9	0.1	1.0	0.1	-0.4	0.1	38.5
$3.6 \leq M \leq 6.2$	137.3	3.3	0.8	0.1	0.9	0.0	-2.0	0.4	12
$6.2 \leq M \leq 8.8$	295.4	11.7	0.7	0.1	0.7	0.0	-18.6	3.2	15
$8.8 \leq M \leq 11.4$	391.6	6.9	0.8	0.1	0.6	0.0	-29.8	2.4	2.0
$11.4 \leq M \leq 14.1$	533.4	11.8	1.53	0.12	0.8	0.0	-20.9	3.6	1.9
Tot. Avg.	62.7	1.8	0.8	0.1	0.9	0.0	-0.7	0.2	47.4

Redshift Stacking	δT_0 [μK]	$\sigma_{\delta T_0}$ [μK]	θ_0 [arcmin]	σ_{θ_0} [arcmin]	β	σ_β	c_0 [μK]	σ_{c_0} [μK]	χ^2_ν
Frequency 90 GHz									
$0.0 \leq z \leq 0.3$	98.5	1.8	1.2	0.1	0.7	-	-6.6	0.7	8.1
$0.3 \leq z \leq 0.4$	68.1	1.5	1.7	0.2	1.2	0.1	-0.5	0.2	11.7
$0.4 \leq z \leq 0.6$	71.5	2.1	0.6	0.1	0.8	-	-1.4	0.2	4.3
$0.6 \leq z \leq 0.7$	61.1	1.5	1.3	0.2	1.4	0.2	-0.1	0.1	5.3
$0.7 \leq z \leq 1.9$	68.0	4.3	0.7	0.2	1.1	0.1	-0.4	0.1	13.1
Tot. Avg.	72.2	1.6	0.9	0.1	0.9	-	-1.2	0.2	29.2
Frequency 150 GHz									
$0.0 \leq z \leq 0.3$	83.3	1.9	1.0	0.1	0.7	-	-6.0	0.7	12
$0.3 \leq z \leq 0.4$	58.2	1.9	1.5	0.2	1.3	0.1	-0.3	0.2	21.2
$0.4 \leq z \leq 0.6$	58.9	1.7	0.8	0.1	1.0	-	-0.4	0.1	6.4
$0.6 \leq z \leq 0.7$	55.3	3.0	1.5	0.5	2.0	0.7	-0.4	0.1	25.6
$0.7 \leq z \leq 1.9$	63.0	4.5	0.7	0.2	1.2	0.2	-0.4	0.1	22.0
Tot. Avg.	62.7	1.8	0.8	0.1	0.9	-	-0.7	0.2	47.4

Table C.1: The two tables contain a report of the best fits of the Isothermal β model as expressed in eq.4.5, to the average clusters profiles stacked by mass (top) and redshift (bottom) at both 90 and 150 GHz. For each fit, the tables include the estimated values for the free parameters ($\delta T_{0,\beta}$, θ_c, β, $c_{0,\beta}$), their respective statistical errors ($\sigma_{\delta T_{0,\beta}}$, σ_{θ_c}, σ_β, $\sigma_{c_{0,\beta}}$) and the resulting χ^2_ν. All quantities are reported with precision to 1 decimal place. The dashes – follow the same convention established in table 4.1. The highly variance on the values of β and the angular core radius θ_c, combined with their extremely low statistical errors, is physically unacceptable and it's thus evidence of the impracticality of performing fits with the β-model without first fixing β to a reasonable value.

Stacking Group	χ^2_ν for U	χ^2_ν for Q
Frequency 90 GHz		
$0.0 \leq z \leq 0.3$	1.4	1.0
$0.3 \leq z \leq 0.4$	2.3	2.2
$0.4 \leq z \leq 0.6$	2.1	1.9
$0.6 \leq z \leq 0.7$	1.1	1.7
$0.7 \leq z \leq 1.9$	1.8	1.0
Tot. Avg.	1.6	1.3
Frequency 150 GHz		
$0.0 \leq z \leq 0.3$	2.8	2.0
$0.3 \leq z \leq 0.4$	4.2	1.2
$0.4 \leq z \leq 0.6$	3.1	3.3
$0.6 \leq z \leq 0.7$	1.8	1.9
$0.7 \leq z \leq 1.9$	2.0	1.6
Tot. Avg.	1.7	1.2

Table C.2: The table contains a report of the χ^2_ν obtained by fitting a flat line of the form $f(\theta) = 0$ to the radial profiles of the Stokes parameters Q and U for the clusters groups stacked by redshift at both 90 and 150 GHz. Overall, $\chi^2_\nu \sim 1$ for most of the stacking groups considered, with exceptions that all present values of $\chi^2_\nu \lesssim 4$, which are not to be considered as a statistically significant variation. All quantities are reported with precision to 1 decimal place.

Bibliography

[1] P. Collaboration, "Plancksz2 - planck 2nd sunyaev-zeldovich source catalog." [Online]. Available: https://heasarc.gsfc.nasa.gov/W3Browse/planck/plancksz2. html

[2] "Cmb temperature map from the wmap satellite mission." [Online]. Available: https://map.gsfc.nasa.gov/media/121238/index.html

[3] J. E. Carlstrom, G. P. Holder, and E. D. Reese, "Cosmology with the Sunyaev-Zel'dovich effect," *Ann. Rev. Astron. Astrophys.*, vol. 40, pp. 643–680, 2002.

[4] M. Arnaud, G. W. Pratt, R. Piffaretti, H. Böhringer, J. H. Croston, and E. Pointe-couteau, "The universal galaxy cluster pressure profile from a representative sample of nearby systems (REXCESS) and the Y_{SZ} - M_{500} relation," , vol. 517, p. A92, Jul 2010.

[5] J. L. Tinker, A. V. Kravtsov, A. Klypin, K. Abazajian, M. S. Warren, G. Yepes, S. Gottlober, and D. E. Holz, "Toward a halo mass function for precision cosmology: The Limits of universality," *Astrophys. J.*, vol. 688, pp. 709–728, 2008.

[6] M. Hasselfield *et al.*, "The Atacama Cosmology Telescope: Sunyaev-Zel'dovich selected galaxyclusters at 148 GHz from three seasons of data," *JCAP*, vol. 1307, p. 008, 2013.

[7] M. Hilton *et al.*, "The Atacama Cosmology Telescope: The Two-Season ACTPol Sunyaev-Zel'dovich Effect Selected Cluster Catalog," *Astrophys. J. Suppl.*, vol. 235, no. 1, p. 20, 2018.

[8] B. Ryden, *Introduction to Cosmology*. Cambridge University Press, 2017. [Online]. Available: https://books.google.com/books?id=07WSDQAAQBAJ

[9] M. Hasselfield, "Galaxy cluster cosmology with the atacama cosmology telescope," *Ph.D. thesis, University of British Columbia (2013)*. [Online]. Available: https://open.library.ubc.ca/cIRcle/collections/ubctheses/24/items/1.0085698

[10] P. Peebles, *Principles of Physical Cosmology*, ser. Princeton Series in Physics. Princeton University Press, 1993. [Online]. Available: https://books.google.com/books?id=AmlEt6TJ6jAC

[11] F. R. Aracena, "Making maps with act data," *Ph.D. thesis, Pontificia Universidad Catolica de Chile (2014)*. [Online]. Available: https://act.princeton.edu/sites/act/files/thesis_msc_feliperojas.pdf

[12] J. R. Peterson and A. C. Fabian, "X-ray spectroscopy of cooling clusters," *Phys. Rept.*, vol. 427, pp. 1–39, 2006.

[13] G. Bertone and D. Hooper, "History of dark matter," *Reviews of Modern Physics*, vol. 90, no. 4, Oct. 2018. [Online]. Available: https://doi.org/10.1103/revmodphys.90.045002

[14] R. D. Planella, "From data to maps with the atacama cosmology telescope," *Ph.D. thesis, Pontificia Universidad Catolica de Chile (2009)*. [Online]. Available: https://act.princeton.edu/sites/act/files/rolando-dunner.pdf

[15] S. Staggs, J. Dunkley, and L. Page, "Recent discoveries from the cosmic microwave background: a review of recent progress," *Reports on Progress in Physics*, vol. 81, no. 4, p. 044901, feb 2018. [Online]. Available: https://doi.org/10.1088%2F1361-6633%2Faa94d5

[16] M. Lungu, "Exploring the universe with the atacama cosmology telescope: Polarization-sensitive measurements of the cosmic microwave background," *Publicly Accessible Penn Dissertations. 2990.*, 2017.

[17] J. M. Kovac, E. M. Leitch, C. Pryke, J. E. Carlstrom, N. W. Halverson, and W. L. Holzapfel, "Detection of polarization in the cosmic microwave background using dasi," *Nature*, vol. 420, no. 6917, p. 772–787, Dec 2002. [Online]. Available: http://dx.doi.org/10.1038/nature01269

[18] M. Zaldarriaga and U. Seljak, "An all sky analysis of polarization in the microwave background," *Phys. Rev. D*, vol. 55, pp. 1830–1840, 1997.

[19] M. Kamionkowski, A. Kosowsky, and A. Stebbins, "Statistics of cosmic microwave background polarization," *Physical Review D*, vol. 55, no. 12, p. 7368–7388, Jun 1997. [Online]. Available: http://dx.doi.org/10.1103/PhysRevD.55.7368

[20] A. F. et Al., "The 13th data release of the sloan digital sky survey: First spectroscopic data from the sdss-iv survey mapping nearby galaxies at apache point observatory," , vol. 233, no. 2, p. 25, Dec 2017.

[21] J. Annis, M. Soares-Santos, M. A. Strauss, A. C. Becker, S. Dodelson, X. Fan, J. E. Gunn, J. Hao, Ž. Ivezić, S. Jester, L. Jiang, D. E. Johnston, J. M. Kubo, H. Lampeitl, H. Lin, R. H. Lupton, G. Miknaitis, H.-J. Seo, M. Simet, and B. Yanny, "The Sloan Digital Sky Survey Coadd: 275 deg^2 of Deep Sloan Digital Sky Survey Imaging on Stripe 82," , vol. 794, no. 2, p. 120, Oct 2014.

[22] M. Scodeggio, L. Guzzo, B. Garilli, B. R. Granett, M. Bolzonella, S. de la Torre, U. Abbas, C. Adami, S. Arnouts, D. Bottini, and et al., "The vimos public

extragalactic redshift survey (vipers)," *Astronomy Astrophysics*, vol. 609, p. A84, Jan 2018. [Online]. Available: http://dx.doi.org/10.1051/0004-6361/201630114

[23] T. Erben, H. Hildebrandt, L. Miller, L. van Waerbeke, C. Heymans, H. Hoekstra, T. D. Kitching, Y. Mellier, J. Benjamin, C. Blake, C. Bonnett, O. Cordes, J. Coupon, L. Fu, R. Gavazzi, B. Gillis, E. Grocutt, S. D. J. Gwyn, K. Holhjem, M. J. Hudson, M. Kilbinger, K. Kuijken, M. Milkeraitis, B. T. P. Rowe, T. Schrabback, E. Semboloni, P. Simon, M. Smit, O. Toader, S. Vafaei, E. van Uitert, and M. Velander, "CFHTLenS: the Canada–France–Hawaii Telescope Lensing Survey – imaging data and catalogue products," *Monthly Notices of the Royal Astronomical Society*, vol. 433, no. 3, pp. 2545–2563, 06 2013. [Online]. Available: https://doi.org/10.1093/mnras/stt928

[24] H. Hildebrandt, T. Erben, K. Kuijken, L. van Waerbeke, C. Heymans, J. Coupon, J. Benjamin, C. Bonnett, L. Fu, H. Hoekstra, T. D. Kitching, Y. Mellier, L. Miller, M. Velander, M. J. Hudson, B. T. P. Rowe, T. Schrabback, E. Semboloni, and N. Benítez, "CFHTLenS: improving the quality of photometric redshifts with precision photometry*," *Monthly Notices of the Royal Astronomical Society*, vol. 421, no. 3, pp. 2355–2367, 04 2012. [Online]. Available: https://doi.org/10.1111/j.1365-2966.2012.20468.x

[25] H. Mo, F. van den Bosch, and S. White, *Galaxy Formation and Evolution*, ser. Galaxy Formation and Evolution.   Cambridge University Press, 2010. [Online]. Available: https://books.google.com/books?id=Zj7fDU3Z4wsC

[26] A. Cavaliere and R. Fusco-Femiano, "Reprint of 1976A&A....49..137C. X-rays from hot plasma in clusters of galaxies." , vol. 500, pp. 95–102, May 1976.

[27] J. Pollack, "Parameter estimation of selected act clusters from x-ray and radio observations," *Junior Independent work, Princeton University (2011).* [Online]. Available: https://www.phas.ubc.ca/~jpollack/spring_jp.pdf

[28] I. R. King, "Density Data and Emission Measure for a Model of the Coma Cluster," , vol. 174, p. L123, Jun. 1972.

[29] S. R. for Galaxy Clusters, "From data to maps with the atacama cosmology telescope," *Junior Independent Work, Princeton University (2019).*

[30] J. F. Navarro, C. S. Frenk, and S. D. White, "The Structure of cold dark matter halos," *Astrophys. J.*, vol. 462, pp. 563–575, 1996.

[31] D. Nagai, A. Vikhlinin, and A. V. Kravtsov, "Testing X-Ray Measurements of Galaxy Clusters with Cosmological Simulations," , vol. 655, no. 1, pp. 98–108, Jan. 2007.

[32] G. M. Voit, S. T. Kay, and G. L. Bryan, "The baseline intracluster entropy profile from gravitational structure formation," *Monthly Notices of the Royal Astronomical Society*, vol. 364, no. 3, p. 909–916, Dec 2005. [Online]. Available: http://dx.doi.org/10.1111/j.1365-2966.2005.09621.x

[33] Z. Haiman, J. J. Mohr, and G. P. Holder, "Constraints on quintessence from future galaxy cluster surveys," *Astrophys. J.*, vol. 553, p. 545, 2000.

[34] N. A. Bahcall and X. Fan, "The most massive distant clusters: Determining $\{upOmega$ and 8," *The Astrophysical Journal*, vol. 504, no. 1, pp. 1–6, sep 1998. [Online]. Available: https://doi.org/10.1086%2F306088

[35] L. Wang and P. J. Steinhardt, "Cluster abundance constraints for cosmological models with a time-varying, spatially inhomogeneous energy component with negative pressure," *The Astrophysical Journal*, vol. 508, no. 2, pp. 483–490, dec 1998. [Online]. Available: https://doi.org/10.1086%2F306436

[36] P. T. Viana, R. C. Nichol, and A. R. Liddle, "Constraining the matter power spectrum normalization using the SDSS/RASS and reflex cluster surveys," *Astrophys. J.*, vol. 569, p. L75, 2002.

[37] Z. Staniszewski *et al.*, "Galaxy clusters discovered with a Sunyaev-Zel'dovich effect survey," *Astrophys. J.*, vol. 701, pp. 32–41, 2009.

[38] P. Ade *et al.*, "Planck 2015 results. XXIV. Cosmology from Sunyaev-Zeldovich cluster counts," *Astron. Astrophys.*, vol. 594, p. A24, 2016.

[39] S. W. Allen, A. E. Evrard, and A. B. Mantz, "Cosmological parameters from observations of galaxy clusters," *Annual Review of Astronomy and Astrophysics*, vol. 49, no. 1, p. 409–470, Sep 2011. [Online]. Available: http://dx.doi.org/10.1146/annurev-astro-081710-102514

[40] D. W. Hogg, "Distance measures in cosmology," 1999.

[41] W. H. Press and P. Schechter, "Formation of Galaxies and Clusters of Galaxies by Self-Similar Gravitational Condensation," , vol. 187, pp. 425–438, Feb. 1974.

[42] A. Jenkins, C. Frenk, S. D. White, J. Colberg, S. Cole, A. E. Evrard, H. Couchman, and N. Yoshida, "The Mass function of dark matter halos," *Mon. Not. Roy. Astron. Soc.*, vol. 321, p. 372, 2001.

[43] J. R. Bond, S. Cole, G. Efstathiou, and N. Kaiser, "Excursion set mass functions for hierarchical gaussian fluctuations," *The Astrophysical Journal*, vol. 379, p. 440, Oct. 1991. [Online]. Available: https://doi.org/10.1086/170520

[44] J. Lee and S. F. Shandarin, "The cosmological mass distribution function in the zeldovich approximation," *The Astrophysical Journal*, vol. 500, no. 1, pp. 14–27, jun 1998. [Online]. Available: https://doi.org/10.1086%2F305710

[45] R. K. Sheth and G. Tormen, "Large-scale bias and the peak background split," *Monthly Notices of the Royal Astronomical Society*, vol. 308, no. 1, pp. 119–126, Sep. 1999. [Online]. Available: https://doi.org/10.1046/j.1365-8711.1999.02692.x

[46] A. E. Evrard, T. J. MacFarland, H. M. P. Couchman, J. M. Colberg, N. Yoshida, S. D. M. White, A. Jenkins, C. S. Frenk, F. R. Pearce, J. A. Peacock, and P. A. T. T. V. Consortium), "Galaxy clusters in hubble volume simulations: Cosmological constraints from sky survey populations," *The Astrophysical Journal*, vol. 573, no. 1, pp. 7–36, Jul. 2002. [Online]. Available: https://doi.org/10.1086/340551

[47] D. S. Reed, R. Bower, C. S. Frenk, A. Jenkins, and T. Theuns, "The halo mass function from the dark ages through the present day," *Monthly Notices of the Royal Astronomical Society*, vol. 374, no. 1, pp. 2–15, Jan. 2007. [Online]. Available: https://doi.org/10.1111/j.1365-2966.2006.11204.x

[48] P. Collaboration, "Planck 2018 results. vi. cosmological parameters," 2018.

[49] T. de Haan *et al.*, "Cosmological Constraints from Galaxy Clusters in the 2500 square-degree SPT-SZ Survey," *Astrophys. J.*, vol. 832, no. 1, p. 95, 2016.

[50] M. Arnaud, E. Pointecouteau, and G. Pratt, "The Structural and scaling properties of nearby galaxy clusters. 2. The M-T relation," *Astron. Astrophys.*, vol. 441, pp. 893–903, 2005.

[51] M. Aguena and M. Lima, "Effects of completeness and purity on cluster dark energy constraints," *Physical Review D*, vol. 98, no. 12, Dec 2018. [Online]. Available: http://dx.doi.org/10.1103/PhysRevD.98.123529

[52] C. Jones and W. Forman, "The structure of clusters of galaxies observed with Einstein." , vol. 276, pp. 38–55, Jan. 1984.

[53] R. F. Mushotzky, "X-ray emission from clusters of galaxies." *Physica Scripta Volume T*, vol. 7, pp. 157–162, Jan. 1984.

[54] E. J. Hallman, J. O. Burns, P. M. Motl, and M. L. Norman, "The -model problem: The incompatibility of x-ray and sunyaev-zeldovich effect model fitting for galaxy clusters," *The Astrophysical Journal*, vol. 665, no. 2, p. 911–920, Aug 2007. [Online]. Available: http://dx.doi.org/10.1086/519447

[55] M. Arnaud, "The -model of the intracluster medium," *Astronomy & Astrophysics*, vol. 500, no. 1, pp. 103–104, Jun. 2009. [Online]. Available: https://doi.org/10.1051/0004-6361/200912150

[56] M. S. Emritte, S. Colafrancesco, and P. Marchegiani, "Polarization of the sunyaev-zel'dovich effect: relativistic imprint of thermal and non-thermal plasma," *Journal of Cosmology and Astroparticle Physics*, vol. 2016, no. 07, p. 031–031, Jul 2016. [Online]. Available: http://dx.doi.org/10.1088/1475-7516/2016/07/031

[57] R. Maartens, "Is the universe homogeneous?" *Philosophical Transactions of the Royal Society A: Mathematical, Physical and Engineering Sciences*, vol. 369, no. 1957, p. 5115–5137, Dec 2011. [Online]. Available: http://dx.doi.org/10.1098/rsta.2011.0289

[58] A. Cooray and D. Baumann, "Cmb polarization towards clusters as a probe of the integrated sachs-wolfe effect," *Phys. Rev. D*, vol. 67, p. 063505, Mar 2003. [Online]. Available: https://link.aps.org/doi/10.1103/PhysRevD.67.063505

[59] S. Y. Sazonov and R. A. Sunyaev, "Microwave polarization in the direction of galaxy clusters induced by the cmb quadrupole anisotropy," *Monthly Notices of the Royal Astronomical Society*, vol. 310, no. 3, p. 765–772, Dec 1999. [Online]. Available: http://dx.doi.org/10.1046/j.1365-8711.1999.02981.x

[60] N. Aghanim, M. Douspis, G. Hurier, D. Crichton, J.-M. Diego, M. Hasselfield, J. Macias-Perez, T. A. Marriage, E. Pointecouteau, M. Remazeilles, and E. Soubrié, "PACT," *Astronomy & Astrophysics*, vol. 632, p. A47, Nov. 2019. [Online]. Available: https://doi.org/10.1051/0004-6361/201935271

[61] P. A. R. Ade, N. Aghanim, M. Arnaud, M. Ashdown, F. Atrio-Barandela, J. Aumont, C. Baccigalupi, A. Balbi, A. J. Banday, and et al., "Planckintermediate results," *Astronomy Astrophysics*, vol. 550, p. A131, Feb 2013. [Online]. Available: http://dx.doi.org/10.1051/0004-6361/201220040

[62] W. J. Percival, "Large scale structure observations," 2013.

[63] D. J. Heath, "The growth of density perturbations in zero pressure Friedmann-Lemaître universes." , vol. 179, pp. 351–358, May 1977.

[64] S. M. Carroll, W. H. Press, and E. L. Turner, "The cosmological constant." , vol. 30, pp. 499–542, Jan. 1992.

[65] W. J. Percival, "Cosmological structure formation in a homogeneous dark energy background," *Astronomy Astrophysics*, vol. 443, no. 3, p. 819–830, Nov 2005. [Online]. Available: http://dx.doi.org/10.1051/0004-6361:20053637

[66] V. Desjacques, D. Jeong, and F. Schmidt, "Large-scale galaxy bias," *Physics Reports*, vol. 733, p. 1–193, Feb 2018. [Online]. Available: http://dx.doi.org/10.1016/j.physrep.2017.12.002